Report No. NASA CR-66037

AN INVESTIGATION OF THE AERODYNAMIC CHARACTERISTICS OF A 25° SPHERE-CONE INCLUDING A PRESSURE DISTRIBUTION ANALYSIS AT ANGLES OF ATTACK, AND A TRAJECTORY ANALYSIS DURING A TYPICAL REENTRY TRAJECTORY

By JOHN W. ARNOLD, HARMON L. SIMMONS, and WILLIAM T. MILLER

Prepared under Contract No. NAS1-3915 by
LTV AEROSPACE CORPORATION, Astronautics Division
Dallas, Texas

for

NATIONAL AERONAUTICS AND SPACE ADMINISTRATION
LANGLEY RESEARCH CENTER
Hampton, Virginia

OUTLINE OF CONTENTS

SUMMARY

15

Aerodynamic data on a low fineness ratio 25° half angle sphere-cone reentry body are presented as functions of Mach number, Reynolds number and angle of attack, and are used as inputs in a trajectory analysis study. The aerodynamic data presented include force and moment derivatives, base pressure and skin friction data, and an estimate of the dynamic stability for Mach numbers up to (M) 26. Also included is a detailed pressure distribution analysis for Mach numbers (M) $\geq$ 4 and angles of attack up to 15 degrees. These data were obtained from a compilation, correlation, and interpolation of many data reports from several sources.

As an aid in the selection of the minimum entry path angle commensurate with impact range requirements, nominal Scout launch vehicle performance in the form of burnout range versus burnout flight path angle is presented along with impact dispersion as a function of entry angle. A typical nominal trajectory and an accuracy analysis showing the burnout and impact deviations attributable to individual error sources are also presented.

A digital computer reentry trajectory study was conducted to establish the most favorable center of gravity location and to determine the individual effects of tip-off, mass unbalance and center of gravity offset. The effect of c.g. location and of each of the individual disturbances on the angle of attack envelope is shown. Center of gravity offset was found to have a particularly adverse effect on the angle of attack history.

The pitch frequency for the spinning body was determined for the nominal trajectory and several off-nominal cases. Although roll-pitch resonance was not experienced for any of the cases considered (there was no roll lock-in or catastrophic yaw) conditions are identified which could result in severe angular motions due to lock-in.

INTRODUCTION

Among the configuations most acceptable for re-entry vehicles are spherically tipped conical frustrums. These are basic aerodynamic shapes and as such have been the object of extensive aerodynamic research for a number of years. A considerable amount of data have accumulated for a large range of parameters, but a survey shows that many information voids still exist.

An extensive literature survey was conducted to gather all available information pertaining to the aerodynamic properties of sphere-cones in an attempt to present in this report accurate aerodynamic characteristics of a 25° half angle spherically blunted cone. The data presented were obtained from a correlation and interpolation of data from many sources, including theoretical results.

As an aid in the selection of nominal burnout conditions, an estimate of impact range dispersion as a function of nominal entry flight path angle was made using previously established "Scout" burnout errors. On the basis of this estimate, a nominal entry angle that was compatible with the impact dispersion requirements was selected and a nominal boost trajectory was established. An accuracy analysis of this booster trajectory was performed to re-establish burnout deviations. On the basis of these burnout deviations an improved estimate of the impact dispersion was established.

Using the aerodynamic data established herein, a six-degree of freedom digital computer study was conducted to investigate the effect of variations in center of gravity location on the dynamic behavior of the spacecraft during descent through the atmosphere. On the basis of this study a nominal center of gravity was selected and additional trajectories were computed to determine the individual effects of tip-off, mass unbalance and center of gravity offset.

For convenience in presentation, this report is divided into four basic divisions; Aerodynamic Stability Analysis, Aerodynamic Pressure Analysis, Impact Dispersion Study, and Reentry Dynamics Study. The Aerodynamic Stability Analysis section presents the data pertaining to overall aerodynamic performance, including normal force coefficient, center of pressure location, pitching moment coefficient, axial force coefficient, and damping-in-pitch derivatives. The Aerodynamic Pressure Analysis section presents a theoretical method of obtaining the pressure distribution over a sphere-cone at angles of attack. The Impact Dispersion Study section presents the results of a trajectory study of impact errors resulting from deviations in nominal booster performance during a typical re-entry trajectory. The Reentry Dynamics study section analyzes effects of mass unbalance and center of gravity travel on the vehicle motions during reentry.

This study was sponsored by the National Aeronautics and Space Administration, Langley Research Center, and performed by the Ling-Temco-Vought Astronautics Division under Contract NAS1-3915, Work Item 8.

The work was performed for the Vehicles Performance Branch of the Applied Materials and Physics Division and under the technical cognizance of James L. Raper and Robert L. Wright.

LIST OF SYMBOLS

C_A - Integrated forebody pressure drag coefficient measured along axis of symmetry, not including base drag or skin friction drag,

$$\text{Forebody Pressure Drag}/.5\ \gamma\ P_\infty M^2 S$$

$C_{A_{\alpha=o}}$ - Integrated forebody pressure drag coefficient at zero angle of attack, $C_{A_o} - C_{A_b} - C_{A_f}$, or

$$C_{A_{\alpha=o}} = \frac{\pi R^2}{S}\int_o^1 Cp(\eta)\,d\eta$$

C_{A_b} - Base pressure drag coefficient, equal to $\left[-C_{p_b} S_b/S\right]$

C_{A_f} - Integrated skin friction drag coefficient measured along axis of symmetry,

$$\text{Skin Friction Drag}/.5\ \gamma\ P_\infty M^2 S$$

C_{A_o} - Total drag coefficient measured along axis of symmetry, $C_A + C_{A_b} + C_{A_f}$

C_M - Pitching moment coefficient measured about the moment reference, Pitch Moment / $.5\ \gamma P_\infty M^2 SD$

C_{M_α} - Pitching moment coefficient variation with angle of attack at $\alpha = o$, i.e.

$$C_{M_\alpha} = \left.\frac{\partial C_M}{\partial \alpha}\right|_{\alpha=o}, \text{ per degree}$$

C_{M_q} - Pitching moment coefficient variation with pitch velocity rate, i.e.

$$C_{M_q} = \frac{\partial C_M}{\partial\left(\frac{qD}{2V}\right)}, \text{ per degree or per radian}$$

C_N - Normal force coefficient measured normal to the axis of symmetry, Normal Force / $.5\ \gamma P_\infty M^2 S$

C_{N_α} - Variation of normal force coefficient with angle of attack at $\alpha = o$, i.e.

$$C_{N_\alpha} = \left.\frac{\partial C_N}{\partial \alpha}\right|_{\alpha = o} .$$

C_p - Pressure coefficient, $\frac{2}{\gamma M^2}\left[\frac{P}{P_\infty} - 1\right]$.

C_p^* - Stagnation pressure coefficient behind normal shock, given by

$$\frac{\gamma+3}{\gamma+1}\left[1 - \frac{2}{(\gamma+3)M^2}\right] .$$

C_{p_b} - Base pressure coefficient, $(\bar{P}_b - P_\infty)/q_\infty$.

$C_p(\eta)$ - Surface pressure coefficient presented as a function of η.

C_{p_ϕ} - Circumferential pressure coefficient at a meridian angle on a sharp cone at angle of attack.

$C_{p_{\phi = o}}$ - Pressure coefficient on windward meridian, $\phi = o$, at angle of attack on sharp cones.

$C_{p_{\alpha = o}}$ - Sharp cone pressure coefficient at zero angle of attack given by tables of Kopal or Sims (Reference 4).

$C_{p_{TC}}$ - Pressure coefficient at s/R and ψ obtained using the "Tangent Sphere-Cone" method without the cross flow modification.

ΔC_p - Difference between $C_{p_{TC}}$ at $(s/R)_T$ and C_{p_ϕ}, i.e.

$$\Delta C_p = (C_{p_{TC}} - C_{p_\phi}) \text{ at } (s/R)_T$$

D - Reference length, maximum diameter of sphere-cone body, 2.5 ft.

h - Altitude from sea level, ft.

I - Pitch moment of inertia = 4.2 slug ft^2

I_x - Roll moment of inertia = 3.2 slug ft^2

K - Circumferential pressure distribution constant defined by equation 8, page 31.

ℓ	- Slant length of body, ft.
M	- Free stream Mach number
M_2	- Mach number behind normal shock
P_∞	- Free stream static pressure, lb/ft^2
P_{stag}	- Pressure at stagnation point behind normal shock, lb/ft^2
$p(s/R,\phi)$	- Point, located on sphere-cone by coordinates s/R and ϕ
P	-Surface pressure on sphere-cone at point $p(s/R,\phi)$, lb/ft^2, or spin frequency
$\bar{P}_b$	- Averaged base pressure over base area, lb/ft^2
q_∞	- Free stream dynamic pressure, $1/2\,\gamma P_\infty M^2$, lb/ft^2.
q	- Rate of change of pitch attitude with time, deg/sec.
r	- Axisymmetric radial body coordinate
R_N	- Reynolds number, $\frac{\rho V \ell}{\mu}$
R	- Radius of spherical nose on sphere-cone bodies, ft.
S	- Reference area, $\frac{\pi D^2}{4}$, ft^2
s	- Distance along a meridian line (points of constant ϕ) measured from the intersection of the axis of symmetry to the point $p(s/R, \phi)$, ft.
s_1	- Distance along a meridian path measured from the stagnation point on a hemisphere to the point $p(s/R,\phi)$ also on the hemisphere, ft.
S_b	- Area of base over which $\bar{P}_b$ acts, ft^2.
$(s/R)_T$	- Normalized distance to the tangency point where pressures in the conical overexpansion region reach the sharp cone value corresponding to a cone angle ψ.
V	- Free stream velocity, ft/sec.
x	- Distance measured parallel to axis of symmetry from nose to the point $p(s/R, \phi)$, ft.
X_{CG}	- Distance measured along axis of symmetry from model base to the moment reference center (center of gravity).

X_{CP} - Distance measured along axis of symmetry from model base to the intersection of the integrated force vector and the axis of symmetry, ft., positive upstream.

Z_{CP} - Distance measured from the axis of symmetry to the intersection point of the integrated force vector and a line normal to the axis of symmetry passing through the moment reference, ft. (See Fig. 1).

Z_{CG} - Distance from axis of symmetry to the center of gravity measured along the Z-axis.

α - Angle of attack, deg.

$\alpha_{P_{max}}$ - The angle of attack for maximum pressure on the windward meridian of sharp cone, Reference 62.

β - Included angle on hemisphere defined by s/R.

γ - Ratio of specific heats considered constant (i.e. perfect gas), $\gamma = 1.4$ for air; or, flight path angle, deg.

ξ - Angle defined by equation 6, page 31.

η - Pressure integration ordinate, $(r/R)^2$.

θ - Cone semi-vertex angle, degrees or radians.

ϕ - Angle between the vertical windward meridian plane and the meridian plane passing through the point $p(s/R, \phi)$.

ρ - Free stream air density, lb sec^2/ft^4.

μ - Absolute viscosity of free stream air, lb sec/ft^2.

ψ - Included angle between the stagnation velocity vector and the conical ray lying along the meridian line defined by points of constant ϕ.

σ - Ratio of roll inertia to pitch inertia, $I_x/I = 0.762$.

ω - Non-spinning body pitch frequency divided by the spin frequency,

$$\frac{1}{P}\sqrt{\frac{-C_{M_\alpha} q_\infty SD}{I}}$$

Ω_1 - Spinning body high pitch frequency

Ω_2 - Spinning body low pitch frequency

$\rho_{\Delta V \Delta h}$ - Correlation coefficient between velocity and altitude errors.

$\rho_{\Delta V \Delta \gamma}$ - Correlation coefficient between velocity and path angle errors.

$\rho_{\Delta h \Delta \gamma}$ - Correlation coefficient between altitude and path angle errors.

DISCUSSION OF RESULTS

A. Aerodynamic Stability Analysis

1. Summary

Aerodynamic stability data for a 25 degree sphere-cone are presented in this division. Longitudinal force and moment coefficients and dynamic stability derivatives are estimated for Mach numbers up to M = 26 and for angles of attack up to 15 degrees. Reynolds number effects are also indicated.

In the appropriate sections below a discussion is made concerning the extent of the literature search, the range of parameters covered, a brief synopsis of several theoretical methods considered for application to this problem, and a discussion of the data presented.

2. Configuration

A sketch of the basic configuration under study is shown in Figure 1. The configuration consists of a spherically blunted 25 degree half angle cone of bluntness ratio (nose radius to base diameter) R/D = 0.1. The moment reference center is taken to be 0.3835 base diameters from the base and on the axis of symmetry. The reference area and reference length for all coefficients are the base area and base diameter respectively.

Also included in this report are data on a 25° pointed cone as a reference with which to compare blunted cone data. The moment reference, reference area and reference length are the same for both configurations.

3. Discussion of Literature

A complete listing of all the literature collected and reviewed is presented in the List of References, Section VI. The references are discussed below according to their content, i.e., whether the report contains experimental data or theoretical results, or a development of a theoretical method.

a. Experimental Data Reports

A summary of the contents of reports containing experiment force and moment data is presented in Table I, Part A. The table presents in semi-graphical form the experimental parameters presented in each report.

A review of Part A of Table I will show that the bulk of the experimental literature presents data for cone half angles of 20 degrees and less and bluntness ratios greater than 0.1. Since a unifying similarity parameter is not presently available which will correlate bodies of different cone angles and bluntness ratios, the use of much of the experimental data was severely restricted. Nevertheless, it was possible to glean from the reports sufficient data to establish with reasonable accuracy the aerodynamic coefficients.

b. Theoretical Data Reports

Part B of Table I briefly outlines the reports presenting results of a theory with direct application to pointed or blunt cones. These results include numerical solutions, closed-form solutions, graphical correlations, and empirical design charts.

4. Discussion of Theoretical Methods

During the study, several theoretical methods of calculation were investigated. Most of the theories were found to be applicable on a very limited basis for blunt bodies of small fineness ratios. The theories which were considered are as follows:

a. Lighthill Slender-Body Theory

b. Von Karman - Moore Linearized Theory

c. Basic Shock-Expansion Theory

d. Second-Order Shock-Expansion Theory

e. Modified Newtonian Flow Theory

f. Method of Characteristics

a. The Lighthill Slender-Body Theory was considered for application below a Mach number of 2.0 in the supersonic range. This method of calculation relates the local pressures to the variation of cross-sectional area and the slope of the body surface. The theory was actually developed for pointed nose bodies, but reasonable estimates of aerodynamic characteristics may be made using this method for some blunted nose bodies. The pressure coefficients at points far from the stagnation point (i.e., not applicable at stagnation point) may be calculated with reasonable accuracy for some blunt bodies. For bodies having a fineness ratio of 3.0, the theory yields values within a few percent of experimental data points over the aft 80% of the body. For a fineness ratio of 2.0, the errors are much larger - approximately 25% at the shoulder at $M = 1.8$, and 13% for $M = 1.4$. The entry body investigated in this study has a fineness ratio of less than 1.0; therefore, the accuracy would not be satisfactory even for the aft portion of the body.

b. The Von Karman - Moore Linearized Theory was applied to the body in an effort to establish the characteristics at low supersonic Mach numbers. The theory replaces the body of revolution by sources and sinks, with their strengths and distribution being determined by the body shape, and the surface local pressures are calculated by a step by step procedure using the following general equation:

$$C_p = \frac{2u}{V} - \left(\frac{v}{V}\right)^2 \qquad \text{(Ref. 54)}$$

where u and v are the perturbation velocities along and normal to the streamlines, respectively. The method proved inapplicable for bodies having small fineness ratios, and the equations only valid for very slender bodies.

c. The Basic Shock-Expansion Theory was considered for use at supersonic Mach numbers. This method of calculation defines the flow at the apex of a body by conical flow relations, and expands the flow downstream of this point by the use of Prandtl-Meyer expansion relations. A prerequisite for using the shock expansion method is that the bow shock must be attached, and the flow downstream of the shock is assumed to be two dimensional. The bow shock must be attached to apply the conical flow relations at the apex, and the theory requires that the flow is supersonic over the surface under consideration. The entry body considered here would not satisfy the above requirements; therefore, the accuracy of the values determined using this method is not acceptable.

d. Second-Order Shock-Expansion Theory

This theory is similar to the Basic Shock-Expansion Theory except that it is a higher order approximation. Generally speaking, the theory cannot be used to determine the aerodynamic characteristics of a sphere-cone for the same reasons that the Basic Shock-Expansion Theory cannot (i.e., the bow shock must be attached, supersonic flow must be present over the entire surface in question,etc.). An LTV IBM computer routine (LV-VC-13) was used to test the applicability of the theory to sphere-cones, and the data obtained were unsatisfactory. The only way this routine (Second-Order Shock-Expansion Theory) may be applied is to input the aerodynamic characteristics of the hemisphere nose into the routine by the use of a sub-routine, and then the theory will only be applied to the portion of the body in supersonic flow. Of course, this procedure is not beneficial, because the flow characteristics of the conical portion of the body may be easily obtained using several other methods.

e. Modified Newtonian Flow Theory was used to calculate the aerodynamic characteristics of the body at high supersonic and hypersonic Mach numbers. The theory assumes that the only particles of air affected by a body are those which undergo collision with the parts of the body facing the incident flow. On collision with the surface, the particles lose their normal component of momentum and then slide along the surface conserving their tangential component of momentum. The air particles have no effect on the portion of the body surface facing away from the flow (i.e. the pressure on the surface lying in the "aerodynamic shadow" is equal to zero). The theory has proved to yield values of acceptable accuracy for blunt bodies in many previous studies. The characteristics were calculated for the entry body in this study by the use of an IBM 7090 computer routine, LTV-LVVC26 (Ref. 11). The results agreed with the values of experimental data obtained in the literature survey and were used as a reference on some of the plots.

f. The Method of Characteristics was also considered for application. Though the method is more exact in the solution of the flow over a body than the previous mentioned approximation methods, the time required to apply the method is far greater than is allowed during this contract period. It would be unreasonable to use the method without having an applicable computer routine.

5. Presentation of Predicted Coefficients

Predicted aerodynamic coefficients are presented in Figures 2 through 12. The predictions are based on a compilation of experimental data and application of theoretical results. Each parameter is discussed below under a separate sub-section.

a. Newtonian Flow Solutions

Results of an IBM 7090 routine (Reference 11) programmed to obtain aerodynamic coefficients by integrating the Newtonian expression for pressure coefficient are presented in Figure 2. The Newtonian pressure coefficient is given by

$$C_p = C_p{}^* \sin^2 \sqrt{}$$

where $\sin \sqrt{} = \cos \alpha \sin \lambda + \sin \alpha \cos \lambda \cos \phi$

and $\sqrt{} = \frac{\pi}{2} - \frac{s_1}{R}$ on hemispherical nose

or $\sqrt{} = \psi$ on conical portion of body ,

$\lambda = \frac{\pi}{2} - \frac{s}{R}$ on hemispherical nose

or $\lambda = \theta$ on conical portion of body

b. Normal Force Coefficient

Figure 3 presents the normal force coefficient slope, C_{N_α}, versus Mach number and includes a comparison of all experimental data available for a 25° blunt (R/D = 0.1) cone and sharp cone. Also included are results of applicable theories.

An independence of bluntness is seen for Mach numbers less than M = 2. Very good correlation is seen for all sharp cone experimental data with the exact Taylor-Maccoll cone solution. This comparison lends confidence to the other experimental data. Excellent correlation is noted between the design chart data of Ref. 3 and the experimental data for both sharp and blunt cones for the lower Mach numbers.

A notable discrepancy between the data of References 1 and 8 is seen at Mach numbers less than M = 1. It was necessary to interpolate the data of Reference 8 to obtain points for $\theta = 25°$ and R/D = 0.1, whereas no interpolation was necessary for the data of Reference 1. Nevertheless, it did not seem advisable to disregard either set of data in favor of the other, hence both are presented.

Without significant error it may be assumed that C_{N_α} = constant up to $\alpha = 15°$ at all Mach numbers. This approximate linearity is verified in a number of references for a wide range of Mach numbers, cone angles, and bluntness ratios. Figure 4 presents a compilation of many experimental data points to test the linearity assumption. The figure presents C_N/C_{N_α} where C_{N_α} is the lift curve slope taken between $\alpha = \pm 4$ degrees. It is seen that up to $\alpha = 15°$ the variation from C_{N_α} = constant is less than 5%, and insufficient data exist to predict a variation with angle of attack other than a linear variation. Other references (2, 8, 9, 16, 17, 18 and 23) report similar observations without presenting supporting evidences.

c. Center of Pressure

By definition, the longitudinal center of pressure location is the intersection point of the axis of symmetry and the integrated force vector. At this point the axial force component of the integrated force vector does not produce a moment about the moment reference (assuming the moment reference is located on the axis of symmetry and the integrated force vector lies in the x-y plane) and the pitching moment coefficient is defined as

$$C_{M_\alpha} = C_{N_\alpha} \frac{\Delta X_{CP}}{D}$$

where ΔX_{CP} is the distance from the moment reference to the longitudinal center of pressure location, i.e. $\Delta X_{CP} = X_{CP} - X_{CG}$.

The vertical center of pressure location is defined as the intersection point of the Z-coordinate passing through the moment reference and the integrated force vector. At this point the normal force component passes through the moment reference, hence producing no moment, and the pitching moment coefficient is defined as

$$C_{M_\alpha} = \frac{\partial}{\partial \alpha} \left(C_A \frac{\Delta Z_{CP}}{D} \right)$$

where ΔZ_{CP} is the vertical distance from the moment reference to the vertical center of pressure location, i.e. $\Delta Z_{CP} = Z_{CG} - Z_{CP}$.

The longitudinal center of pressure variation with Mach number is presented in Figure 5. As predicted by Newtonian theory, Figure 2, the longitudinal center of pressure, ΔX_{CP}, does not vary with angle of attack. This is verified in References 8, 9 and 22, among other references, for both pointed and blunt cones. It should be noted that this characteristic is not general and is valid for cones of small bluntness and moderate cone angles.

For comparison, sharp 25° cone data are included in Figure 5. The theory curve is obtained from Stones pertubation to the Taylor-Maccoll solution (Ref. 9) and has been shown to check with experimental data very well for all cone angles less than $\theta = 50°$. The experimental points presented for the blunted cone were obtained from an interpolation of the data in the noted references. A discrepancy is seen between the data of Reference 1 and Reference 8 for sonic and subsonic Mach numbers. Both sets of data are presented since it did not seem advisable to disregard either one.

The variation of the vertical position of the center of pressure with angle of attack from Newtonian theory is seen in Figure 2.

d. Pitching Moment Coefficient

The pitching moment coefficient derivative, C_{M_α}, is shown as a function of Mach number in Figure 6. These data are obtained from Figures 3 and 5 as follows:

$$C_{M_\alpha} = C_{N_\alpha} \frac{\Delta X_{CP}}{D} \; , \; (\Delta X_{CP} = X_{CP} - X_{CG}) \; .$$

The discrepancies between References 1 and 8 which showed up in both C_N and X_{CP} data are transferred to the pitching moment data. The pitching moment data are resolved about the moment reference point shown in Figure 1.

e. Axial Force - Forebody Drag, Skin Friction Drag, Base Pressure Drag

The forebody axial force coefficient at zero angle of attack is presented as a function of Mach number in Figure 7. Experimental and theoretical results are presented from many sources for both sharp and blunt cones. These data do not include base pressure drag.

Integrated pressure data are presented from Reference 3 for a 25° sharp cone at $\alpha = 0$ and $0.7 \leq M \leq 2.0$ and from the pressure distribution data obtained from Division B of this report. The equation of integration was:

$$C_A = \int_0^1 C_p \; (\eta) \, d\eta$$

where $\eta = (r/R)^2$ and $C_p(\eta)$ is the pressure coefficient plotted as a function of η.

The data show that up to $M = 2$ the foredrag is practically independent of bluntness, for small bluntness ratios. Excellent correlation is noted between the integrated pressure data of Reference 3 and the integrated pressure data of Reference 4 (i.e., Taylor-Maccoll) at $M = 2.0$.

The dependence of forebody drag coefficient on angle of attack is shown in Figure 8. The ordinate is normalized using C_A at $\alpha = 0$ and data for many cone angles, bluntness ratios and Mach numbers are presented.

The skin friction drag coefficient variation with Mach number and Reynolds number is shown in Figure 9. These data were obtained from the flat plate solutions of Van Driest (Ref. 19) and modified to a 25° sharp cone using the so called "cone rule" developed by W. Mangler as presented in Reference 57.

Figure 10 presents accumulated base pressure drag data from many sources. For $M > 1$ the base drag coefficient is fairly independent of body shape provided that the boundary layer is turbulent at the base. For $M < 1$ the base drag coefficient becomes a complicated function of Reynolds number, Mach number and body shape.

In general, base pressure drag data obtained in wind tunnels are considered unreliable due to sting and wall interference effects. Consequently, many of the references presenting experimental data delete base pressure information. Reference 21 presents a semi-empirical method of calculating base pressure drag at all Mach numbers based upon a correlation of theory and experimental data for sharp and blunt cones at zero lift. Although the accuracy of the prediction method of Reference 21 is not stated the data were used extensively, to aid in the curve fairing of Figure 10.

A final drag curve, showing the total drag at zero lift, is shown in Figure 11. The total drag coefficient, C_{A_o}, is the summation

$$C_{A_o} = C_{A\alpha = o} + C_{A_f} + C_{A_b}$$

The median Reynolds number during re-entry is approximately 1.6×10^6, so all C_{A_f} values were taken at that Reynolds number.

f. Damping-In-Pitch Derivative

The damping-in-pitch derivative is presented as a function of Mach number in Figure 12. Reference 7 was used to establish a trend and the Newtonian solution was used to establish a level for the predicted curve. The variation of C_{M_q} with Mach number in the transonic regime is assumed to be qualitative, although not quantitative, and was established from observed behavior of similar bodies. Very little information was found in the literature to permit an accurate estimate of C_{M_q} at angles of attack different from zero.

6. Degree of Uncertainty

The estimated accuracy of predictions presented in Figures 2 through 11 is indicated as follows:

$\epsilon\, C_{M_\alpha}$ = $[\pm .0015$ for $0 < M < 0.7]$, $[\pm .0005$ for $0.7 < M < 4.0]$,
$[\pm .0008$ for $4 < M < 26]$.

$\epsilon\, X_{CP}/D$ = $[\pm 0.1$ for $0 < M < 1.1]$, $[\pm .01$ for $1.1 < M < 26]$.

$\epsilon\, C_{A_B}$ = $[\pm .05$ for $0 < M < 0.7]$, $[\pm .02$ for $0.7 < M < 4]$,
$[\pm .01$ for $4 < M < 26]$.

$\epsilon\, C_A$ = $[\pm .02$ for $0 < M < .6]$, $[\pm .01$ for $.6 < M < 3]$,
$[\pm .008$ for $3 < M < 26]$.

$\epsilon\, C_{M_q}$ = $[\pm .005$ for $0 < M < 2]$, $[\pm .002$ for $2 < M < 26]$.

These estimates are based upon correlation of experimental data, amount of data available, comparison with available theory, and an intuitive appraisal of data reliability.

B. Pressure Distribution Analysis

1. Summary

A technique is developed to predict the pressure distribution over a sphere-cone body at moderate angles of attack and supersonic Mach numbers, $M \geq 4$. The method is verified with experimental data from various sources.

The technique herein developed is applied to the problem of a sphere-cone with a 25° half angle conical skirt. The pressure distribution is predicted along meridian lines which converge at the axis of symmetry. Pressure coefficient variations are obtained at $\alpha = 0$, 5, 10 and 15 degrees, $M = 4$, 10 and 15, and along eight meridian lines using the so called "Modified Tangent Sphere-Cone" method.

2. Configuration Description

For the purpose of this division the configuration under study is a semi-infinite spherically tipped conical frustrum. Points on the surface are located by two coordinates, s/R and ϕ. The major symbols used are identified in the sketch of Figure 13.

3. Discussion of Literature

An extensive literature survey was conducted during this study in search of pressure data, both experimental and theoretical, related to sphere-cones. A very limited amount of experimental data were available, and the majority of the theoretical data were for zero angle of attack only. A complete summary of the results of the survey is presented in Table II.

One of the most comprehensive pressure data sources found during this study was Reference 61. These data were obtained from detailed characteristics solutions on sphere-cones at various Mach numbers. Pressure coefficients are tabulated as a function of normalized surface distance (C_p vs. s/R), at zero angle of attack. The pressure distributions were given for cone angles of 0, 5, 10, 20, 30 and 40 degrees, and for Mach numbers of 3, 4, 6, 10 and infinity. These data are presented in Figures 14 through 17 for the various cone angles, and interpolated curves for additional cone angles are also included.

Figure 15 presents a comparison of theoretical and experimental data at Mach numbers near 6. Experimental data from Reference 71 are compared to theoretical data for cone angles of 10, 20 and 40 degrees at M = 5.8. Experimental data from Reference 69 for θ = 15 degrees and M = 6 compare favorably with interpolated curve shown in Figure 15. Other comparisons between experiment and theory are shown in Figure 17.

Comparisons between theoretical results are shown in Figure 18. Data from References 66, 67 and 68 are compared to data from Reference 61. Agreement is shown to be very close between all theoretical results. The small variations between theories are believed to be due to real gas effects. It should be noted that Reference 67 uses, as a correlation parameter, the specific heat ratio behind a normal shock wave. For presentation of these data in Figure 18 a specific heat ratio of 1.22 was used. Theoretical data from Reference 65 are shown also in Figure 15 for cone angles of 7.96 and zero degrees.

The close agreement between experimental and theoretical data from several sources tends to verify the validity of the theoretical data from Reference 61.

Figure 19 presents (for a 15° sphere-cone at α = 10°), a comparison of experimental data to theoretical values calculated by the method used to obtain the final predicted pressure variations. A similar comparison is made in Figure 20 for a 40° cone at $\alpha = 8°$. The close agreement of the values indicate that the method used herein to establish the pressure distribution of the 25° sphere-cone is valid. This method is discussed in detail in the next section.

In addition to the data obtained in the literature survey, an attempt was made to apply two LTV computer routines (References 11 and 40), but the data did not prove satisfactory, therefore, were disregarded.

4. Method of Pressure Prediction

a. Basic Tangent Sphere-Cone Method

As stated before, Reference 61 includes a very comprehensive and detailed pressure distribution analysis on sphere-cones at several Mach numbers. It was decided to utilize the data in Reference 61 as much as possible by interpolating the results to include other cone angles. The results of the interpolation are shown in Figures 14 through 17. Included in the interpolated data is the pressure distribution on a 25° sphere-cone at zero angle of attack and four Mach numbers.

A method very similar to the "tangent-cone theory" was used to predict the pressure variation along a meridian line at angles of attack. This method, in its simplest form, is to calculate the included angle between the meridian line on the cone surface and the free-stream velocity vector (call this angle ψ) and to use the data from Figures 14 through 17 corresponding to the angle ψ as the pressure variation along the meridian line. From spherical trigonometry the relation between ψ, α, θ and ϕ is

$$(1) \qquad \sin\psi = \cos\alpha \sin\theta + \sin\alpha \cos\theta \cos\phi .$$

This simplified method assumes that the streamlines near the body radiate from the stagnation point along a meridian path to the sphere-cone junction where they are abruptly turned to follow a conical ray. Consequently, the circumferential pressure distribution around the conical portion is established solely from flow expansion over the hemispherical nose, and the effects of cross flow are neglected. The errors involved with this method vary directly with angle of attack and inversely with Mach number.

In order to reduce the errors at high angles of attack a correction was applied to the basic tangent-sphere-cone method described above. The correction essentially introduced a crossflow term to the conical portion of the body sufficiently far downstream of the nose and extended the correction upstream to the sphere-cone junction. A more detailed explanation of how this correction was derived and applied will be given following a discussion of the pressure distribution on the spherical portion of the sphere-cone body.

b. Pressure Distribution On Spherical Nose

A number of authors have obtained solutions to the hemispherical blunt body problem. Notable solutions are found in References 61, 63, 65, 66 and 68. Figure 21 presents the data from Reference 61 which is identical to the solutions from the various other sources. These data are presented for several Mach numbers and a comparison is made with Newtonian theory.

The hemispherical pressure distribution presented in Figure 21 is shown for zero angle of attack, i.e. the stagnation velocity vector is coincident with the longitudinal reference axis.(For a sphere-cone body of revolution the longitudinal reference axis is also the axis of symmetry).

Thus streamlines and meridian lines are coincident at zero angle of attack, and the pressure distribution is symmetrical about the longitudinal reference axis. For cone half angles $\theta < 45°$ and $M > 3$ the sphere-cone junction is located in locally supersonic flow, hence the conical skirt has no effect on the pressure distribution over the spherical portion up to the sphere-cone junction.

At angles of attack (zero yaw) the stagnation point moves along the vertical meridian a distance

(2) $$\frac{s}{R} = \alpha \text{ (radian)} .$$

Streamlines then radiate from the stagnation point in a symmetrical pattern about the stagnation velocity vector for a distance

(3) $$\frac{s_1}{R} = \left(\frac{\pi}{2} - \theta - \alpha \right)$$

which is the arc distance from the stagnation point to the sphere-cone junction at $\phi = 0$. Analytical results were not available to predict a pressure variation along the streamline path between $\frac{s_1}{R} = \left(\frac{\pi}{2} - \theta - \alpha \right)$ and $\frac{s_1}{R} = \frac{\pi}{2} - \psi$ (sphere-cone junction) for meridians other than $\phi = 0$. For the purpose of this report it is assumed that all streamlines follow exactly a meridian path between the stagnation point and the sphere-cone junction, and that the pressure variation along the path is given by the data in Figure 21. The validity of this assumption should be investigated further although it is believed that for moderate angles of attack the assumption yields good accuracy.

It now remains to compute the pressure distribution along meridian lines on the hemispherical nose. The relation between the sides and angles of an oblique spherical triangle is

(4) $$\cos \frac{s_1}{R} = \cos \frac{s}{R} \cos \alpha + \sin \frac{s}{R} \sin \alpha \cos \phi .$$

Using this equation for a given α and meridian line defined by ϕ a relation between $\frac{s_1}{R}$ and $\frac{s}{R}$ is obtained. Then, the pressure at any point $p(\frac{s}{R}, \theta)$

can be found by first finding its distance from the stagnation point, $\frac{s_1}{R}$, and then take the pressure corresponding to this distance from Figure 21.

Figures 22 through 24 present the pressure coefficient variation along eight meridian lines (ϕ = 0, 30, 60, 90, 180, 210, 240, 270) to $\frac{s}{R} = 1.1$ for angles of attack of 5, 10, and 15 degrees and for $M \geqslant 15$. Data for other Mach numbers can easily be obtained using equation (4) and the method described above, although as seen in Figure 21 there is little dependence on Mach number except near the stagnation point.

c. Modified Tangent Sphere-Cone Method

As mentioned before, the pressure distribution along a conical ray of a sphere-cone body at angles of attack can be determined approximately using the tangent sphere-cone theory described earlier. This theory may be improved somewhat by obtaining the actual circumferential pressure distribution on a sharp cone at angles of attack and applying the results sufficiently far downstream from the nose.

Reference 62 presents a method of predicting the circumferential pressure distribution on a sharp cone at angles of attack. The method is semi-empirical in nature and the pertinent equations are reproduced here. The circumferential pressure distribution is given by

$$(5)\quad \frac{C_p}{C_{p\phi=0}} = 1.1\cos^3\frac{3\xi}{4} + .00097\xi - .15\cos^3(\alpha+\theta)\sin^3\xi - 0.1$$

where

$$(6)\quad \cos\xi = \frac{\sin\psi}{\sin(\alpha+\theta)}$$

and $C_{p\phi=0}$ is the pressure coefficient on the vertical windward meridian and is given by

$$(7)\quad C_{p\,\phi=0} = K\sin^2\frac{(\alpha+\theta)\,\pi/2}{\alpha_{P_{max}}+\theta}\ .$$

Equation (7) is modified somewhat from that presented in Reference 62 so that $C_{p\,\phi=0}$ will reduce to the exact cone pressure at $\alpha = 0$. Thus,

$$(8)\quad K = C_{p\alpha=0}\sin^2\frac{\theta\,(\frac{\pi}{2})}{\alpha_{P_{max}}+\theta}$$

where $C_{p\alpha=0}$ is the exact cone pressure from Reference 4 and $\alpha_{P_{max}}$ is a function of cone angle and Mach number given on a chart in Reference 62. For $\theta = 25^\circ$ and $M = \infty$, 7, 4 and 3, $\alpha_{P_{max}}$ = 57.0, 55.9, 54.0 and 51.9 respectively. The circumferential pressure distribution can now be found from

$$(9)\ C_p = C_{p\phi=0}\left[\frac{C_p}{C_{p\phi=0}}\right]$$

using equations (5) and (7). The results for $\theta = 25°$, four angles of attack and three Mach numbers are presented in Figures 25 through 27.

The pressure distribution on the conical skirt of a sphere-cone body far downstream from the nose approaches the sharp cone values. This is seen in Figures 14 through 17 at $\alpha = 0$ where the sharp cone asymptote value for each curve is obtained from the tables of Sims or Kopal. It follows, then, that at angles of attack the circumferential pressure distribution of a sphere-cone body will approach that of a sharp cone sufficiently far downstream from the nose. An assumption must be made, however, to extend these sharp cone data into the region of overexpansion. This report assumes that the difference between the tangent-cone asymptotic pressure coefficient (i.e. the pressure coefficient on a sharp cone of cone angle ψ) and the actual pressure coefficient obtained from Figures 25 through 27 is applied as a linear function of $\frac{s}{R}$ between the sphere-cone junction and the asymptotic tangency point obtained from the tangent sphere-cone method.

Mathematically, the pressure coefficient at any point on the cone between the sphere-cone junction, $\frac{s}{R} = \frac{\pi}{2} - \theta$, and the asymptotic tangency point, $(\frac{s}{R})_T$, is given by

$$(10)\quad C_p = C_{pTC} - \Delta C_p\left[\frac{\frac{s}{R} - \frac{\pi}{2} + \theta}{(\frac{s}{R})_T - \frac{\pi}{2} + \theta}\right]$$

where C_{pTC} is the pressure coefficient given by the tangent sphere-cone method from Figures 14 through 17.

$C_{p\phi}$ is the sharp cone circumferential pressure coefficient given in Figures 25 through 27.

ΔC_p is the difference between C_{pTC} at $(\frac{s}{R})_T$ and $C_{p\phi}$; i.e. $\Delta C_p = (C_{pTC} - C_{p\phi})$ at $(\frac{s}{R})_T$, and $(\frac{s}{R})_T$ is the tangency point where the pressure coefficient in the overexpansion region reaches the sharp-cone value.

obtained from Figures 14 through 17. Predicted pressure coefficient data on a 25° sphere-cone at angles of attack up to 15° obtained by this method are presented in Figures 28 through 39.

A check on the validity of the method used is shown in Figure 19 for a 15° sphere-cone body. Experimental data from Reference 62 is compared to the present method and to the "Tangent Sphere-Cone" method. Unfortunately, experimental data on the leeward side of the body were not available. Experimental data for a 15° sharp cone are also included as a check on the predicted circumferential pressure distribution.

The only other experimental data suitable for analysis were found in Reference 71. These data were for a 40° sphere-cone at $\alpha = 8°$ and comparison with the predicted results is shown in Figure 20. It is believed that the discrepancies are largely due to viscosity effects.

5. Presentation of Final Predicted Pressure Coefficients

Figures 28 through 39 present the final predicted pressure coefficient data on a 25° sphere-cone. These data were obtained using the "Modified Tangent Sphere-Cone" method described in section 4.c. Pressure varations are presented along meridian lines eminating from the axis of symmetry for several meridian lines, angles of attack, and Mach numbers.

Specifically, Figures 28 through 36 present the pressure variation along eight meridian lines, each at $\alpha = 5$, 10, and 15 degrees and Mach numbers 4, 10, and 15. Figures 37 through 39 present data in the vertical meridian plane ($\phi = 0$ and 180), each at $\alpha = 0$, 5, 10, and 15 degrees and Mach numbers 4, 10, and 15.

6. Degree of Uncertainty

Although flow solutions by the method of characteristics are considered the most exact solutions thus far obtainable, viscosity effects are neglected. In most cases these effects are small enough to neglect, but under certain conditions these effects may be considerable, for example $\theta = 40°$, Figure 15. For large cone angles the shock wave lies close enough to the conical afterbody to induce a possible boundary layer-shock wave interaction. Thus, the accuracy of prediction is believed to suffer most along the windward meridian ($\phi = 0$) at high angles of attack.

Except in the vicinity of the sphere-cone junction where the viscosity effects are most noticeable, the expected mean prediction accuracy is $C_p = \pm 0.015$. This accuracy figure is based upon a correlation of experiment and theory and an intuitive appraisal of test results, validity of assumptions, and anticipated viscosity effects.

C. IMPACT DISPERSION STUDY

1. Summary

This division presents the results of an anlysis undertaken to define the re-entry path angles which produce, for a given set of booster burnout deviation, one, two and three sigma total impact range deviations of 400 n. mi. Utilizing a standard NASA Scout configuration, a nominal boost trajectory was developed which satisfies each of the above derived re-entry path angles. The nominal trajectory corresponding to the two sigma re-entry angle (which produces a range deviation of 400 n. mi.) was then used as a basis for an accuracy analysis. The boosters errors were separately imposed upon the trajectory and the burnout and impact deviations statistically combined to define the standard deviations in burnout and impact conditions for this particular re-entry angle.

The Scout booster vehicle configuration used in this analysis consisted of the following rocket motors.

Stage One	-	Algol IIB
Stage Two	-	Castor II
Stage Three	-	ABL X 259
Stage Four	-	ABL X-258

2. Impact Dispersion Study

The first part of this study was to determine the entry path angle which, for a given set of booster burnout deviations, would produce one, two and three sigma impact range deviations of 400 n. mi. The standard deviations and correlation coefficients used in these computations were defined in Reference 92 and are:

Standard Deviations	Correlation Coefficients
V (velocity) = 62.3 ft./sec.	$\rho_{\Delta V \Delta h} = -.1705$
h (altitude) = 3.24 n. mi.	$\rho_{\Delta V \Delta \gamma} = -.179$
γ (entry angle) = .293 degrees	$\rho_{\Delta h \Delta \gamma} = .706$

Impact range deviations were calculated on a three degree-of-freedom trajectory routine (Reference 93) which incorporates an oblate rotating spheroid earth model and a 1962 ARDC atmosphere model. The nominal entry velocity and altitude were assumed to be 26,000 ft./sec. and 433,000 feet, respectively. Figures 40, 41 and 42 show impact range deviations as functions of velocity, altitude and flight path angle deviations for several nominal entry path angles (the angle between the local horizon and the vehicle air relative velocity vector).

Range deviations obtained by separate statistical combinations of one, two and three sigma velocity, altitude and path angle errors are shown in Figure 43. Positive and negative range deviations were combined separately to show the non-symmetry of the impact distribution.

Total range deviation was plotted as a function of nominal entry flight path angle and is shown in Figure 44. Entry angles corresponding to one, two and three sigma total range deviations of 400 n. mi. were found to be -3.44 degrees, -4.53 degrees and -5.77 degrees, respectively. A nominal Scout "gravity turn" boost trajectory was designed which achieved the -4.53° entry angle along with an entry velocity of 26,500 ft/sec at an altitude of 433,000 ft. A range altitude profile of this nominal trajectory is shown in Figure 45. Gravity turn trajectories for the -3.44° and -5.77° entry angles were also computed to determine the variation of total range to impact as a function of nominal angle. This variation is shown in Figure 46.

3. Impact Dispersion Analysis

An impact dispersion analysis was performed for the -4.53 degree entry angle. The effect of each significant booster error source on final burnout conditions of the Scout booster as well as impact range of the payload was determined by trajectory calculations separately incorporating each error source. These calculations were combinations of six and three-degrees of freedom trajectory simulations. The first stage of the boost vehicle was simulated in six-degrees of freedom in order to accurately simulate the launch dynamics and the effects of winds and thrust misalignment. A three-degree of freedom simulation was adequate for the upper stages and was used in order to conserve machine computational time.

The results of these calculations are shown in Table III. The deviations from the nominal value of the re-entry parameters of velocity, altitude, flight path angle, angle of attack and impact range are shown for each error source. For most of the error sources both the plus and minus 3 sigma values were run. The RSS value is based on an average of the plus and minus deviations, since they are essentially linear. It is of interest to note that the largest velocity errors are those produced by fourth stage motor data, winds and second stage deadband errors. The significant altitude errors are caused by first and second stage motor data, drag variations and second stage deadband errors. Angle of attack and flight path angle deviations are most strongly a function of guidance, deadband and tip-off errors. The impact range deviations are influenced strongly by most of the errors with the exception of winds, thrust misalignment and fourth stage motor data. The bottom line on Table III shows the RSS value of the average values.

Standard deviations in each of the important fourth stage burnout parameters were computed from Table III using the RSS technique and are shown below.

Parameter	Standard Deviation
Velocity	61 ft/sec
Altitude	2.70 n. mi.
Flight path angle	.25 deg.
Range	2.60 n. mi.
Angle of attack	.382 deg.

Correlation coefficients were computed as described in Reference (92) and were found to be

$$\rho_{\Delta V \Delta h} = -.118$$
$$\rho_{\Delta V \Delta \gamma} = -.042$$
$$\rho_{\Delta h \Delta \gamma} = .664$$

The "two sigma" total deviation in impact range was computed by root sum squaring the average deviation produced by each error source and was found to be 374 nautical miles. Root sum squaring positive and negative deviations separately resulted in "two sigma" deviations of +205 n. mi. and -169 n. mi. An estimate of the "two sigma" range dispersion as a function of nominal entry angle appears in Figure 47. This estimate is based on the burnout deviations and correlation coefficients for the -4.53 degree entry angle rather than those from Reference 92.

D. Reentry Dynamics Study

1. Summary

This division presents the results of a study of the reentry dynamics of the subject vehicle. Reentry trajectories were computed to determine the most aft center of gravity limit which would cause angle of attack excursions not to exceed 2 degrees and to investigate the effects of tip-off, mass unbalance, and center of gravity off-set. A roll-pitch frequency analysis was conducted to determine the natural frequencies of the vehicle and to define regions of roll-pitch resonance.

2. Trajectory Analysis

A six (6) degree of freedom digital computer study was conducted to investigate the effect of center of gravity location on the dynamic behavior of the spacecraft during descent through the atmosphere. On the basis of this study, a nominal center of gravity was selected and additional trajectories were computed to determine the individual effects of tip-off, mass unbalanee and center of gravity offset on the angle of attack envelope. Data are presented which show the effect of center of gravity location and of each of the disturbances on the angle of attack envelope.

a. Simulation

The entry vehicle was simulated as a six (6) degree of freedom rigid body using the LTV NEMAR trajectory routine. This routine is described in detail in Reference 93.

Mass unbalance was simulated as an I_{xz} product of inertia. Since the basic NEMAR routine does not have provision for including a product of inertia term the equation for calculating body axis angular rates (equations 4.04 of Reference 93) were modified as follows,

$$P = (H_x I_{zz} + H_z I_{xz})/(I_{xx} I_{zz} - I_{xz}^2)$$

$$Q = H_y / I_{yy}$$

$$R = (H_z I_{xx} + H_x I_{xz})/(I_{xx} I_{zz} - I_{xz}^2)$$

where H_x, H_y, H_z are the components of angular momentum of the vehicle about its body axes in ft/lbs; I_{xx}, I_{yy}, I_{zz} are the moments of inertia of the vehicle about the body axes in slugs ft^2; I_{xz} is the product of inertia between the x and z body axes in slugs ft^2.

A center of gravity offset was simulated as a displacement of the center of gravity along the negative z-axis measured from the axis of symmetry, as defined in Figure 1. Thus, an additional x-axis moment of (Z_{cg} N_y) and an additional y-axis moment of (Z_{cg} N_x) were introduced into the NEMAR time rate of change of angular momentum equations (equations 4.03, Reference 93).

The following vehicle characteristics were used in the simulation.

Weight - 192 lbs.

Pitch and yaw moments of inertia - 4.2 slug ft^2

Roll moment of inertia - 3.2 slug ft^2

Diameter - 2.5 ft.

Base Area - 4.9 sq. ft.

Axial force coefficient vs. Mach no. - Figure 11

Normal force derivative vs. Mach no. - Figure 3

Center of pressure vs. Mach number - Figure 5 (Fwd value)

Pitch damping derivative vs. Mach number - Figure 12

b. Effect of Center of Gravity Location

The purpose of this analysis is to determine an acceptable aft center of gravity limit. The criteria for an acceptable limit is that the angle of attack envelope not exceed two degrees, especially in the regions of high heating and high loads.

A reference trajectory was computed using the center of gravity specified in Reference 91, 0.3835 diameters forward of the base. Values from this trajectory were then used to explore the low speed regime to define an acceptable aft center of gravity limit since in this region the vehicle exhibits the least stability.

Center of gravity locations of 0.20 D, 0.24 D and 0.28 D were selected and trajectories computed using the following initial conditions. These conditions correspond to a time of 243.2 seconds after burnout as determined in the final nominal trajectory.

Mach Number	1.16
Altitude	67909 ft.
Relative Flight Path Angle	-34.099 degrees
Spin Rate	3 cps

The initial pitch and yaw rates were zero as well as the roll angle and aerodynamic angle of attack. A mass unbalance of 20 oz-in^2 was included.

Angle of attack time histories for these trajectories are shown in Figure 48. The 0.20 D and 0.24 D CG positions were found to cause divergence and were abandoned. The 0.28 D position did not diverge but did reach a large maximum angle of attack which appeared unacceptable. Consequently, this case was re-computed starting with burnout conditions to insure that results from the short runs, starting at M = 1.16, were valid. The results of this latter run, shown in Figure 49, correlate well with the data of Figure 48 and show that the short runs provide valid results.

Unless otherwise specified, the initial conditions are those which exist at burnout. These conditions are listed below.

Mach number	16.42
Altitude, ft.	433,226
Relative Flight Path Angle, deg.	-4.530
Relative velocity, ft/sec	26,500
Angle of Attack, degrees (3 sigma value)	1.15

A tip-off of 1 lb-sec, acting at the separation plane, and a mass unbalance of 20 oz-in.^{2} were included as specified in Reference 91. The vehicle was initially oriented (roll angle = 90°) so that both the mass unbalance and initial pitch rate (due to tip-off) tend to initially cause a positive angle of attack. In other words, all disturbances and initial conditions were oriented or produce the largest possible angle of attack. The initial spin rate is 3 cps.

As a result of these exploratory studies, a CG of 0.32 D was selected as a probable aft limit. A trajectory was computed for this case, starting from burnout. The angle of attack time history, presented in Figure 49, was considered to be satisfactory. Consequently, a CG position of 0.32 D was selected as the aft limit and used for all of the subsequent analyses. The initial angle of attack shown on Figure 49 is 1.15 degrees plus the effect of the 1 lb/sec tip-off impulse. Since the tip-off impulse produces a different moment for different CG positions the initial angle of attack is different for the two runs shown.
The initial angle of attack buildup (Figure 49) is due to a downward rotation of the velocity vector that occurs before the dynamic pressure

attains sufficient magnitude to cause the aerodynamically stable vehicle to tend to follow the velocity vector. The c.g. position has very little effect on the magnitude and damping of this initial angle of attack buildup. After a higher dynamic pressure is reached the angle of attack is reduced essentially to zero. (This initial angle of attack buildup could be avoided by programming the booster so that burnout occurs at a slightly negative angle of attack of approximately 4.5 degrees. The normal rotation of the velocity vector would then reduce the angle of attack to zero after approximately 80 seconds.) The angle of attack then remains very small until a lower Mach number is reached and the center of pressure shift reduces the stability of the vehicle to the extent that the vehicle cannot follow a rapidly pitching velocity vector. Subsequently, the pitch rate of the velocity vector reduces and the aerodynamic stability again reduces the angle of attack to a small value. The magnitude of this low speed angle of attack buildup is dependent on the aerodynamic stability and thus, is obviously very strongly related to the c.g. position.

The Mach number and dynamic pressure for these trajectories are presented in Figure 50.

The ranges of accelerations at the CG and body axis angular rates as determined from these trajectories are shown below,

	X_{cg} = .28D	X_{cg} = .32D
Accelerations (g's)		
Longitudinal	0 to 11.4	0 to 11.4
Normal and traverse	+.85 to -.85	+.45 to -.45

	X_{cg} = .28D	X_{cg} = .32D
Body axis angular rates (deg/sec)		
Pitch and Yaw	+65 to -65	+40 to -40
Roll	1080	1080

These trajectories incorporated the 1 lb-sec tip-off impulse and 20 oz-in^2 mass unbalance disturbances.

c. Nominal Trajectory

In order to determine the effects of individual disturbances on the angle of attack envelope, a trajectory with no disturbances is required as a reference. A nominal no-disturbance trajectory was computed using the burnout initial conditions except that the initial angle of attack was zero. The angle of attack envelopes for the nominal trajectory and disturbance trajectories are shown in Figure 51, 52, and 53. It is interesting to note that the Mach number and dynamic pressure time histories for these cases show no significant variation from those presented in Figure 50.

In the following paragraphs, which discuss the effects of individual disturbances, all conditions are the same as for the nominal case except as noted.

d. Effect of Tip-off

The effect on the angle of attack envelope of a tip-off impulse of 2 lb-sec. acting at the separation plane is shown in Figure 51. The 2 lb.-sec. tip-off impulse was simulated as an initial pitch rate of -21.8 degrees with the vehicle initially rolled 90 degrees to cause the displacement of the cone center to be upward and thus have the greatest effect on angle of attack. The nearly constant increment in angle of attack seen in Figure 51 is due to the coning motion and the upward displacement of the cone center. When the region of high dynamic pressure is reached the coning motion is damped and the angle of attack is reduced to zero. The remaining portion of the angle of attack envelope is not affected by the initial tip-off impulse.

e. Effect of Mass Unbalance

The effect of a 50 oz. in.^{2} mass unbalance (I_{xz} = .000 675 slug ft.^{2}) is shown in Figure 52. The 1.5 degree deviation from nominal that occurs at 118 sec. is due to roll pitch resonance. This motion is quickly damped and should be of no particular consequence. In the low Mach number region the low aerodynamic stability allows the mass unbalance to produce a slight coning motion which increases the angle of attack envelope by approximately 0.8 degrees.

f. Effect of Center of Gravity Offset

Preliminary trajectory calculations with center-of-gravity offsets of 0.1 and 0.2 inches indicated that a vehicle with a c.g. offset would rather closely follow the nominal angle of attack histories except in regions of roll-pitch resonance which occur at approximately 120 seconds and 235 seconds. During these regions the preliminary trajectories indicated that large deviations in angle of attack occurred; however, due to the amplitude and frequency of the motion involved the integration error control used in these preliminary calculations was judged to be inadequate for accurately defining the amplitudes of these deviations. It is interesting to note that the integration error control that was adequate for calculating the motion resulting from the other disturbances was not suitable for calculating the motion resulting from a c.g. offset. This is so because for a given error control (truncation error control) more integration steps are required for a cg offset run than for say a mass unbalance run. Therefore, for a given period of trajectory time the cg offset run will require more integration steps. The larger number integration steps produce a larger accrued build-up in truncation error in the variables of integration. To control this accrued error the error control must be tightened (allow a smaller truncation error) but this process requires smaller integration steps and hence longer computational times result for the same period of trajectory time. Since tightening the error control to a suitable level resulted in an almost prohibitive computer time requirement for an entire trajectory, trajectories were computed only in the region of roll-pitch resonance. Trajectories starting at 80 seconds and ending at 160 seconds were run to define the response to the roll-pitch resonance that occurs at a high Mach number and trajectories beginning at 220 seconds and ending at 280 seconds were run to define the response to the low speed region of roll-pitch resonance. The initial conditions for the low speed region trajectories were based on preliminary computer runs. Trajectories of this type were run for c.g. offsets of 0.1, 0.2 and 0.3 inches. Results of these calculations are shown in Figure 53. It can be seen from Figure 53 that the response to roll-pitch resonance in the high speed region is very nearly linear while the response in the low speed region is obviously very non-linear. The non-linear response that occurs in this region is evidently due to a reduction in spin rate that accompanies the large amplitude deviation in angle of attack. Spin rate reduction is shown in Figure 54. This spin rate reduction is due to the rolling moment produced by the side forces acting at the offset c.g. The vehicle maintains a coning rate approximately equal to the spin frequence so that the vehicle x and y axes maintain the same general orientation relative to the angle of attack plane (plane formed by the vehicle X body axis and the relative velocity vector). For the three cases shown the vehicle maintained an orientation with the negative y body axis lying near the angle of attack plane so that a negative rolling moment was produced by the side force. Further work needs to be done to determine whether or not the vehicle will always settle into this orientation so that the spin rate is always reduced or if it is possible for the vehicle to remain with the positive y axis oriented within the angle of attack plane so that the spin rate will be increased.

3. Roll-Pitch Frequency Analysis

Roll-pitch frequencies have been computed for the nominal trajectory and for several off-nominal cases. These frequencies are those which will appear on the body axes. The off-nominal cases considered are center of gravity off-sets of 0.2 and 0.3 inches and a center-of-pressure location which is more aft than that used in the nominal case.

a. Method

The method used for calculating the roll-pitch frequencies is a modification of the equations developed by Phillips in Reference 95. Phillips developed the equations for a case where the mass could be assumed to be distributed in a plane, as for an airplane. Using the same approach, equations have been derived for the case of the mass distributed symmetrically about the longitudinal axis of the body.

Since the reentry body being analyzed herein is both aerodynamically and inertially symmetric about the spin axis, the equations can be further simplified by combining the terms containing the aerodynamic moment. These conditions result in the following equation for body fixed frequencies.

$$\Omega_{1,2} = P\left\{\omega^2 + \frac{1}{2}\sigma^2 - \sigma + 1 \pm \frac{1}{2}(\sigma - 2)\sqrt{(\sigma^2 + 4\omega^2)}\right\}^{\frac{1}{2}}$$

where: Ω_1 = the high body frequency

Ω_2 = the low body frequency

ω = the non-spinning pitch frequency divided by the spin frequency

σ = the ratio of roll inertia to pitch inertia = 0.762

P = the spin frequency

Before proceeding to the numerical analysis of this spinning body some of the characteristics of the above equation will be discussed.

When: $\omega = 0$ (corresponding to no aerodynamic moments) the equation reduces to

$\Omega_1 = P$

$\Omega_2 = (1 - \sigma)\ P$ or $(\sigma - 1)\ P$

These are the spin frequency and the coning frequency for a spinning body in a vacuum.

When $\omega \rightarrow \infty$ (corresponding to a case of zero spin rate) both frequencies approach ω, indicating that only the non-spinning pitch frequency is present.

Roll-pitch resonance can occur when either of the frequencies become equal to zero. Since the high frequency is always equal to, or larger than, the spin frequency, this can only occur for the low frequency. It can be shown that the low frequency can never be less than zero but it can equal zero. The latter case represents roll-pitch resonance and occurs when $\omega = \sqrt{1-\sigma}$

Substituting the inertia ratio into the frequency equation provides a numerical equation for the two frequencies as follows

$$\Omega_{1,2} = P\left\{\omega^2 + 0.5283 \pm \sqrt{0.2225 + 1.5326\,\omega^2}\right\}^{\frac{1}{2}}$$

A plot of this equation is presented in Figure 55. The low frequency goes to zero at $\omega = 0.486$ indicating roll-pitch resonance at this value of ω.

b. Results for Nominal Case

Figure 56 presents a time history of ω for the nominal trajectory (Figure 50) and for several off-nominal conditions. For the nominal trajectory, a spin rate of three cycles per second was used. For the cases with a CG off-set, the spin rate was taken from Figure 54. For these cases the spin rate steadily decreased after 220 seconds.

The frequency ratio for the nominal trajectory passes through roll-pitch resonance at 120 seconds and again at 236 seconds. The time spent near the resonant condition is short and the buildup in angle of attack is small as shown in Figure 51. For the cases with mass unbalance a small increase in angle of attack is noted near resonance (Figure 52).

c. Results for Off-Nominal Cases

The frequency ratio for the nominal trajectory with an aft center of pressure (Figure 56) is slightly higher than that for the nominal case. This is, of course, simply due to increasing the static margin, hence making the system stiffer. Using the aft center of pressure does not produce catastrophic roll-pitch resonance; however, it can be seen that the aft CP in conjunction with a CG off-set could cause a resonance condition for a considerable period after about 260 seconds.

The effects of CG off-set on the frequency ratio are profound at the low speed end of the trajectory. This is due to a significant reduction in spin rate after 220 seconds. The spin rate at 280 seconds is 2.1 cps for the 0.2 case and 0.23 cps for the 0.3 case. Although neither of the cases shown herein seem to have a roll-pitch resonance problem per se, it appears from these data that some combination of CG off-set and/or static margin, within the range of values considered, could very well produce a resonant condition for all or part of the period after 260 seconds.

The reduction in spin rate is caused by a rolling moment due to sideslip. As the angle of attack builds up after 220 seconds, the angle of sideslip tends to be biased in a positive direction. This produces a side force which causes a rolling moment since the force does not act through the center of gravity. Positive bias of the sideslip angle occurred for all of the cases with a CG off-set and may be an inherent characteristic of the body in the low speed flight regime.

The body frequencies are presented in Figures 57 and 58 for the nominal trajectory with a spin rate of 3 cps. These frequencies were obtained from the data presented in Figures 55 and 56. As discussed above, roll-pitch resonance occurs when the low frequency (Figure 57) goes to zero. The high frequency can never produce resonance although it is near the spin frequency for a considerable portion of the flight.

d. Conclusions

The results of this analysis show that roll-pitch resonance is not a problem for the cases considered. However, there is a potential problem area at the low speed end of the flight. Roll-pitch resonance could develop in this area if the static margin is too large or for some combination of static margin and CG off-set within the range considered.

CONCLUSIONS

In keeping with the major divisions of this report the following conclusions are drawn:

A. Aerodynamic Stability Analysis

1. Aerodynamic stability coefficients have been predicted for a 25° blunt and sharp cone using data available from technical literature.

2. The accuracy of prediction is considered to be generally good for Mach numbers greater than unity.

3. A marked discrepancy was discovered between data of References 1 and 8 for X_{cp} and C_{N_α} at subsonic Mach numbers. This lack of correlation renders an accurate prediction impossible based on these data.

4. The most notable information void exists for dynamic stability data at all Mach numbers and angles of attack.

5. Although much data are available for a wide range of sphere-cone configurations and flow parameters, much additional data are needed before these parameters can be completely correlated to allow accurate interpolations.

B. Pressure Distribution Analysis

1. Complete pressure distribution data have been predicted for a 25° spherically blunted cone at Mach numbers 4, 10 and 15 and at angles of attack 0, 5, 10 and 15 degrees.

2. A general method of pressure prediction at angles of attack was developed using axi-symmetric sphere-cone characteristics solutions and an adjustment for cross flow.

3. The accuracy of the "Modified Tangent Sphere-Cone" method of pressure prediction is considered good.

CONCLUSIONS (Continued)

C. Impact Dispersion Study

1. The entry angles which correspond to one, two and three sigma total range deviations of 400 n.mi. were determined to be -3.44, -4.53 and -5.77 degrees, respectively. These angles are based on typical Scout booster vehicle burnout deviations.

2. The accuracy analysis performed on the -4.53 degree entry angle trajectory produced burnout deviations which are very similar to the deviations used in the impact dispersion study which were derived in an earlier Scout re-entry accuracy analysis for an entry angle of -7.0 (Reference 92).

3. For entry angles in the range investigated the impact range deviations are not symmetrical and the down range or positive range deviation is larger than the up-range or negative range deviation.

D. Reentry Dynamics Study

1. A center of gravity located 0.32 diameters foward of the base is a satisfactory aft limit.

2. Tip-off affects only the initial, low dynamic pressure, flight regime. A 2 lb.-sec. tip-off produces an angle of attack of 3 degrees which damps to zero 160 seconds after burnout.

3. The effects of mass unbalance appear near the roll-pitch resonant point. A 50 oz-in^2 mass unbalance causes a 1.6 degree increase in angle of attack 118 seconds after burnout.

4. A center of gravity located off the axis of symmetry can have a profound effect on the body motions in the low speed flight regime. An off-set of 0.2 in. appears acceptable but a value of 0.3 in. causes very large excursions in angle of attack.

LIST OF REFERENCES

1. Owens, R. V.: Aerodynamic Characteristics of Spherically Blunted Cones at Mach Numbers From 0.5 to 5.0. MSFC-MTP-AERO-61-38, May 1961.

2. Nichols, J. O.: Aerodynamic Characteristics of Blunt Bodies. JPL-TR-32-677, November 1964.

3. Hammer, R. L.: Linear Aerodynamic Loads on Cone-Cylinders at Mach Numbers From 0.7 to 2.0. LMSC/HREC/11289-1, March 1965.

4. Sims, Joseph L.: Tables for Supersonic Flow Around Right Circular Cones at Zero Angle of Attack. NASA SP-3004, 1964.

5. Foster, A. D.: A Compilation of Longitudinal Aerodynamic Characteristics Including Pressure Information for Sharp and Blunt Nose Cones Having Flat and Modified Bases. SC-R-64-1311, January 1965.

6. Sims, Joseph L.: Tables for Supersonic Flow Around Right Circular Cones at Small Angle of Attack. NASA SP-3007, 1964.

7. Murray, Tobak; and Wehrend, W. R.: Stability Derivatives of Cones at Supersonic Speeds. NACA TN 3788, September 1956.

8. Geudtner, W. J., Jr.: Sharp and Blunted Cone Force Coefficients and Centers of Pressure From Wind Tunnel Tests at Mach Numbers from 0.5 to 4.06. CONVAIR Report ZA-7-017, June 1955.

9. Penland, J. A.: A Study of the Stability and Location of the Center of Pressure on Sharp, Right Circular Cones at Hypersonic Speeds. NASA TN D-2283, May 1964.

10. Ward, L. K.; and Urban, R. H.: Dynamic Stability Tests of Three Re-Entry Configurations at Mach 8. AEDC TDR-62-11, January 1962.

11. Smith, D. E.: Computation of the Aerodynamic Characteristics of Arbitrary Bodies at Hypersonic Velocities by the Use of Modified Newtonian Impact Theory - Computer Routine No. LV-VC-26. LTV Astronautics Report No. 00.447, May 1964.

12. Solomon, G. E.: Transonic Flow Past Cone Cylinders. NACA TN 3213, September 1954.

13. Bertram, M. H.: Correlation Graphs for Supersonic Flow Around Right Circular Cones at Zero Yaw in Air as a Perfect Gas. NASA TN D-2339, June 1964.

14. Wehrend, W. R.: A Wind Tunnel Investigation of the Effects of Changes in Base Contour on the Damping-in-Pitch of a Blunted Cone. NASA TN D-2062, November 1963.

15. Wehrend, W. R.; and Reese, David E.: Wind Tunnel Tests of the Static and Dynamic Stability Characteristics of Four Ballistic Re-Entry Bodies. NASA TM X-369, June 1960.

16. Keyes, J. W.: Longitudinal Aerodynamic Characteristics of Blunted Cones at Mach Numbers of 3.5, 4.2 and 6.0. NASA TN D-2201, February 1964.

17. Shaw, D. S.; Fuller, D. E.; and Babb, C. D.: Effects of Nose Bluntness, Fineness Ratio, Cone Angle, and Model Base on the Static Aerodynamic Characteristics of Blunt Bodies at Mach Numbers of 1.57, 1.80, and 2.16 and Angles of Attack up to 180°. NASA TN D-1781, May 1963.

18. Wehrend, William R.: An Experimental Evaluation of Aerodynamic Damping Moments of Cones with Different Centers of Rotation. NASA TN D-1768, March 1963.

19. Van Driest, E. R.: Turbulent Boundary Layer in Compressible Fluids. J. Aeron. Sci., vol. 18, no. 3, March 1951, pp. 145-160.

20. Penland, J. A.: Aerodynamic Force Characteristics of a Series of Lifting Cone and Cone-Cylinder Configurations at a Mach Number of 6.83 and Angles of Attack up to 130°. NASA TN D-840, June 1961.

21. Technical Staff Members: An Empirical Method For The Determination of the Zero-Lift Drag Coefficient of Sharp and Blunt Nosed Conical Exit/Entry Configurations at Subsonic, Transonic, Supersonic and Hypersonic Flight Speeds. Space/Planetary Entry Systems, Inc., Technical Note - 641, August 1964.

22. Whitfield, J. D.; and Wolng, W.: Hypersonic Static Stability of Blunt Slender Cones. AEDC-TDR-62-166, August 1962.

23. Marks, A. S.: Normal Force, Pitching Moment, and Center of Pressure of Several Spherically Blunted Cones at Mach Numbers of 1.50, 2.13, 2.81, and 4.04. AOMC/ARGMA/OML Report 6R8F, April 1958.

24. Merz, G. H.; and Pritts, O. R.: Static Force Tests at Mach 8 of Sharp and Blunt 20-Deg. Half-Angle Cones and a Blunt 70-Deg. Swept Delta Wing. AEDC-TDR-62-187, October 1962.

25. Fisher, L. R.: Equations and Charts for Determining the Hypersonic Stability Derivatives of Combinations of Cone Frustrums Computed by Newtonian Impact Theory. NASA TN D-149, November 1959.

26. Gray, J. Don: Drag and Stability Derivatives of Missile Components According to the Modified Newtonian Theory. AEDC-TN-60-191, November 1960.

27. Shantz, I.: Cone Static Stability Investigation at Mach Numbers 1.56 through 4.24. NAVORD Report 3534, December 1953.

28. Wilkinson, D. B.; and Harrington, S. A.: Hypersonic Force, Pressure, and Heat Transfer Investigations of Sharp and Blunt Slender Cones. AEDC-TDR-63-177, August 1963.

29. Saltzman, E. J.: Base Pressure Coefficients Obtained From the X-15 Airplane for Mach Numbers up to 6. NASA TN D-2420, August 1964.

30. Whitfield, J. D.; and Potter, J. L.: On Base Pressures at High Reynolds Numbers and Hypersonic Mach Numbers. AEDC-TN-60-61, March 1960.

31. Gabeaud, Ingenieru: Base Pressures at Supersonic Velocities. J. Aeron. Sci., vol. 16, no. 7, July 1949, p. 638.

32. Arnold, J. W.: Static Stability and Control Effectiveness Tests on a Maneuvering Re-Entry Vehicle in the Mach Number Range of 0.8 to 4.8. Chance Vought High Speed Wind Tunnel Test 86, December 1962.

33. Love, E. S.: Base Pressure at Supersonic Speeds on Two-Dimensional Airfoils and on Bodies of Revolution With and Without Fins Having Turbulent Boundary Layers. NACA TN 3819, 1957.

34. Brooks, C. W.; and Trescot, C. D.: Transonic Investigation of the Effects of Nose Bluntness, Fineness Ratio, Cone Angle, and Base Shape on the Static Aerodynamic Characteristics of Short, Blunt Cones at Angles of Attack to 180°. NASA TN D-1926, August 1963.

35. Maraca, R. J. : Aerodynamic Load Distributions for the Project FIRE Configurations at Mach Numbers From 0.25 to 4.63. NASA TN D-2604, Feburary 1965.

36. Neal, Luther: Aerodynamic Characteristics at a Mach Number of 6.77 of a 9° Cone Configuration, With and Without Spherical Afterbodies, at Angles of Attack up to 180° With Various Degrees of Nose Blunting. NASA TN D-1606, March 1963.

37. Wolng, William: Blunt Cone Force Tests at M=20. AEDC-TDR-62-43, March 1962.

38. Intrieri, P. F.: Free-Flight Measurements of the Static and Dynamic Stability and Drag of a 10° Blunted Cone at Mach Numbers 3.5 and 8.5. NASA TN D-1299, May 1962.

39. Wells, W. R.; and Armstrong, W. O.: Tables of Aerodynamic Coefficients Obtained From Developed Newtonian Expressions for Complete and Partial Conic And Spheric Bodies at Combined Angles of Attack and Sideslip with Some Comparisons with Hypersonic Experimental Data. NASA TR R-127, 1962.

40. Damstrom, E. J.; and Dye, F. E.: Local Flow Conditions and Aerodynamic Parameters by a Second-Order Shock Expansion Method Applicable to Bodies of Revolution Near Zero Lift and at Supersonic Speeds - LTV Computer Routine No. LV-VC-13. LTV Report No. 00.33, September 1962.

41. Eggers, A. J.: Generalized Shock Expansion Method. J. Aeron. Sci., vol. 22, no. 4, April 1955, pp 231-238.

42. Eggers, A. J.; and Savin, R. C.: A Unified Two-Dimensional Approach To The Calculation of Three-Dimensional Hypersonic Flows, With Application to Bodies of Revolution. NACA Report 1249, 1955 (Supersedes NACA TN 2811)

43. Syvertson, C. A.; and Dennis, D. H.: Second Order Shock Expansion Method Applicable to Bodies of Revolution Near Zero Lift. NACA Report 1328, 1957. (Replaces NACA TN 3527)

44. Eggers, A. J.; and Savin, R. C.: Approximate Methods For Calculating the Flow About Nonlifting Bodies of Revolution at High Supersonic Speeds. NACA TN 2579, 1951.

45. Ward, G. N.: Linearized Theory of Steady High Speed Flow. Cambridge University Press, 1955.

46. Van Dyke, M. D.: A Study of Second-Order Supersonic Flow Theory. NACA TR 1081, 1952. (Supersedes NACA TN 2200)

47. Van Dyke, M. D.: First and Second Order Theory of Supersonic Flow Past Bodies of Revolution. J. Aeron. Sci., vol. 18, no. 3, March 1951, pp 161-173.

48. Van Dyke, M. D.: Practical Calculations of Second-Order Supersonic Flow Past Bodies of Revolution. NACA TN 2744, July 1952.

49. Lighthill, M. J.: Supersonic Flow Past Bodies of Revolution. British ARC R and M no. 2003, 1945.

50. Lees, L: Hypersonic Flow. IAS Preprint No. 554, 1955.

51. Hayes, W. D.; Roberts, R. C.; Haaser, N.: Generalized Linearized Conical Flow. NACA TN 2667.

52. Ferri, A.: The Method of Characteristics for the Determination of Supersonic Flow Over Bodies of Revolution at Small Angles of Attack. NACA Report 1044, 1951.

53. Isenberg, J. S.; and Lin, C. C.: The Method of Characteristics in Compressible Flow, Part I (Steady Supersonic Flow), Air Materiel Command Report, No. F-TR-1173A-ND, December 1947.

54. Kennedy, E. D.: Methods of Calculating the Pressure Distribution on Various Nose Shapes at Zero Angle of Attack in the Range of Mach Numbers From 0.9 to 7.0. Gruen Applied Science Laboratories, Inc., Scientific Report No. 1, 1957.

55. Kennedy, E. D.: Methods of Calculating the Pressure Distribution on Various Nose Shapes at Small Angle of Attack in the Range of Mach Numbers From 0.9 to 7.0. Gruen Applied Science Laboratories, Inc., Scientific Report No. 3, 1957.

56. Cherngi, G. G.: Introduction to Hypersonic Flow. Academic Press, New York, 1961.

57. Shapiro, A. H.: The Dynamics and Thermodynamics of Compressible Fluid Flow, Vols. I and II. The Ronald Press Co., New York, 1954.

58. Hayes, W. D.; and Probstein, R. F.: Hypersonic Flow Theory. Academic Press, New York, 1959.

59. Keuhn, D. M.: Experimental and Theoretical Pressures on Blunt Cylinders for Equilibrium and Nonequilibrium air at Hypersonic Speeds. NASA TN D-1979, November 1963.

60. Jorgensen, L. H.: Aerodynamics of Planetary Entry Configurations in Air and Assumed Martian Atmospheres. AIAA Paper No. 65-318, July 1965.

61. Ellett, D. M.: Pressure Distribution on Sphere Cones. SC-RR-64-1796, January 1965.

62. Amick, J. L.: Pressure Measurements on Sharp and Blunt 5° and 15° Half-Angle Cones at Mach Number 3.86 and Angles of Attack to 100°. NASA TN D-753, February 1961.

63. Van Dyke, M. D.; and Gorden, H. D.: Supersonic Flow About a Family of Blunt Axisymmetric Bodies. NASA TR R-1, 1959.

64. Li, Ting-Li; and Gieger, R. E.: Stagnation Point of a Blunt Body in Hypersonic Flow. IAS Preprint No. 629, 1956.

65. Inouye, Mamoru; and Lomax, Harvard: Comparison of Experimental and Numerical Results for the Flow of a Perfect Gas About Blunt-Nosed Bodies. NASA TN D-1426, September 1962.

66. Gravalos, F. G.; Edelfelt, I. H.; and Emmons, H. W.: The Supersonic Flow About a Blunt Body of Revolution for Gases at Chemical Equilibrium. Proc. IX Int. Astron. Cong., Amsterdam, Vol. I, August 1958, pp. 312-322.

67. Storer, E. M.: A Method for the Prediction of the Pressure Distribution on the Conical Portion of a Sphere-Cone. G. E. Aero. Fund. Memo. No. 131, March 1962.

68. Vaglio-Laurin, Roberto; and Trella, Massimo: A Study of Flow Fields About Some Typical Blunt-Nosed Slender Bodies. PIBAL Report No. 623.

69. Conti, R. J.: Laminar Heat Transfer and Pressure Measurements at a Mach Number of 6 on Sharp and Blunt 15° Half-Angle Cones at Angles of Attack up to 90°. NASA TN D-962, October 1961.

70. Baer, A. L.: Pressure Distributions on a Hemisphere Cylinder at Supersonic and Hypersonic Mach Numbers. AEDC TN-61-96, August 1961.

71. Machell, R. M.; and O'Bryant, W. T.: An Experimental Investigation of the Flow Over Blunt-Nosed Cones at a Mach Number of 5.8. GALCIT Memo No. 32, June 1956.

72. Oliver, R. E.: An Experimental Investigation of Flow Over Simple Blunt Bodies at a Nominal Mach Number of 5.8. GALCIT Memo. No. 26, June 1955.

73. Oliver, R. E.: An Experimental Investigation of Flow About Simple Blunt Bodies at a Nominal Mach Number of 5.8. J. Aeron. Sci., vol. 23, no. 2, February 1956, pp. 177-179.

74. Lewis, C. H.: Pressure Distribution and Shock Shape Over Blunted Slender Cones at Mach Numbers From 16 to 19. AEDC TN-61-81, August 1961.

75. Lomax, Harvard; and Inouye, Mamoru: Numerical Analysis of Flow Properties About Blunt Bodies Moving at Supersonic Speeds in an Equilibrium Gas. NASA TR R-204, July 1964.

76. Capiaux, R.; and Karchmar, L.: Flow Past Slender Blunt Bodies - A Review and Extension. IAS Paper No. 61-210-1904.

77. Munson, A. G.: A Preliminary Investigation of the Flow Over Simple Bodies of Revolution at M=10.4 in Helium. GALCIT Memo. No. 35, December 1956.

78. Julius, Jerome D.: Measurements of Pressure and Local Heat Transfer on a 20° Cone at Angles of Attack up to 20° for a Mach Number of 4.95. NASA TN D-179, December 1959.

79. Bertram, M. H.: Tip Bluntness Effects on Cone Pressures at M=6.85. J. Aeron. Sci., vol. 23, no. 9, September 1956, pp. 898-900.

80. Tewfik, O. K.; and Giedt, W. H.: Heat Transfer, Recovery Factor, and Pressure Distributions Around A Circular Cylinder Normal to a Supersonic Rarefied Air Stream. IAS Paper No. 60-46, January 1960.

81. Tewfik, O. K.: Heat Transfer, Recovery Factor and Pressure Distributions Around A Circular Cylinder Normal to a Supersonic Rarefied Air Stream; Part II - Comparison of Experiment with Theory. University of California TR HE-150-169, May 1959.

82. Lehnert, R.; and Schermerhorn, V. L.: Wake Investigation on Sharp and Blunt Nose Cones at Supersonic Speeds. NAVORD Rep. 5668, January 1958.

83. Kopal, Zdnek: Tables of Supersonic Flow Around Cones of Large Yaw. MIT Tech. Rep. No. 5, 1949.

84. Van Dyke, M. D.; Young, G. B. W.; and Siska, Charles: Proper Use of the MIT Tables for Supersonic Flow Past Inclined Cones. J. Aeron. Sci., vol. 18, no. 5, May 1951, pp. 355-356.

85. Holt, Maurice; and Blackie, John: Experiments on Circular Cones at Yaw in Supersonic Flow. J. Aeron. Sci., vol. 23, no. 10, October 1956, pp. 931-936.

86. Harris, E. L.: Determination of Streamlines on a Sphere-Cone at Angle of Attack From the Measured Surface Pressure Distribution. NAVORD NOL TR 63-37, 1963.

87. Ferri, Antonio: Supersonic Flow Around Circular Cones at Angles of Attack. NACA TR 1045.

88. Ames Research Staff: Equations, Tables, and Charts for Compressible Flow. NACA TR 1135, 1953.

89. Burke, G. L.: Heat Transfer and Pressure Distributions About Sharp and Blunt Elliptic Cones at Angles of Attack and High Mach Numbers. AFFDL TR-64-172, May 1965.

90. Gregorck, G. M.; Nark, T. C.; and Lee, J. D.: An Experimental Investigation of the Surface Pressure and the Laminar Boundary Layer on a Blunt Flat Plate in Hypersonic Flow. ASD-TDR-62-792, March 1963.

91. Bean, J. M.: Statement of Work, Entry Body Aerodynamic Performance Study. LTV Memo 3-50000/5M-265 Rev. A, July 1965.

92. Yanowitch, S.; Kilpatrick, P. D.; and Miller, W. T.: Mission Accuracy Analysis for the Scout Launch Vehicle. LTV Report No. 23.41, November 1962.

93. Everett, H. V.; and Dobson, W. T.: The Near Earth Mission Analysis Trajectory Routine, LV-VC-27. LTV Report No. 00.251, October 1963.

94. Rolfe, B. P.: Nominal, Plus and Minus Three Sigma Motor Performance. LTV DIR No. 23-DIR-89 Rev. B, September 1965.

95. Phillips, William H.: Effect of Steady Rolling on Longitudinal and Directional Stability. NACA TN 1627, June 1948.

TABLE I - Part A

Semi Graphical Summary of the Contents of Data Reports Presenting Experimental Force And Moment Data on Sphere-Cones

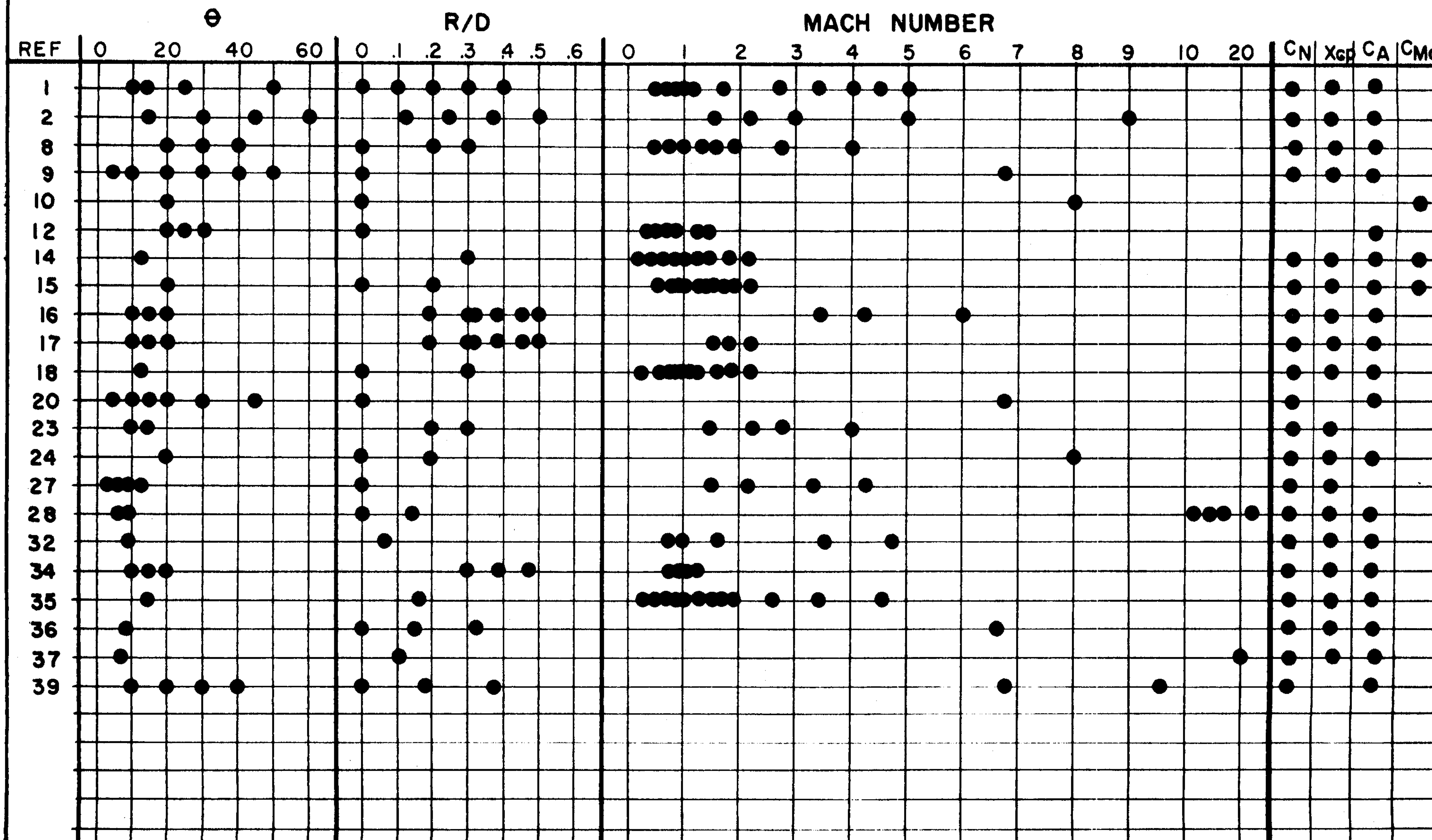

TABLE I - PART B

Summary of Reports Presenting Theoretical Results

The following references include a development of an applicable theory for various types of bodies. A short summary including the theoretical approach, data presented, and limitations of the theory is presented here.

Ref. 3 - An empirical compilation of aerodynamic loads on sharp cones and cone-cylinders in the transonic Mach number range are presented in design chart form.

Ref. 4 - A solution of the Taylor-Maccoll sharp cone equations for cone angles up to 30° and supersonic Mach numbers.

Ref. 5 - This report presents little new information but does compile many reports together for comparison. The range of material covered is very broad.

Ref. 6 - This report presents a solution of the equations derived by A. H. Stone which applies an angle of attack perturbation to the Taylor-Maccoll equations. The range of parameters are the same as in Reference 4. First order solutions for angle of attack dependent variables are presented in derivative form.

Ref. 7 - Closed form solutions for force and moment derivatives for cones in supersonic flow were obtained from an integration of the potential flow equations. First and second order theories are presented.

Ref. 11 - A computer routine for the computation of aerodynamic characteristics of arbitrary bodies using Newtonian impact theory is presented.

Ref. 12 - An approximate solution of the axially symmetric transonic equations, valid for a semi-infinite cone, is presented.

Ref. 13 - The hypersonic similarity parameter is employed to correlate sharp cone solutions for all supersonic Mach numbers and cone angles up to 50°. The sharp cone solutions were obtained from Reference 4 and Reference 6.

Ref. 19 - A numerical solution to the compressible turbulent boundary layer equations are presented for adiabatic and non-adiabatic flat plates.

Ref. 21 - Base pressure drag and forebody drag data are presented for sharp and blunt cones for all Mach numbers. The data were obtained from a correlation of many test results. An accuracy estimate is not included.

Ref. 22 - Similarity parameters correlating normal force and pitching moment coefficients for many sphere-cone configurations are presented. These parameters were derived from Newtonian flow equations, hence are good only for high Mach numbers.

Ref. 25 - Charts for determining aerodynamic coefficients on basic missile components are presented. The coefficients are based on Newtonian flow theory and can be combined for complex missile shapes.

Ref. 26 - This report is similar to Reference 25 except that characteristics for sphere-cones are presented as a complete body.

Ref. 40 - This report develops a computer routine using the second order shock expansion theory of Ref. 43 for use with the LTV 7090 computer. Although the theory is inapplicable for blunt bodies the routine allows computations to begin at an arbitrary point by inputting local conditions from another source. Reasonably accurate results may be obtained by inputting estimated conditions at the sphere-cone junction and adding aerodynamic coefficients for the hemispherical nose.

Other reports, up to Reference 61, not included in either part of this Table contain special information which did not warrant a special discussion but was nevertheless applicable in some degree to the problem.

TABLE II - Part A

Semi Graphical Summary of the Contents of Data Reports Presenting Experimental Pressure Distribution Data on Sphere - Cones

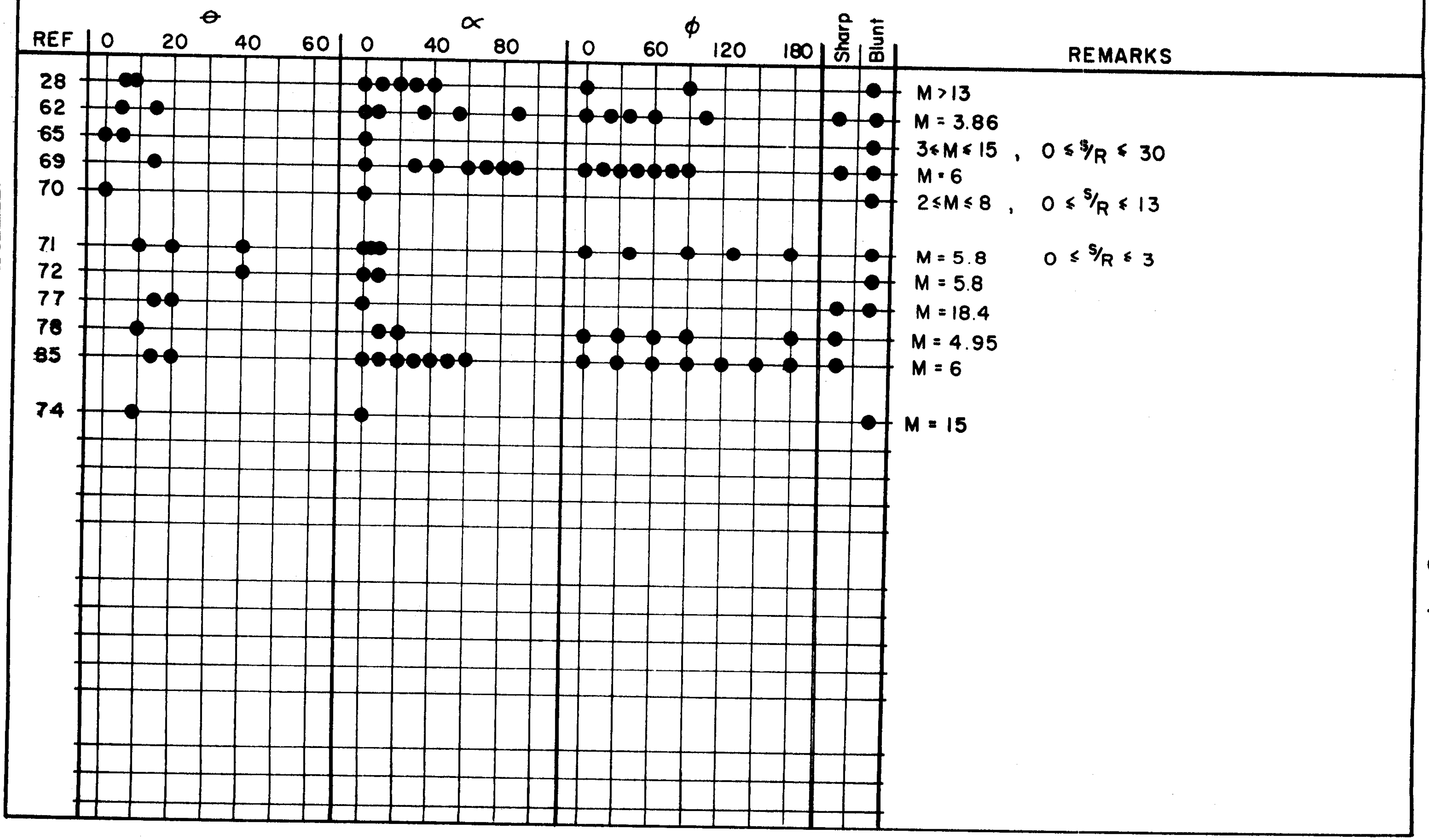

TABLE II - PART B

Summary of Reports Presenting Theoretical Pressure Distribution Data on Sharp and Blunt Cones

The following references include a development and/or results of an applicable theory for predicting pressure distribution on a sharp or blunt cone. A short summary describing the report contents is presented here.

Ref. 61 - Tabulated data for sphere-cones with cone half angles up to 40° are presented for Mach numbers of 3, 4, 6, 10 and infinity.

Ref. 62 - A semi-empirical method of predicting the circumferential pressure distribution on sharp cones is developed.

Ref. 63 - Pressure distribution on a hemisphere is computed for several Mach numbers and specific heats. The method is an "inverse" one wherein a shock shape is assumed and the flow equations are solved for a body shape that yields the assumed shock shape.

Ref. 64 - An approximate solution to the pressure distribution on a hemisphere is presented.

Ref. 66 - A combination of relaxation methods, numerical integration, and method of characteristics are combined to develop a unified theory for computing the flow field about axi-symmetric blunt bodies in supersonic flow.

Ref. 67 - A number of flow field solutions using the method of Reference 68 are presented for sphere-cones. Real gas solutions are correlated using the ratio of specific heats behind a normal shock wave.

Ref. 68 - A method of correlating characteristics solutions for perfect and dissociated gasses is presented for sphere-cones.

Ref. 75 - An "inverse" method is employed to compute flow field solutions about hemispheres in perfect and equilibrium gasses.

Ref. 83 - Higher order terms are retained in Stones' angle of attack pertubation of the Taylor-Maccoll equations so that accurate flow field solutions about a cone at large yaw can be computed.

Ref. 87 - A first-order solution to the circumferential pressure distirbution on a sharp cone at small angles of attack is presented.

Other reports, up to Reference 91, not included in either part of this Table contain special information which did not warrant a special discussion but was nevertheless applicable in some degree to the problem.

TABLE III

Effect of "Three Sigma" Error Sources

Error Source	Fourth Stage Burnout Conditions: Velocity, ft/sec	Altitude, ft.	Flight Path Angle, Degrees	Angle of Attack, Degrees	Impact Range, n. mi.
First Stage motor data; +3σ (Reference 94)	-8	33975	.221	-.21	171
-3σ	1	-35237	-.240	.23	-142
Second Stage motor data; +3σ (Reference 94)	31	18523	.195	-.16	114
-3σ	-32	-18328	-.196	.16	-94
Third Stage motor data; +3σ (Reference 74)	20	4713	.167	-.23	52
-3σ	-20	-4531	-.153	.22	-42
Fourth Stage motor data; +3σ (Reference 74)	144	2108	.012	-.08	18
-3σ	-145	-2109	-.014	.09	-17
Winds; headwind profiles shown in Reference 92	-73	-180	-.075	-.01	-25
tailwind	39	-1979	.020	.01	3
Aerodynamic Drag; +10%	-23	-13836	-.134	.11	-69
-10%	23	13817	.134	-.11	79
Thrust misalignment; .25° pitch up	-35	7105	.017	-.05	21
.25° pitch down	33	-8192	-.028	.06	-26
Guidance system errors; pitch up (Reference 92)	-25	9363	.290	.11	97
pitch down	23	-9305	-.290	-.11	-79
Second Stage deadband; .802° pitch up	-66	21078	.153	-.19	95
.802° pitch down	64	-21225	-.154	.19	-84
Third Stage deadband; .802° pitch up	-13	7016	.260	-.26	83
.802° pitch down	10	-7025	-.260	.26	-69
Fourth Stage tip-off; 1.5° pitch up	-7	2230	.483	1.02	130
1.5° pitch down	2	-2232	-.485	-1.02	-95
RSS of average value	183	49200	.747	1.15	561

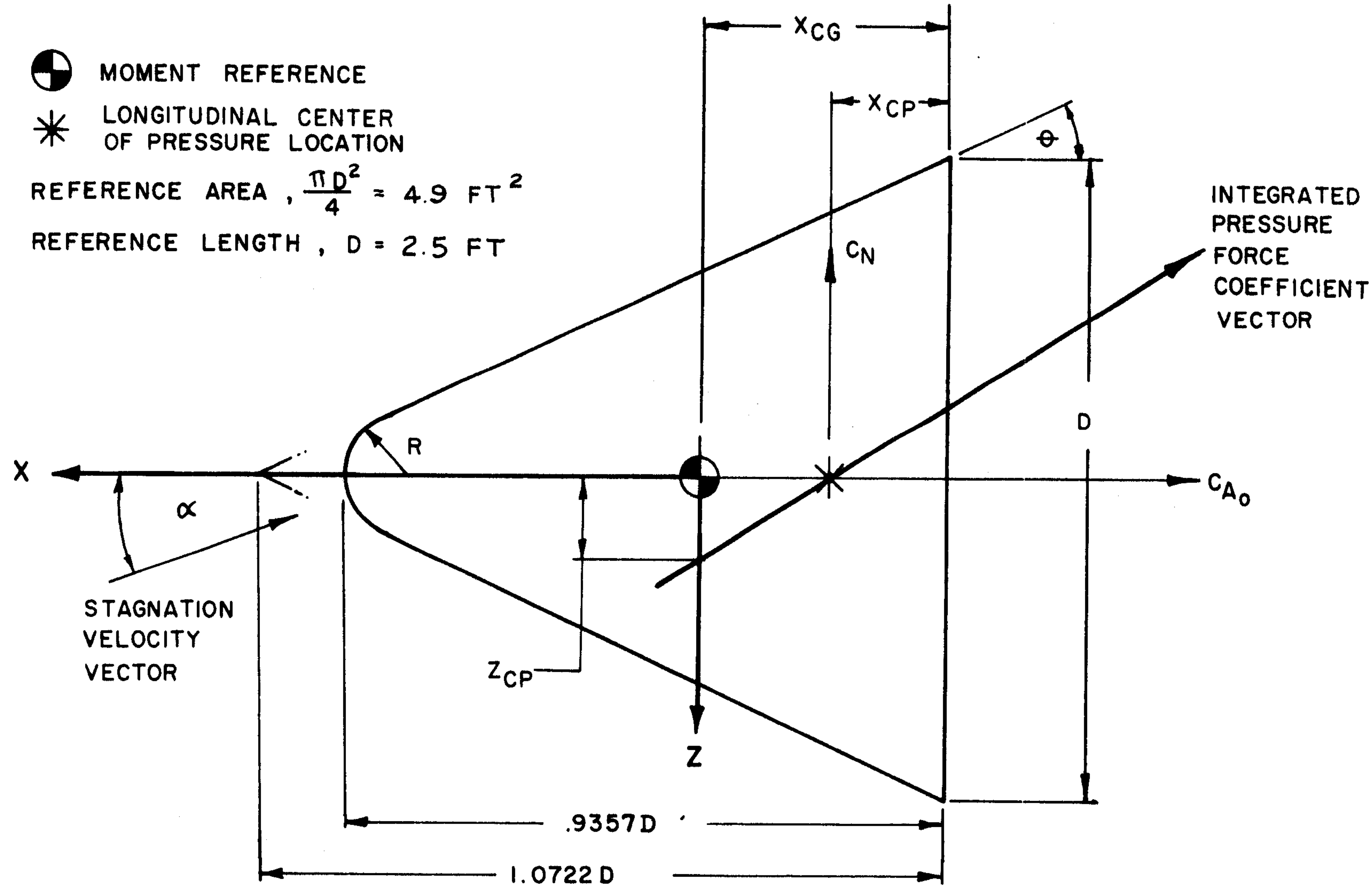

FIGURE 1 - SKETCH OF BASIC SPHERE-CONE BODY , $\Theta = 25°$, R/D = 0.1

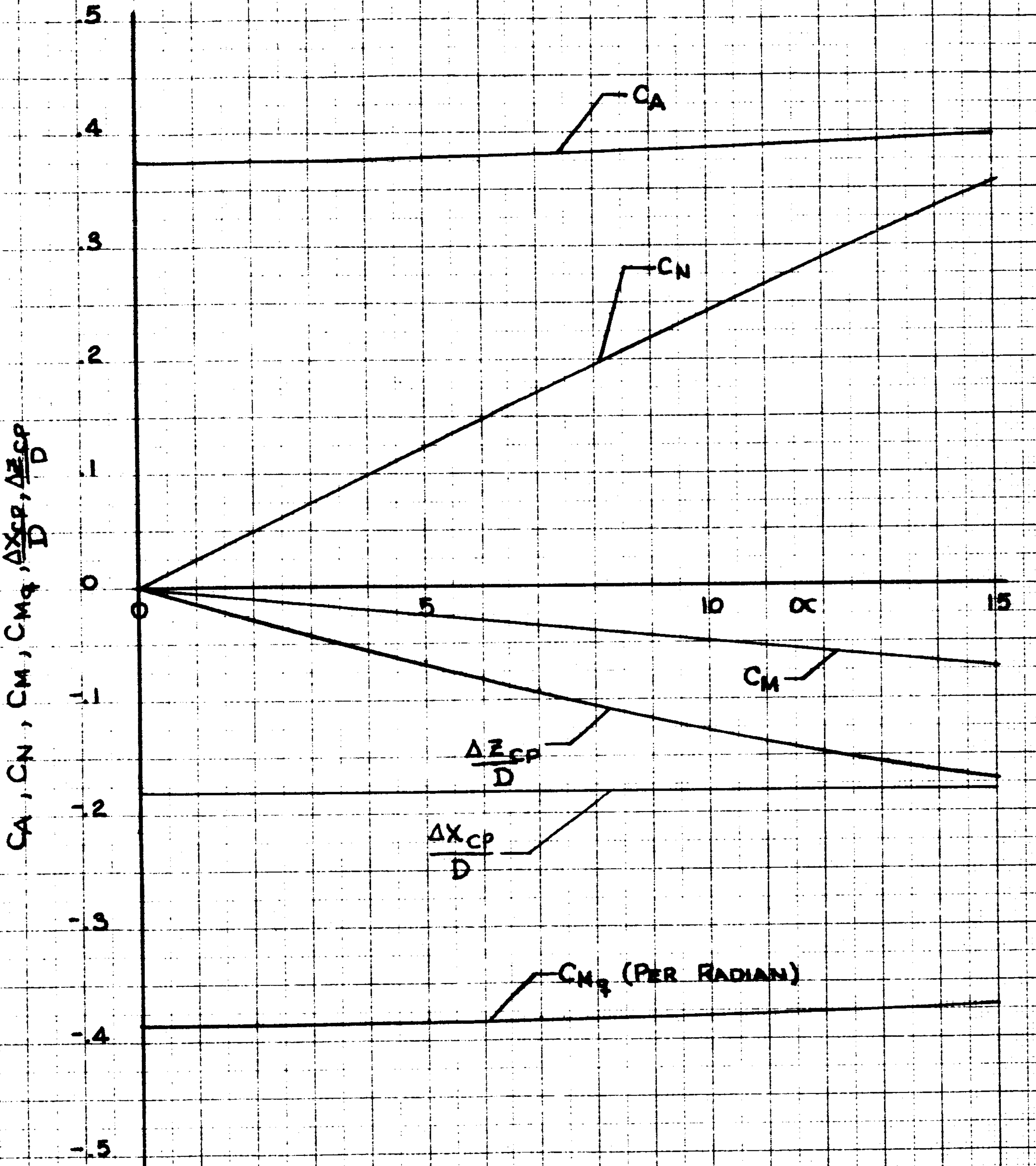

FIGURE 2

MODIFIED NEWTONIAN FLOW COMPUTATION OF AERODYNAMIC PARAMETERS FOR SPHERE-CONE, $\theta = 25°$, $R/D = 0.1$

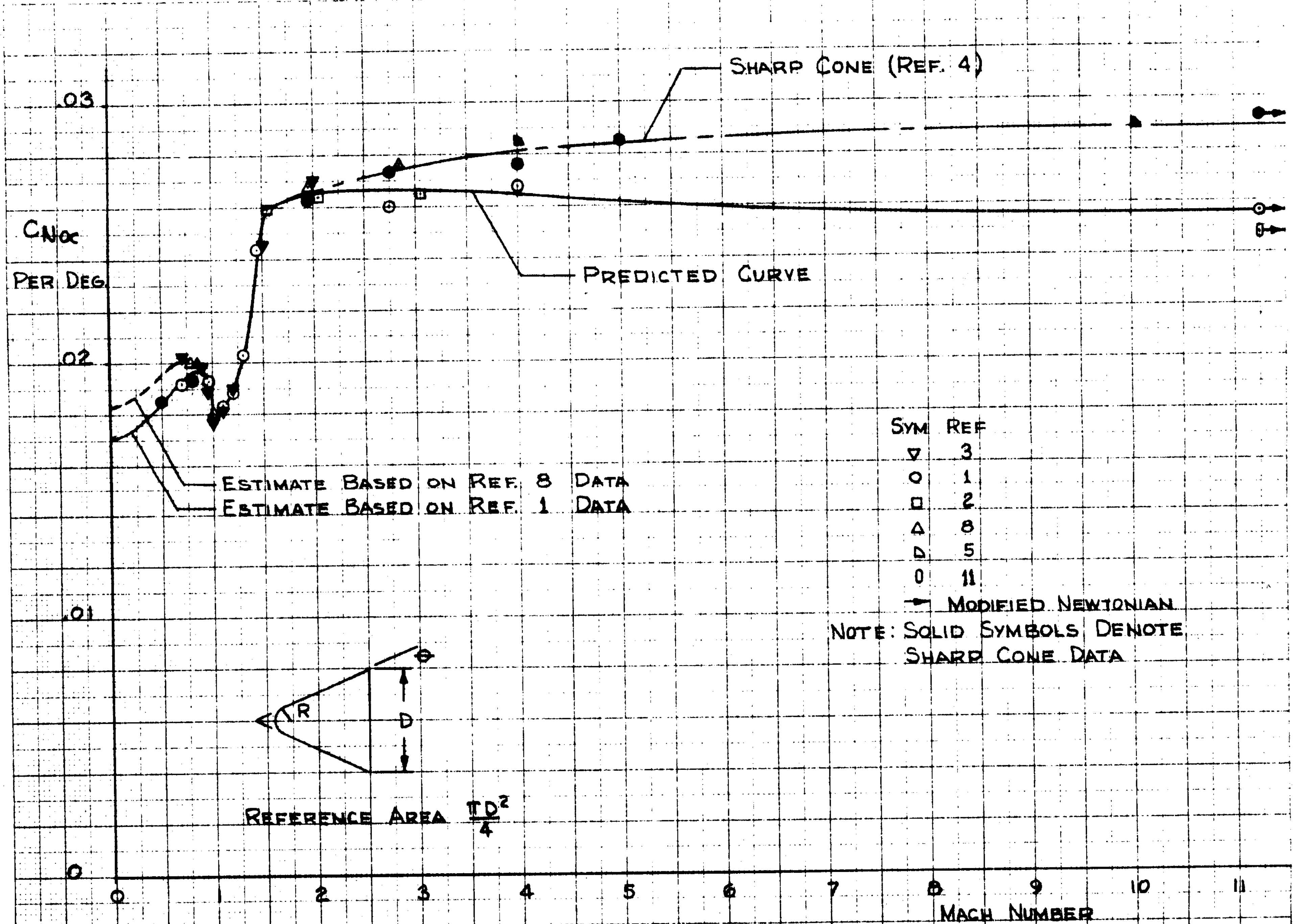

FIGURE 3

VARIATION OF NORMAL FORCE DERIVATIVE WITH MACH NUMBER FOR 25° SPHERE CONE, R/D= 0, 0.1

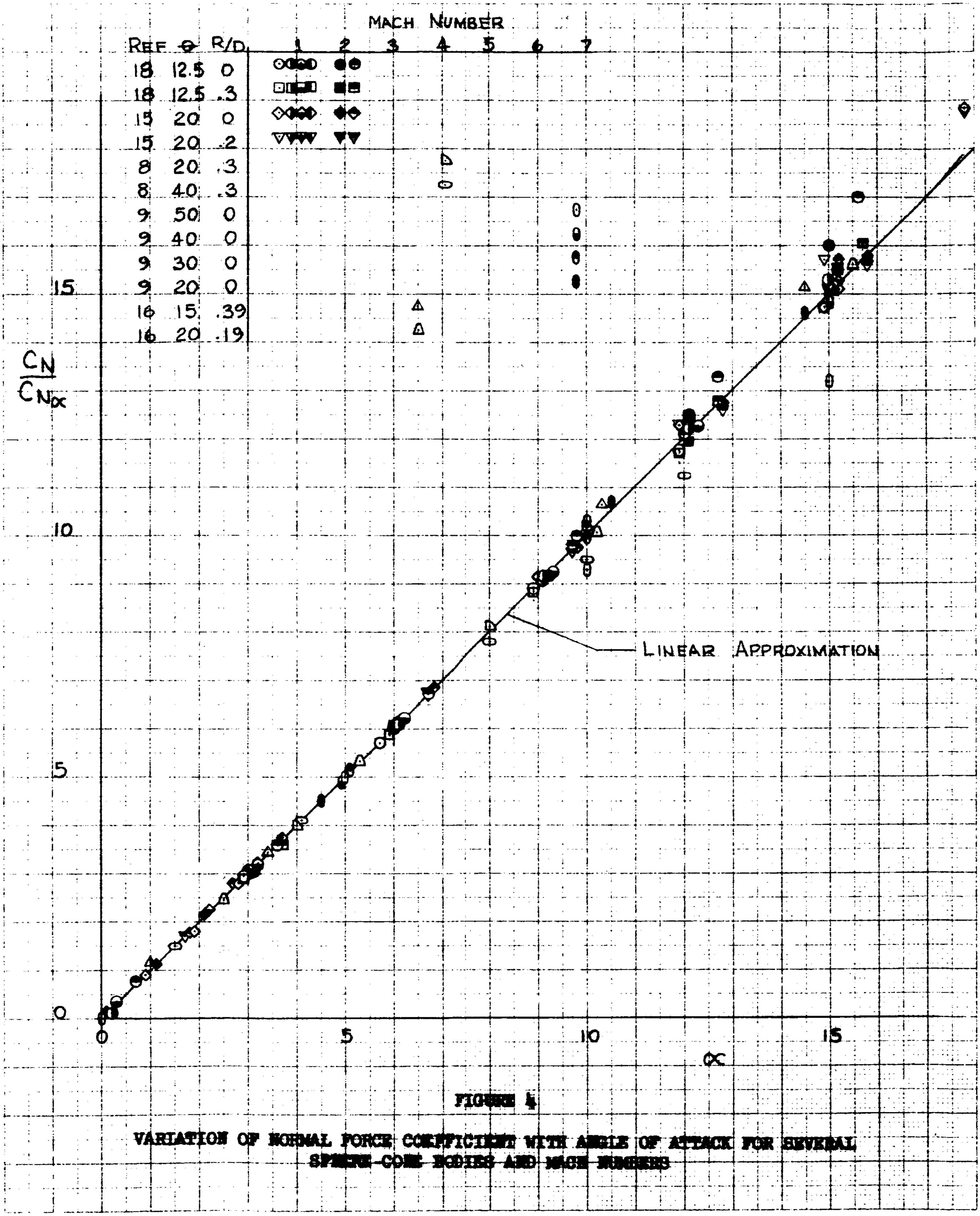

FIGURE 4

VARIATION OF NORMAL FORCE COEFFICIENT WITH ANGLE OF ATTACK FOR SEVERAL SPHERE-CONE BODIES AND MACH NUMBERS

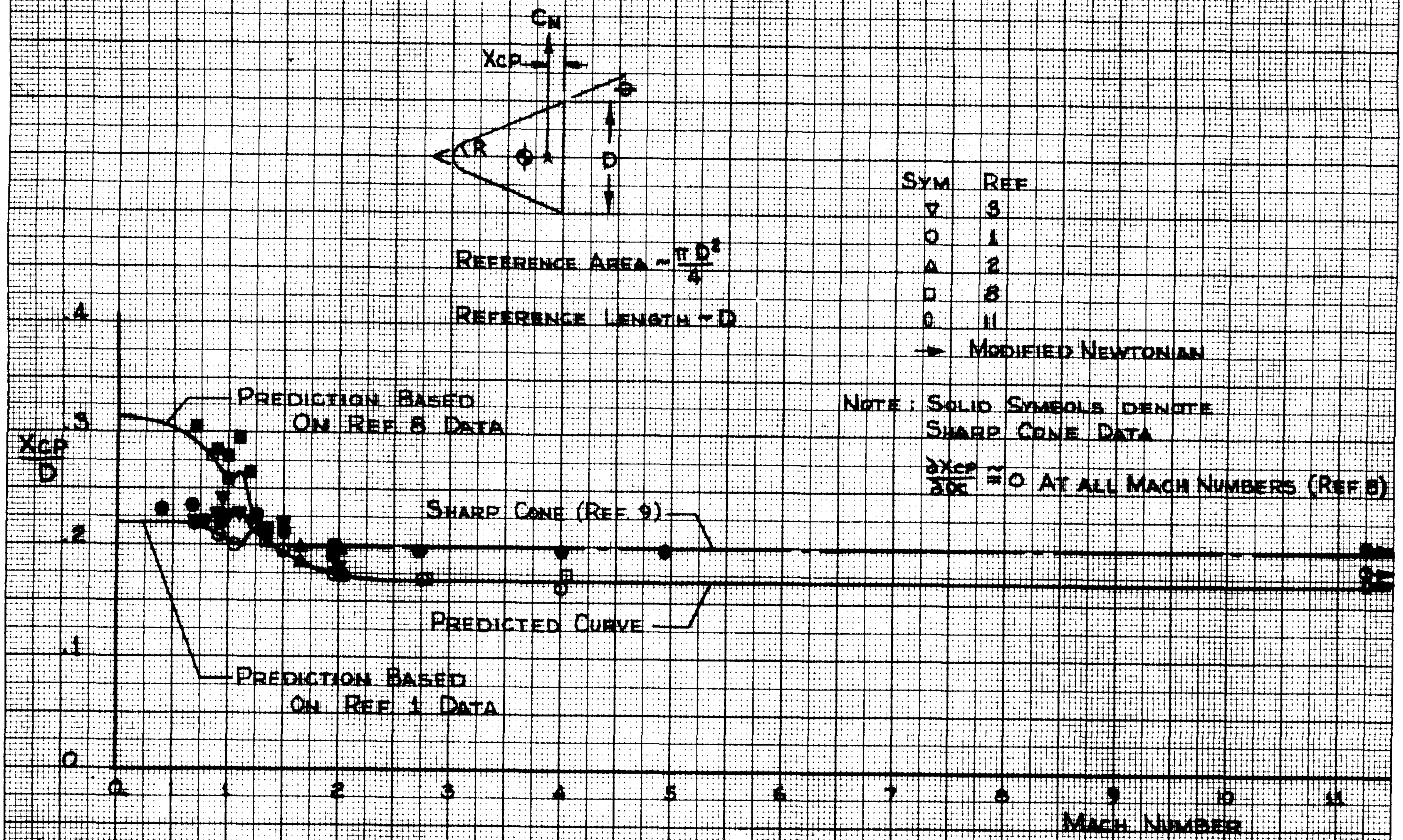

FIGURE 5

VARIATION OF CENTER OF PRESSURE LOCATION WITH MACH NUMBER FOR SPHERE-CONES, $\theta = 25°$, $\frac{R}{D} = 0, 0.1$

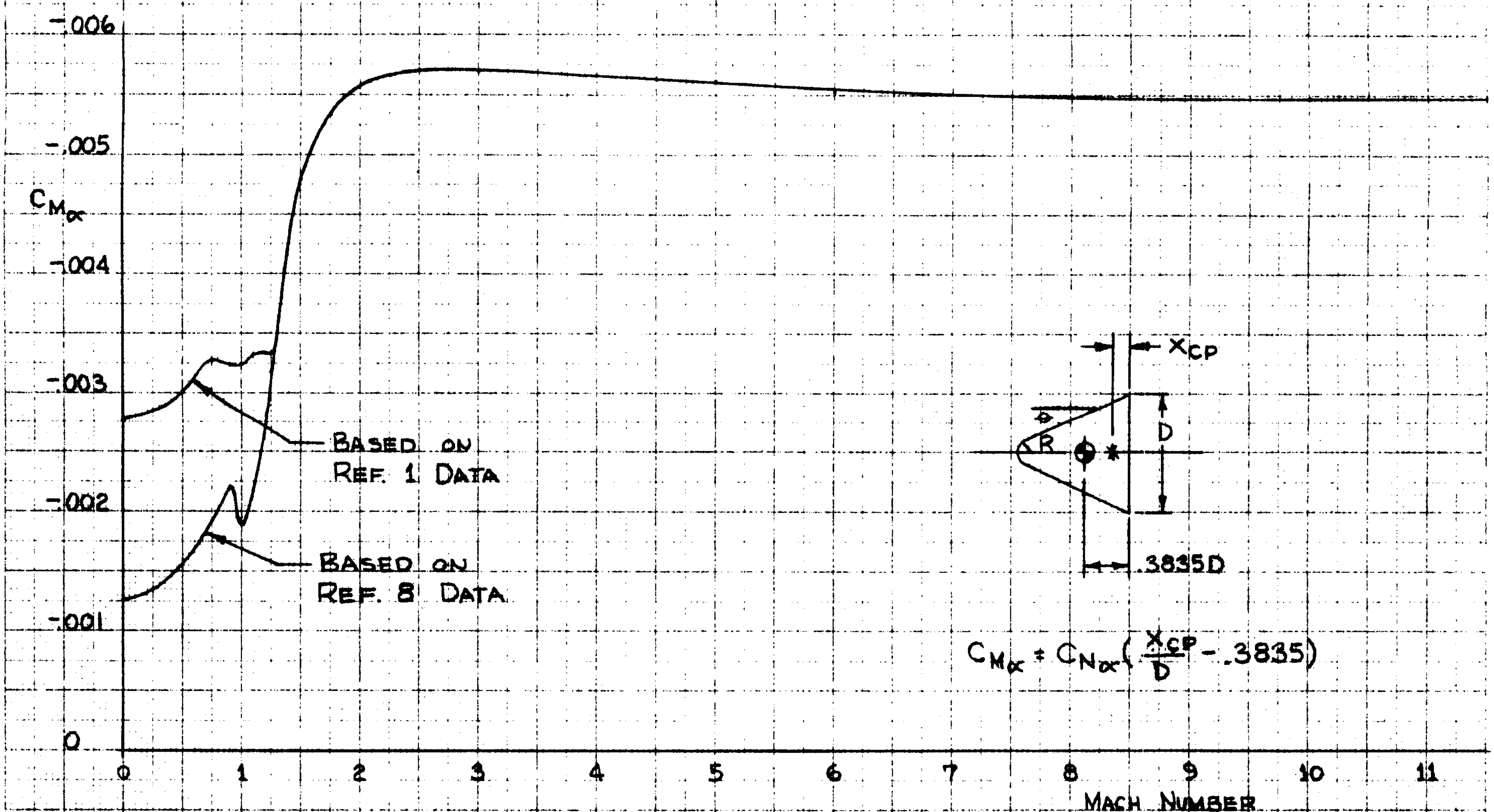

FIGURE 6

PREDICTION OF PITCHING MOMENT COEFFICIENT DERIVATIVE VARIATION WITH MACH NUMBER FOR SPHERE CONE, $\theta = 25°$, $R/D = 0.1$

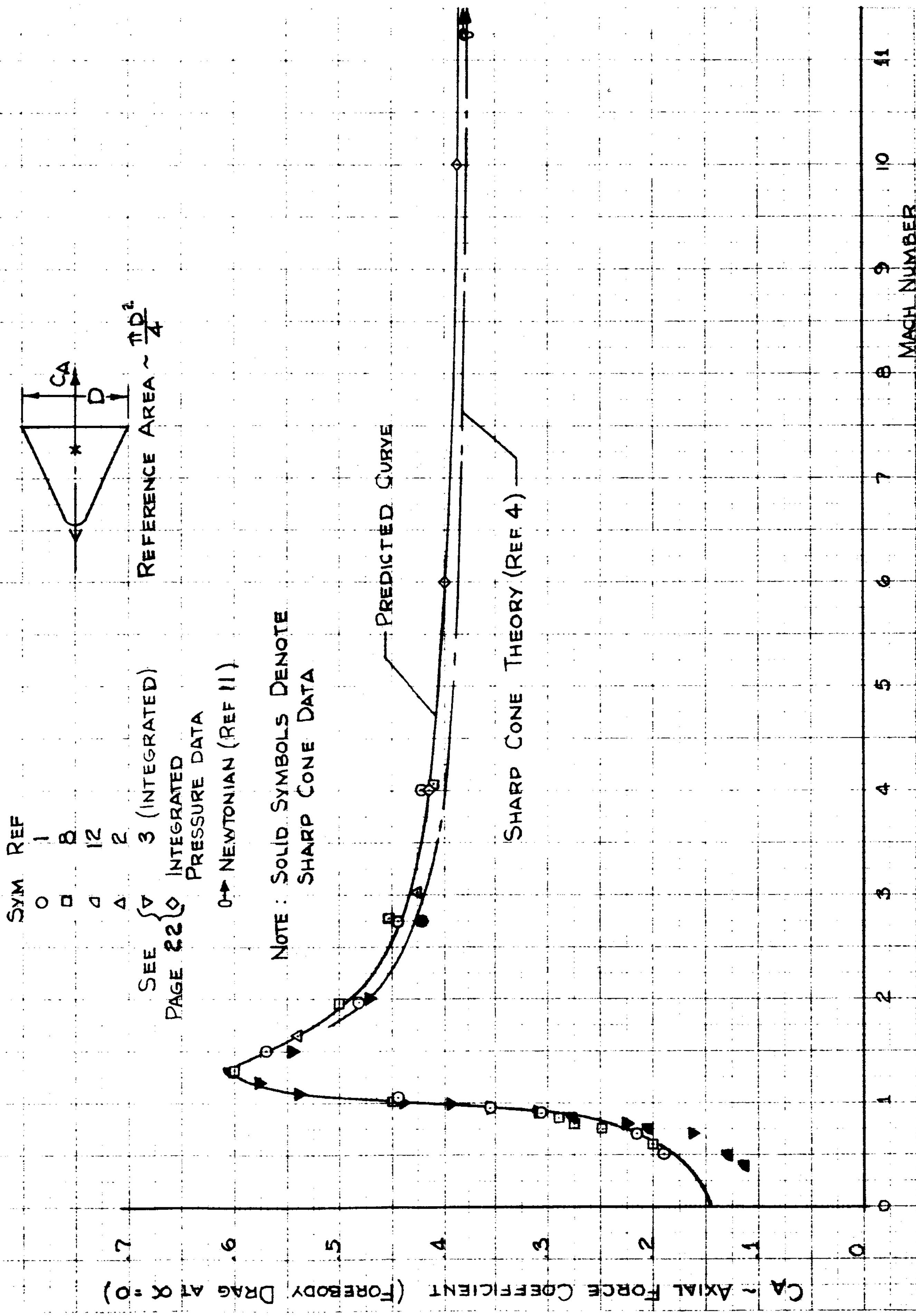

FIGURE 7

VARIATION OF AXIAL FORCE COEFFICIENT WITH MACH NUMBER FOR 25° SPHERE-CONE, R/D = 0.1

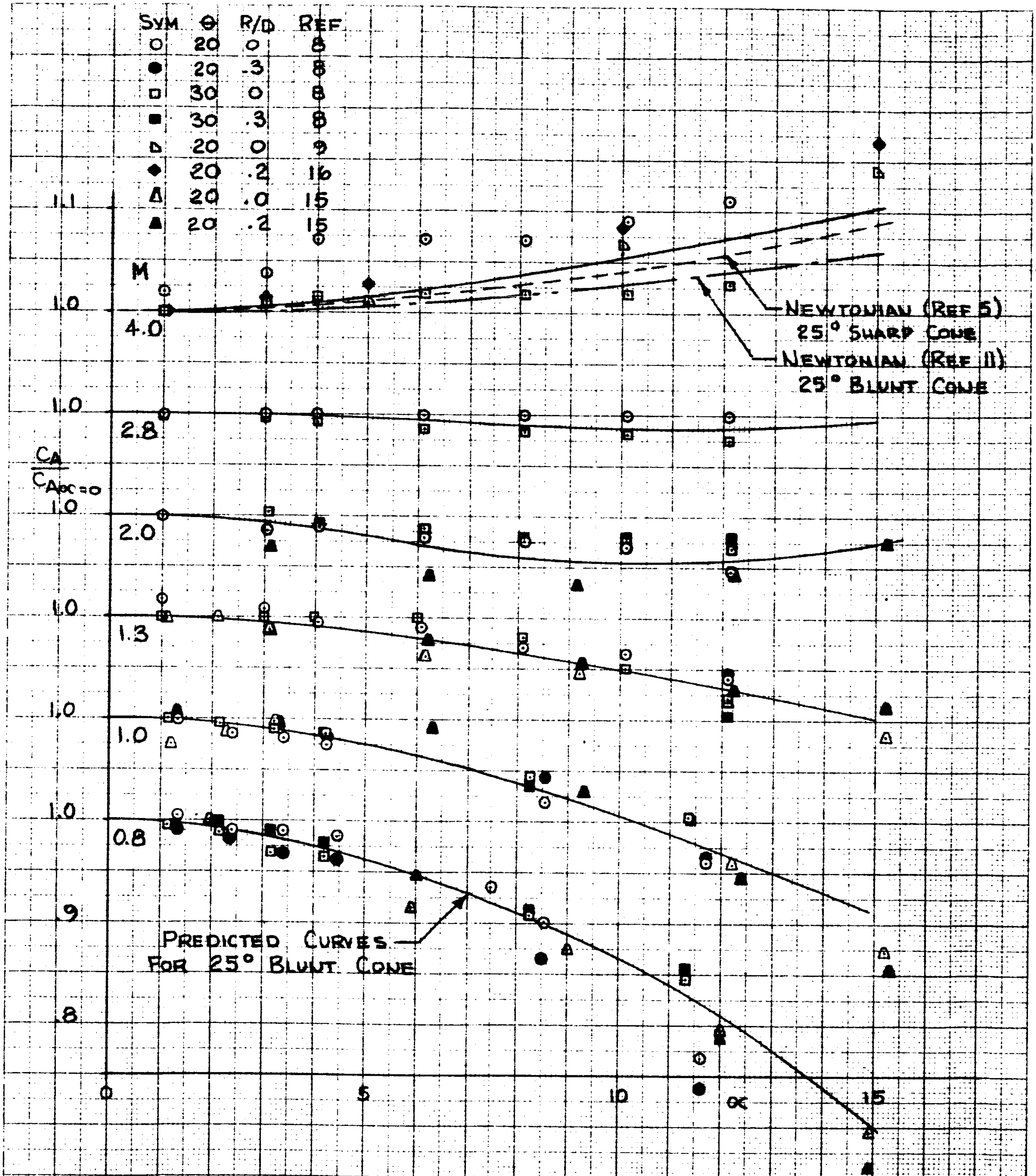

FIGURE [illegible]

VARIATION OF AXIAL FORCE COEFFICIENT WITH ANGLE OF ATTACK AND MACH NUMBER

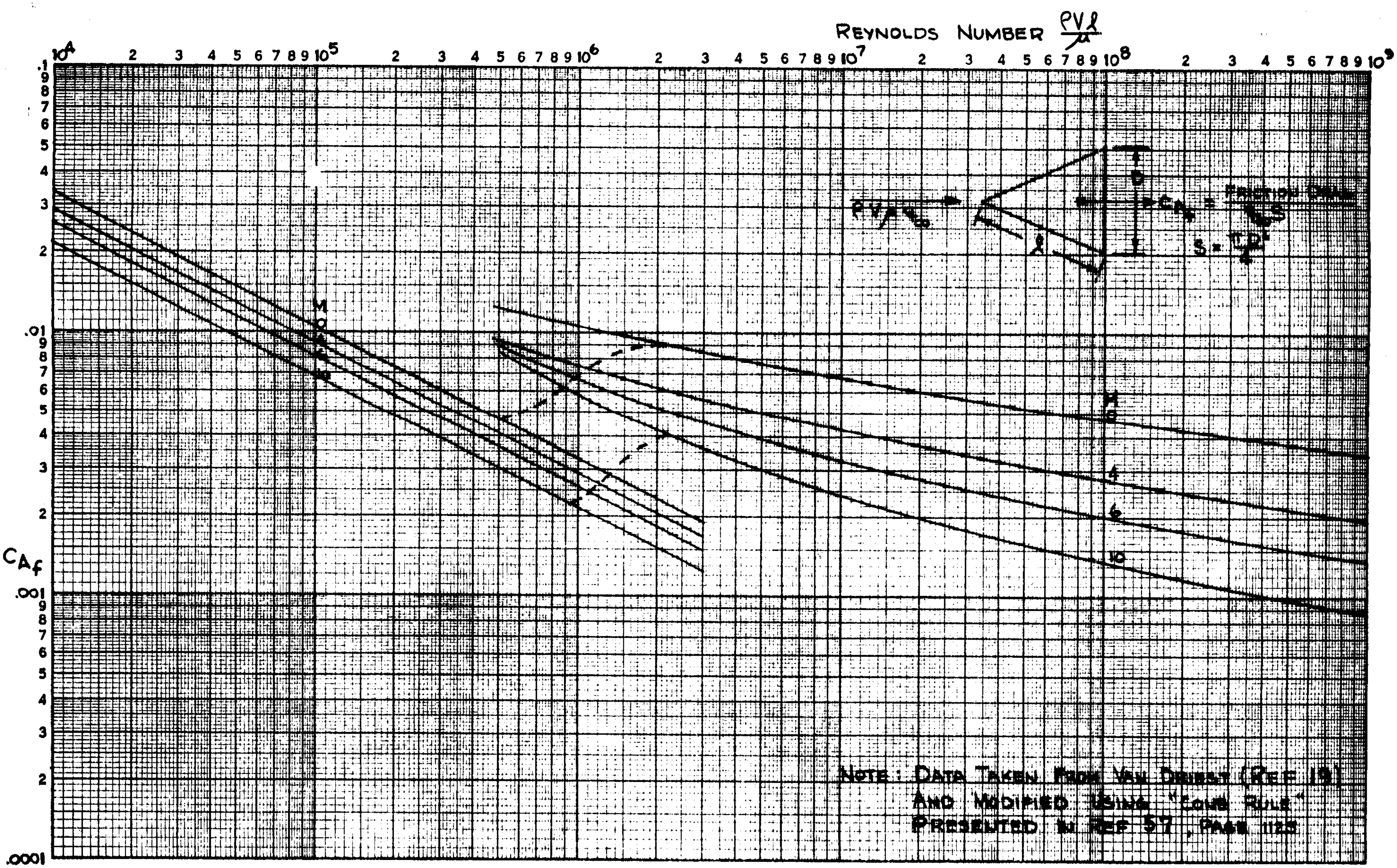

FIGURE 9

INTEGRATED SKIN FRICTION DRAG COEFFICIENT ON A 25° ADIABATIC CONE AS A FUNCTION OF REYNOLDS NUMBER AND MACH NUMBER

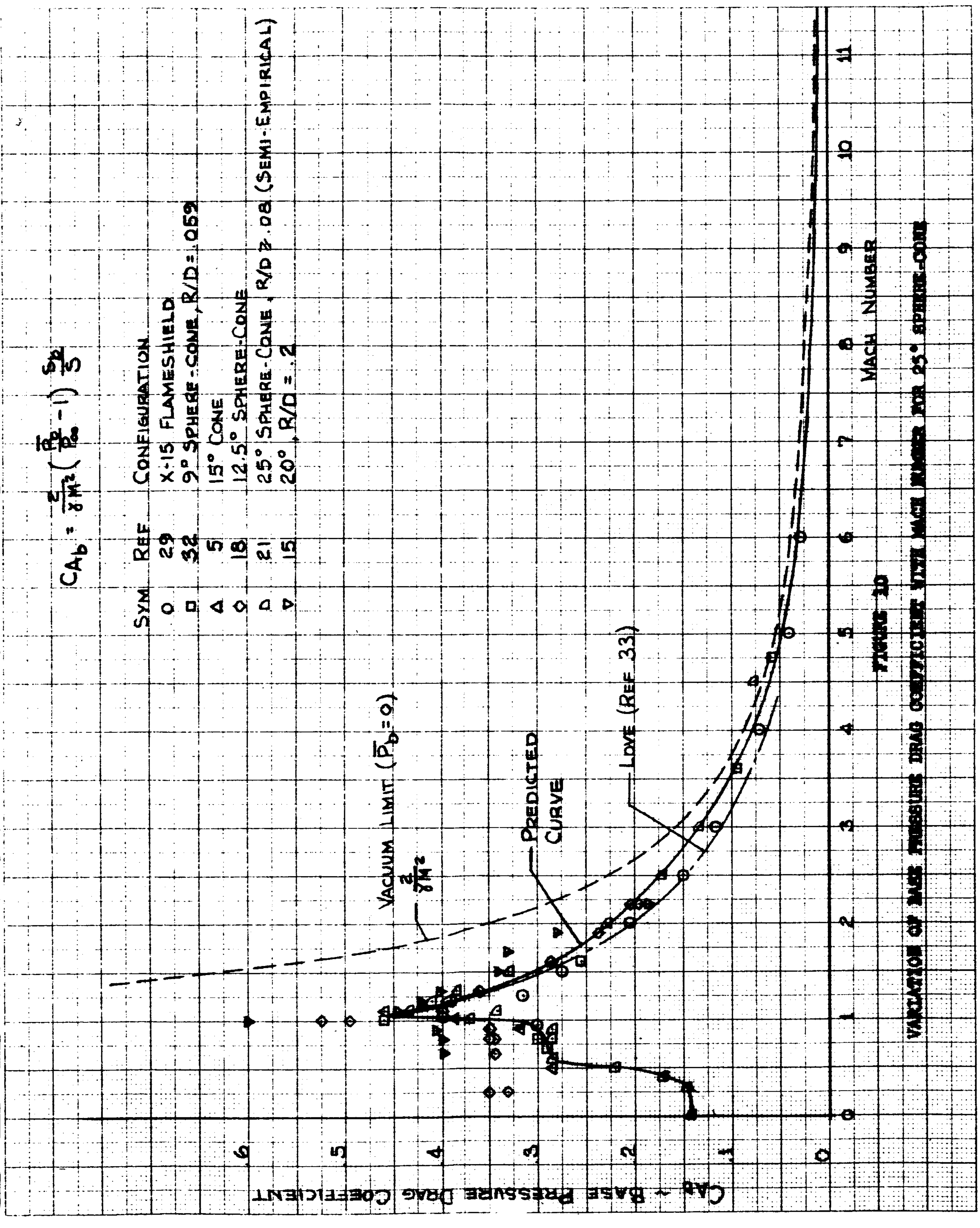

FIGURE 10

VARIATION OF BASE PRESSURE DRAG COEFFICIENT WITH MACH NUMBER FOR 25° SPHERE-CONE

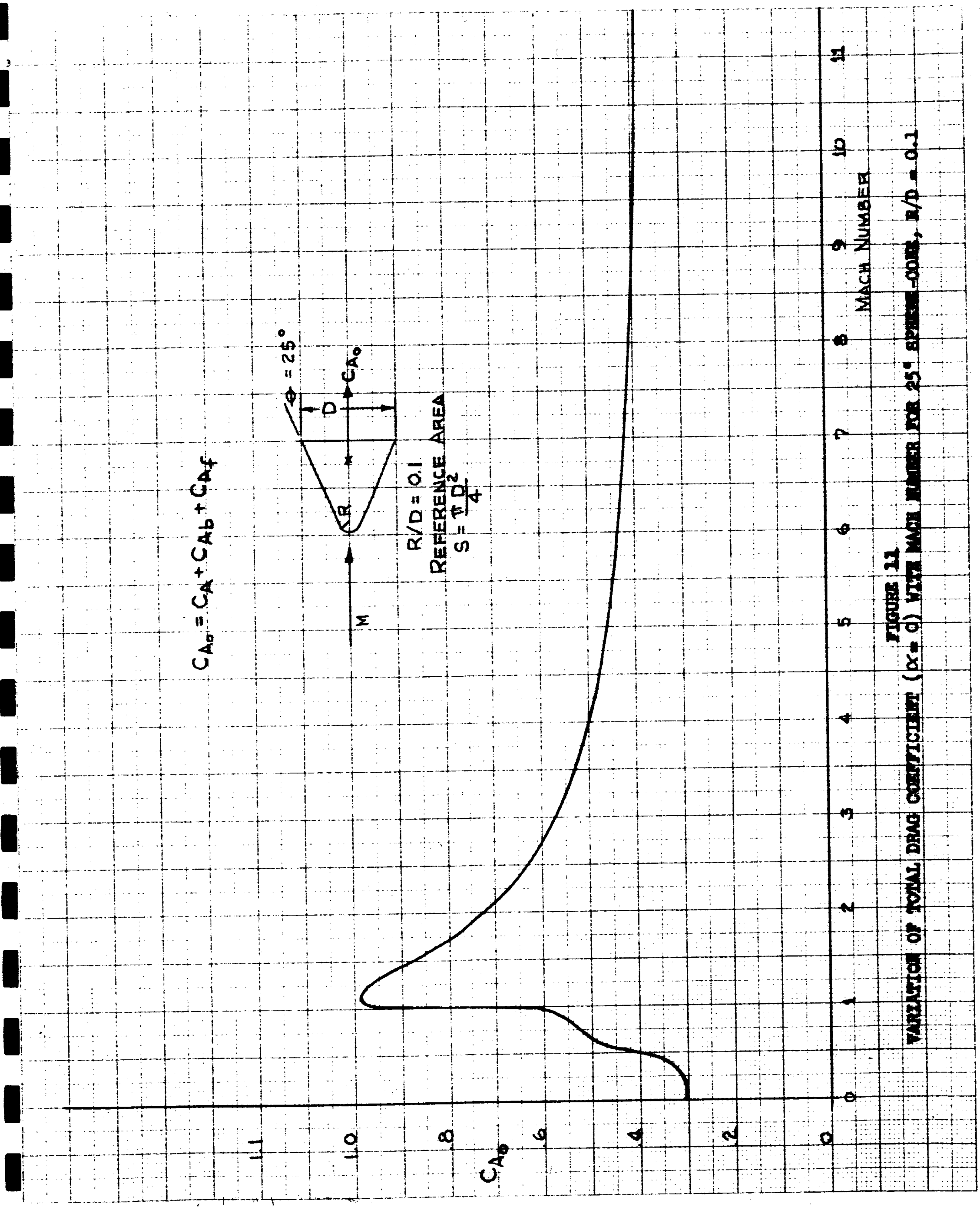

FIGURE 11
VARIATION OF TOTAL DRAG COEFFICIENT ($\alpha = 0$) WITH MACH NUMBER FOR 25° SPHERE-CONE, R/D = 0.1

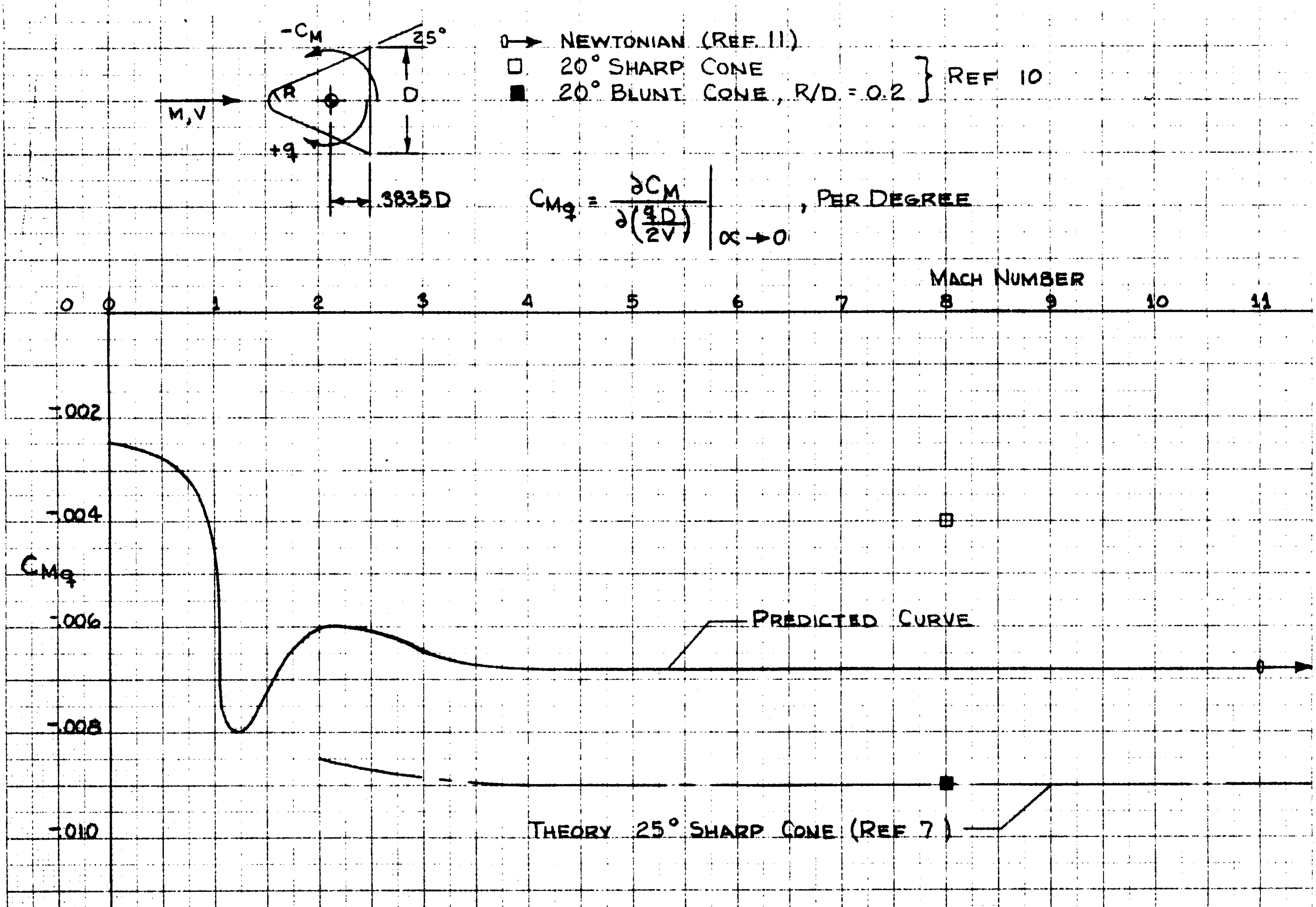

FIGURE 12

VARIATION OF PITCH DAMPING DERIVATIVE WITH MACH NUMBER FOR 25° SPHERE-CONE, R/D = 0.1

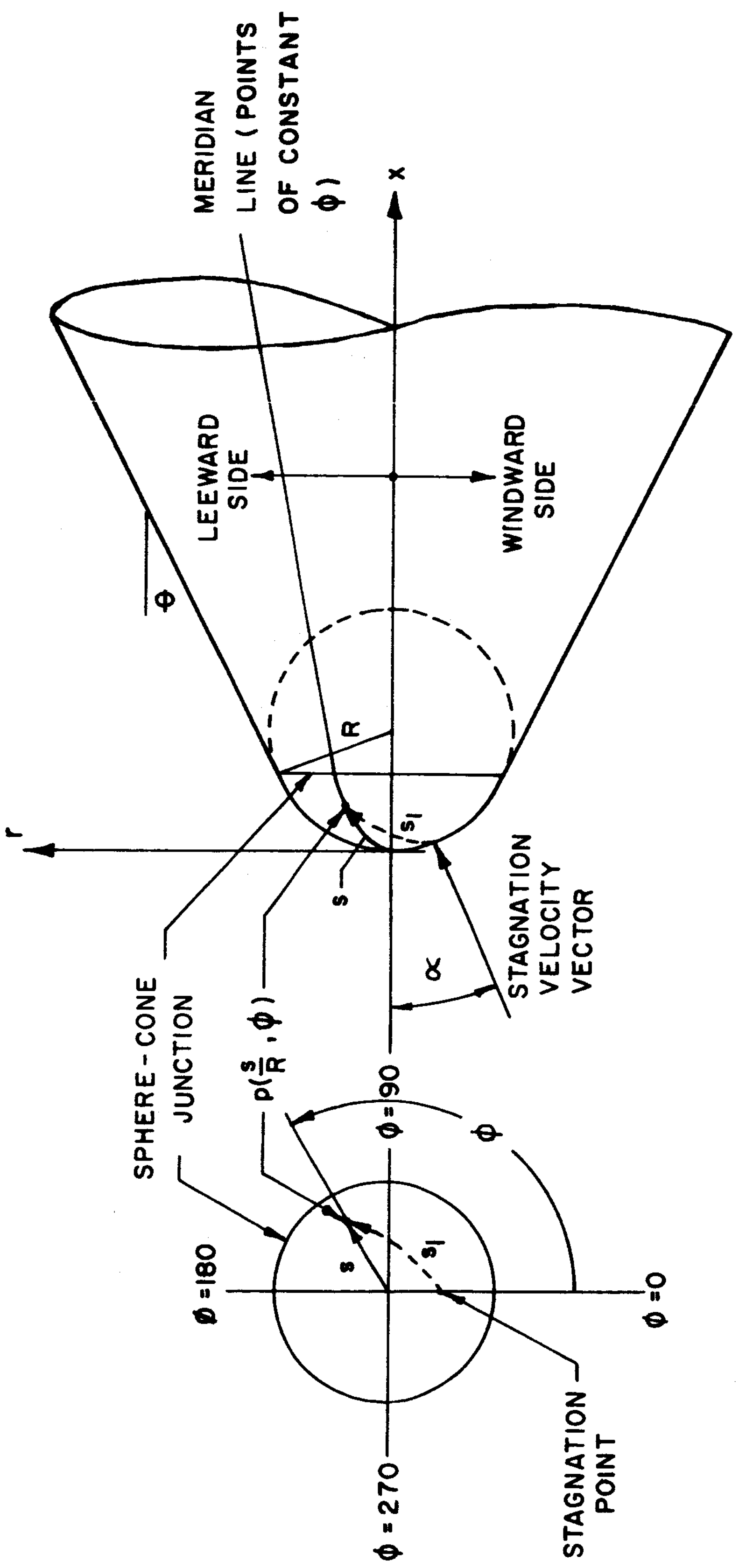

FIGURE 13 - IDENTIFICATION OF NOMENCLATURE USED WITH PRESSURE DISTRIBUTION DATA ON SPHERE-CONE BODIES

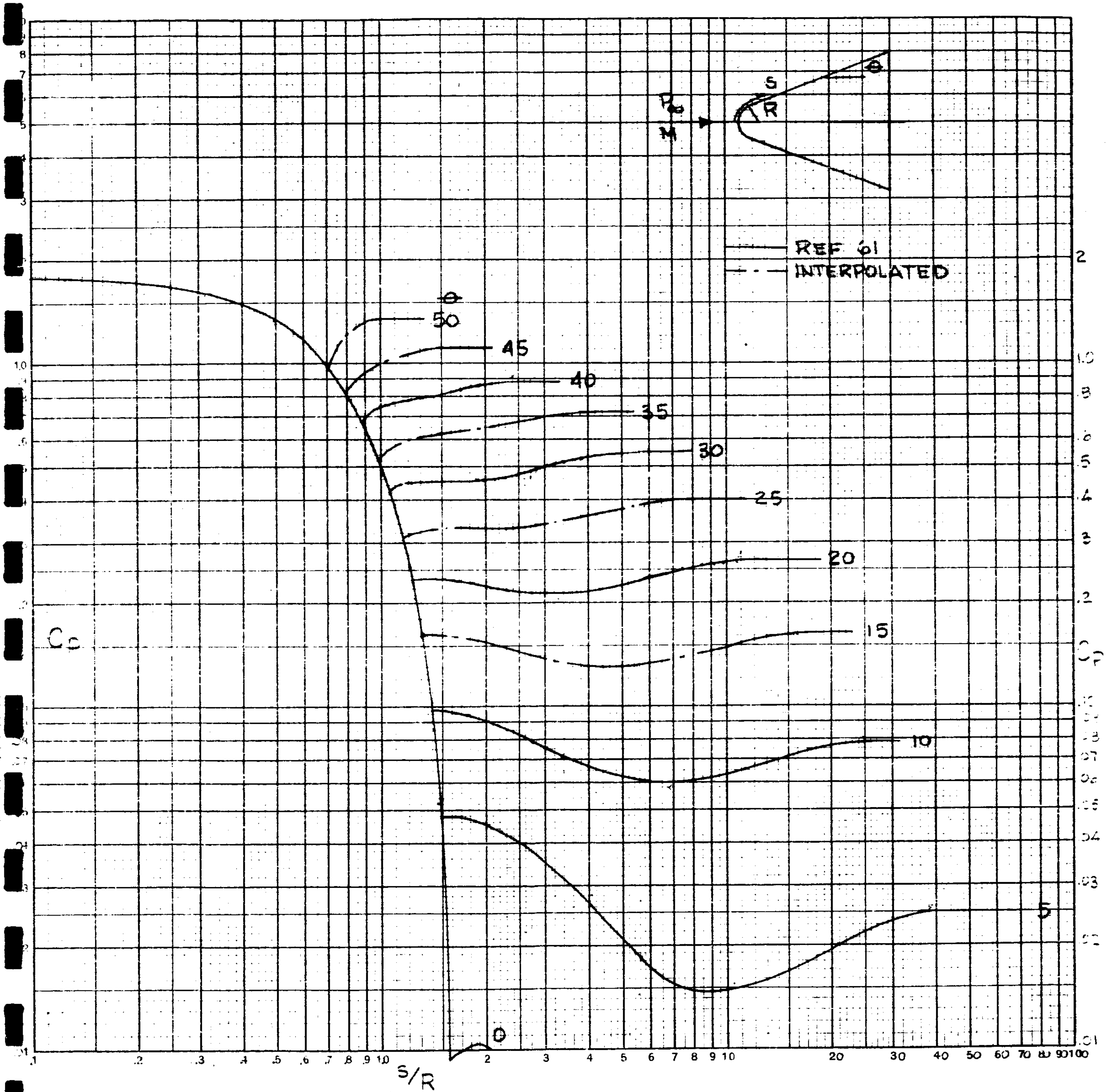

FIGURE 14

VARIATION OF SURFACE PRESSURE COEFFICIENT ON SPHERE-CONES FOR VARIOUS CONE ANGLES AT M = 4

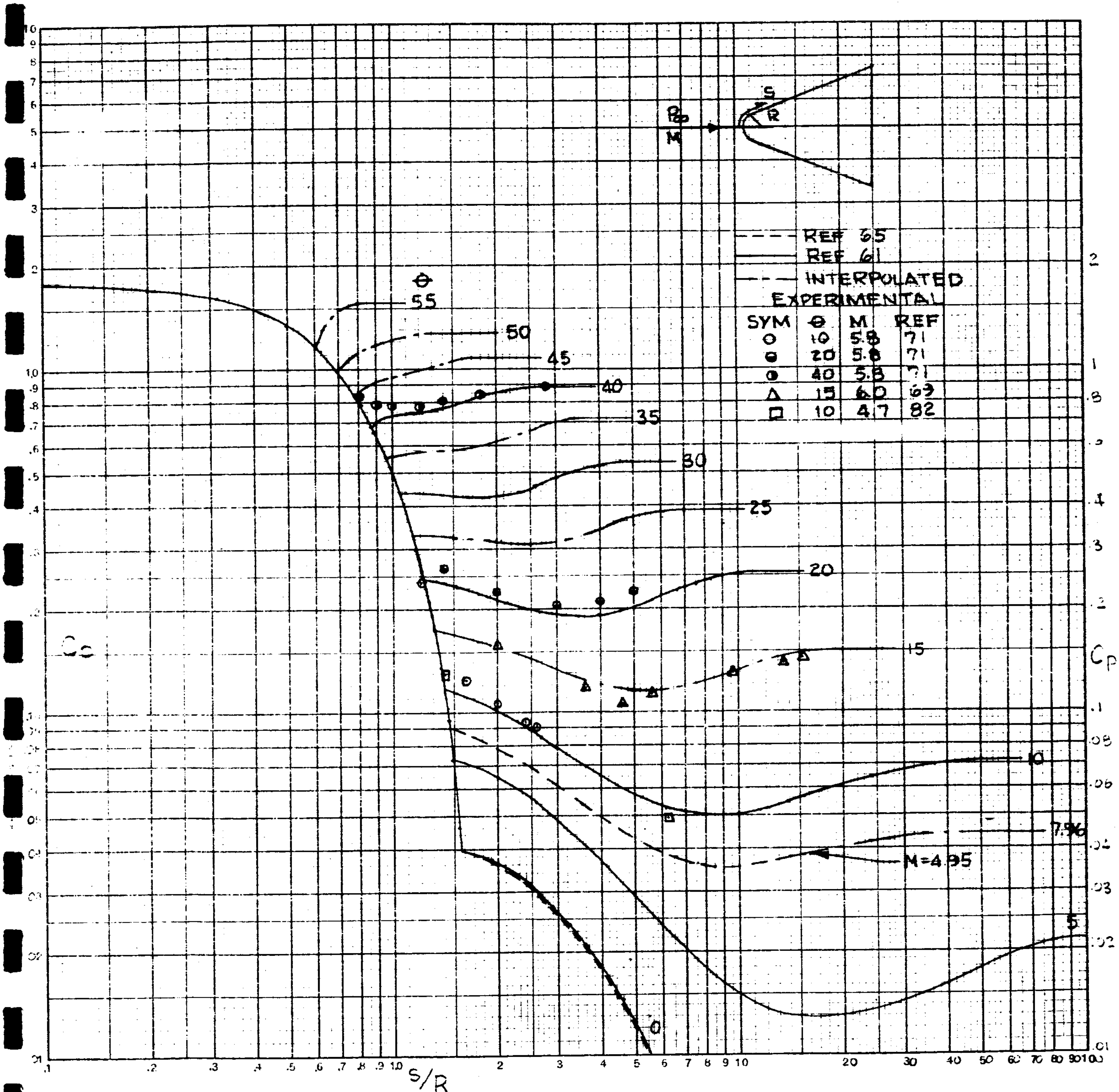

FIGURE 15

VARIATION OF SURFACE PRESSURE COEFFICIENT ON SPHERE-CONES FOR VARIOUS CONE ANGLES AT M = 6

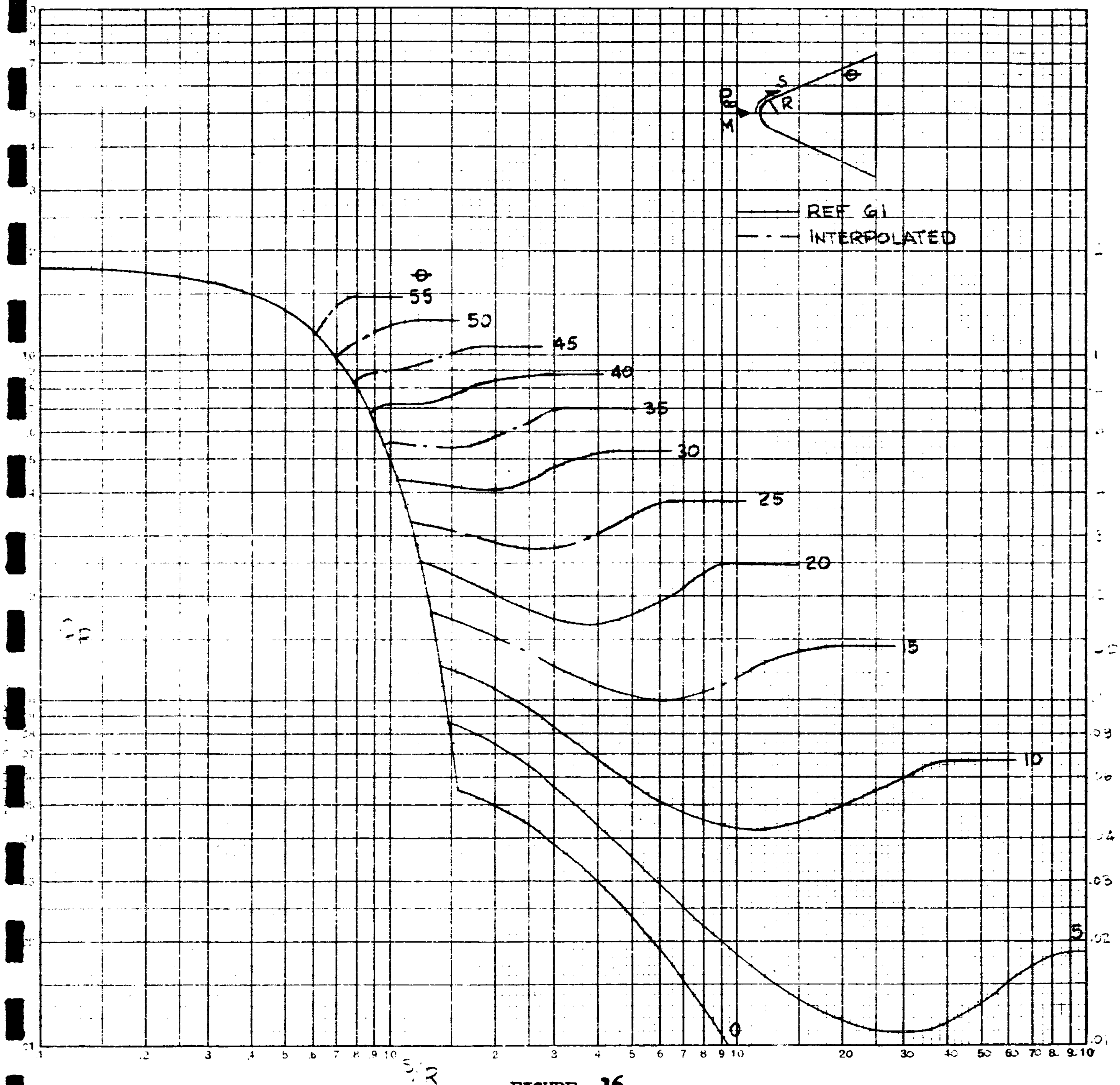

FIGURE 16

VARIATION OF SURFACE PRESSURE COEFFICIENT ON SPHERE-CONES FOR VARIOUS CONE ANGLES AT M = 10

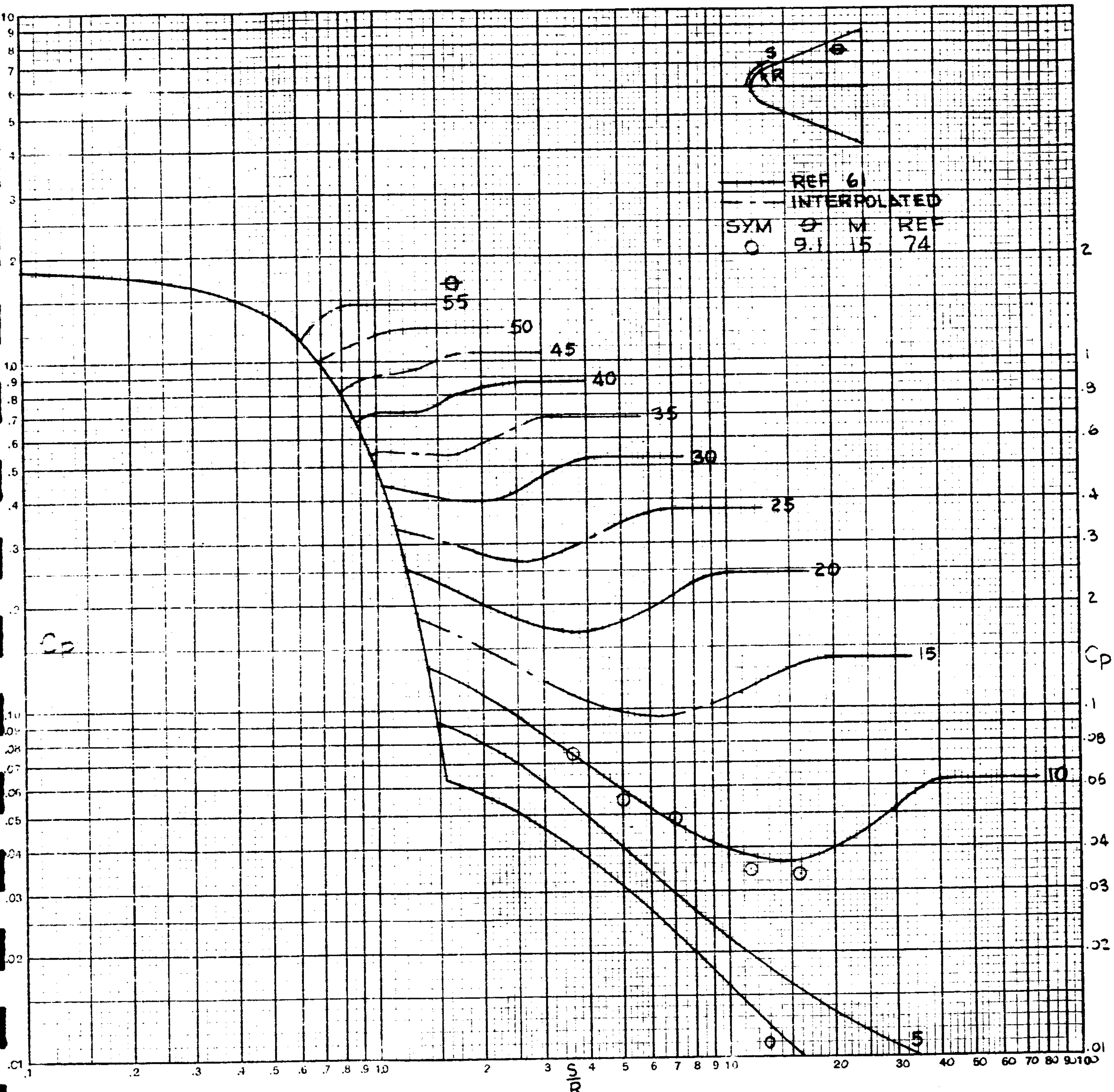

FIGURE 17

VARIATION OF SURFACE PRESSURE COEFFICIENT ON SPHERE-CONES FOR VARIOUS CONE ANGLES AT M ≥ 15

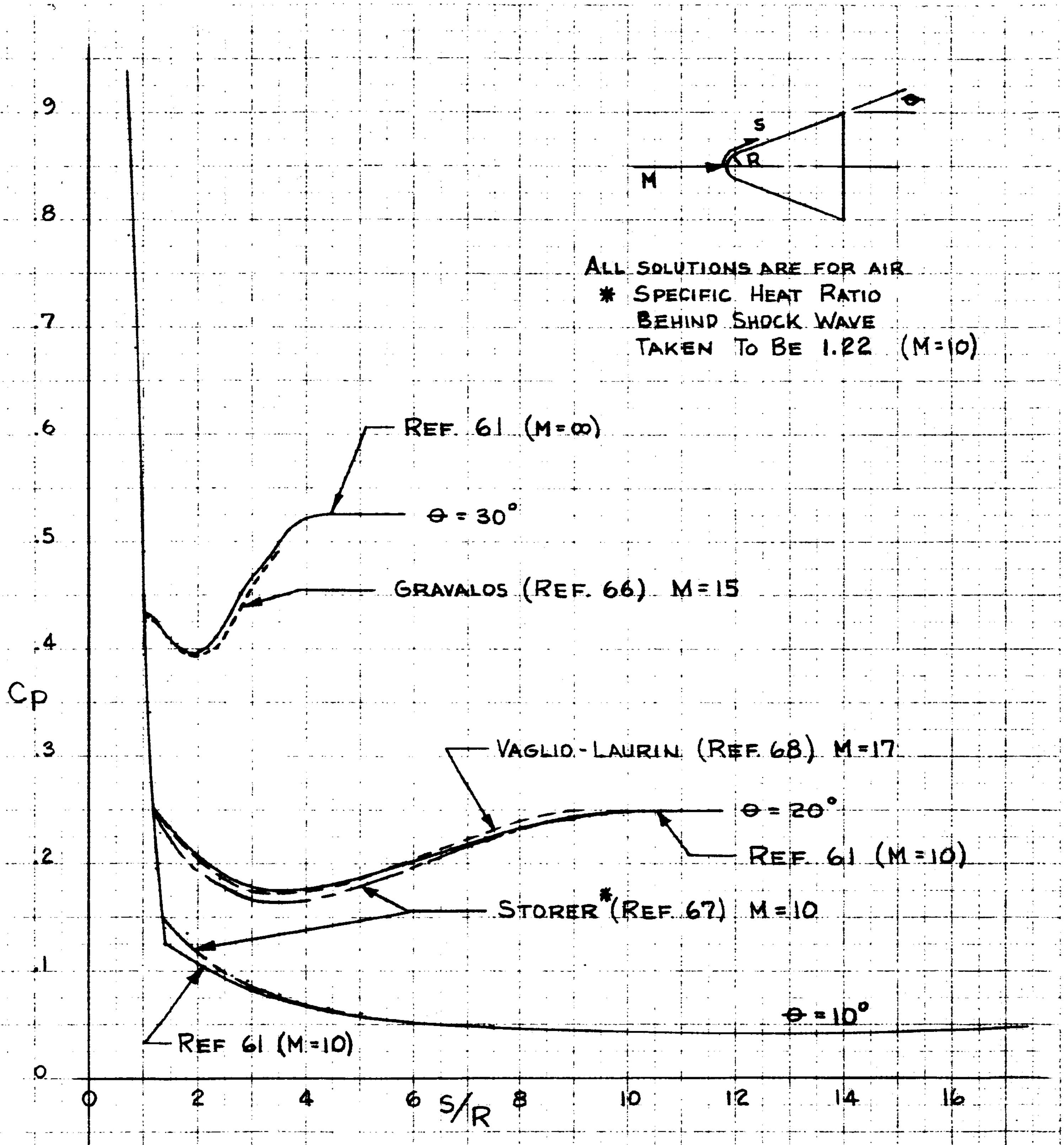

FIGURE 18

COMPARISON OF NUMERICAL SOLUTIONS FROM SEVERAL SOURCES

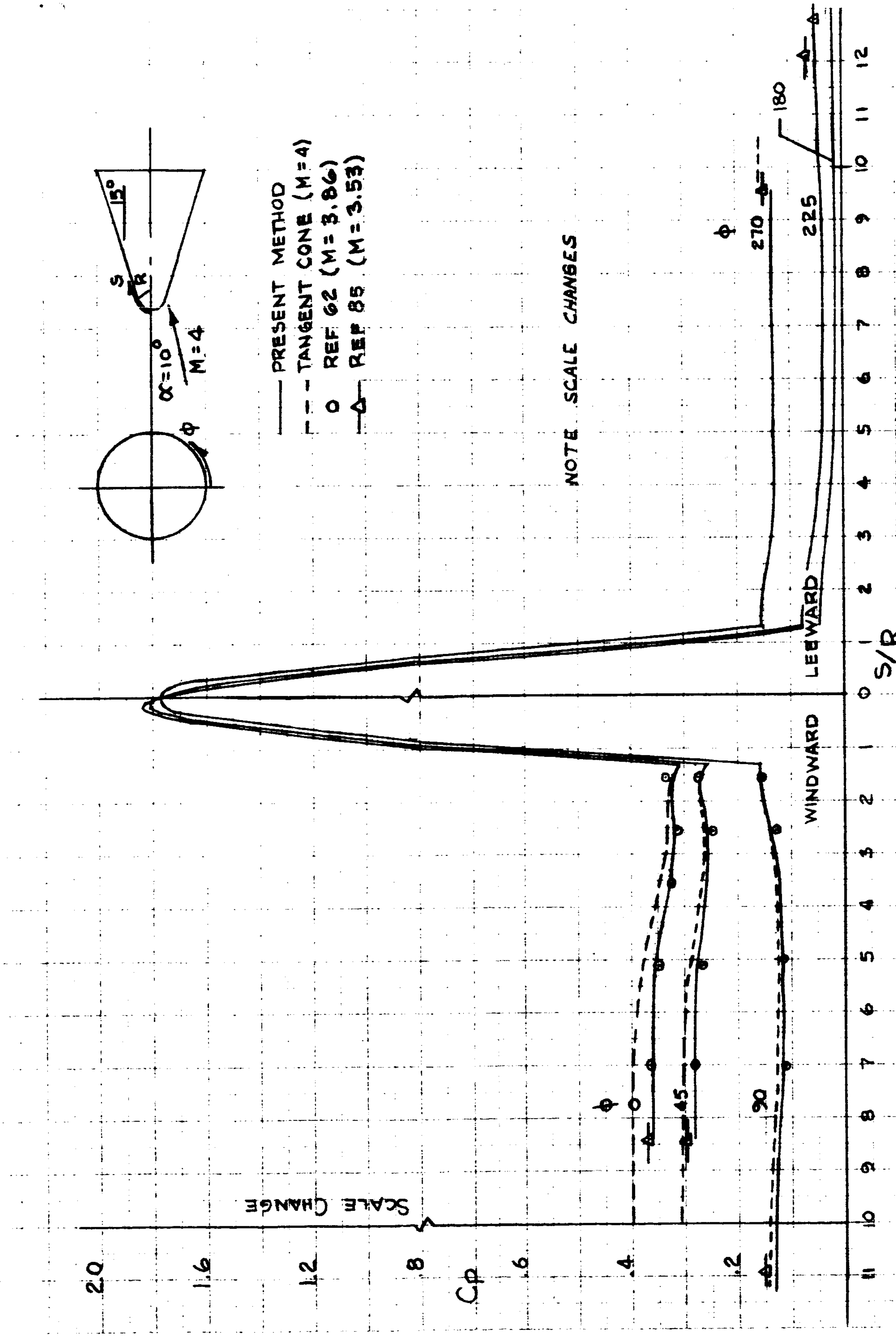

FIGURE 19

COMPARISON OF EXPERIMENTAL AND THEORETICAL SURFACE PRESSURE COEFFICIENTS ALONG MERIDIAN LINES ON A 15° SPHERE-CONE AT $\alpha = 10°$

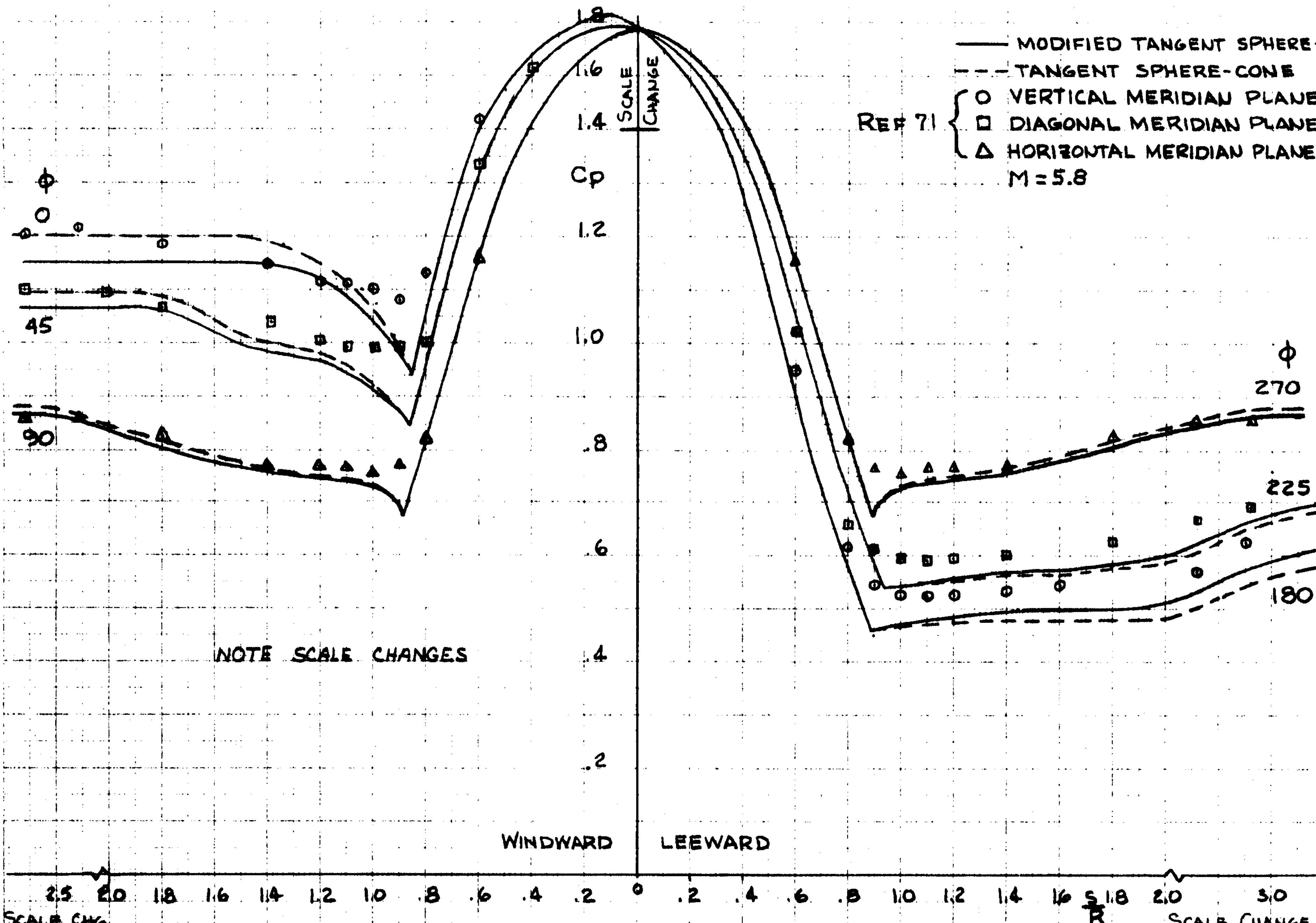

FIGURE [illegible]

COMPARISON OF EXPERIMENTAL AND THEORETICAL SURFACE PRESSURE COEFFICIENTS ALONG MERIDIAN LINES ON A 40° SPHERE-CONE AT $\alpha = 8°$

FIGURE 21

VARIATION OF PRESSURE COEFFICIENT ON A HEMISPHERE AT $\alpha = 0$

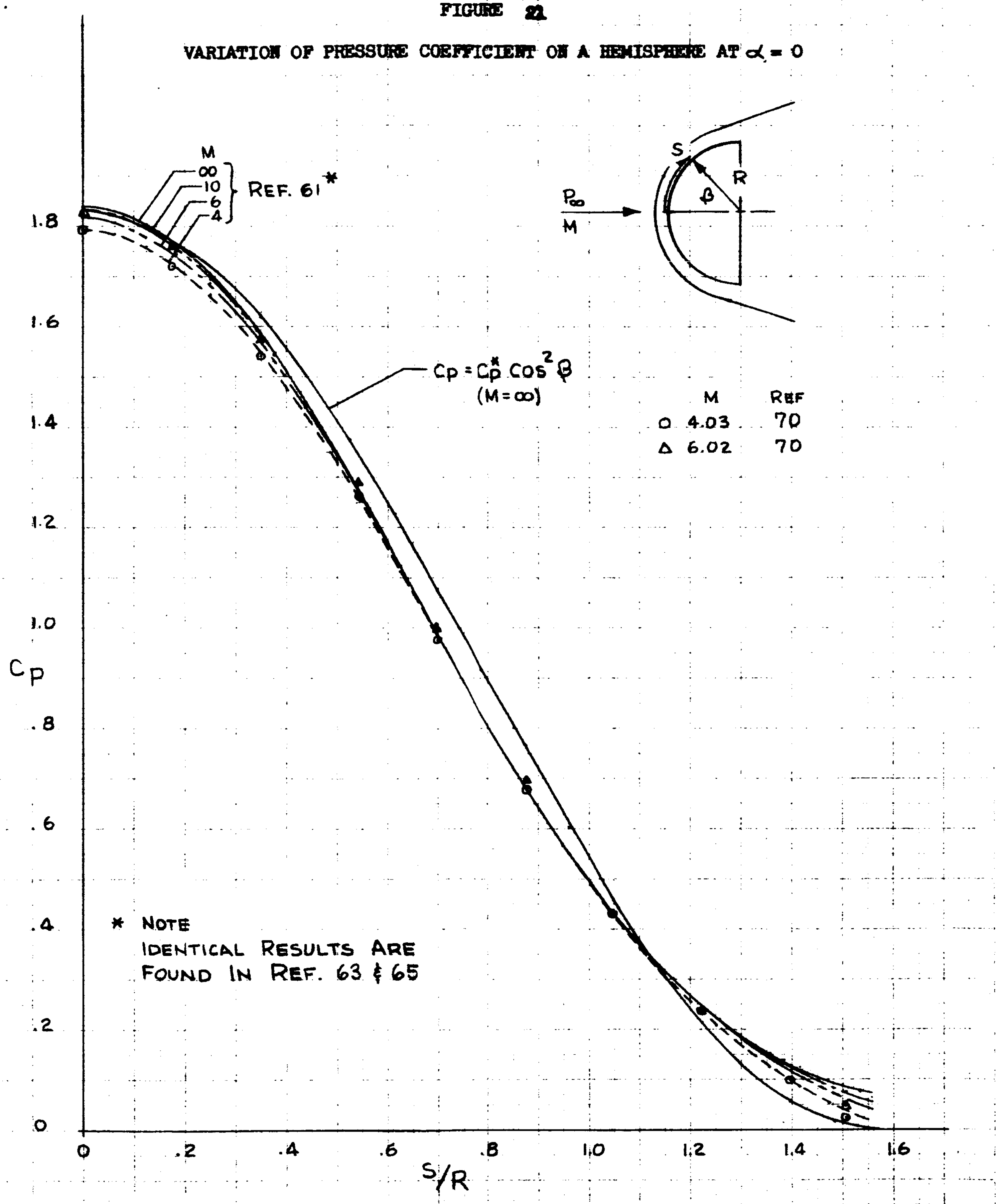

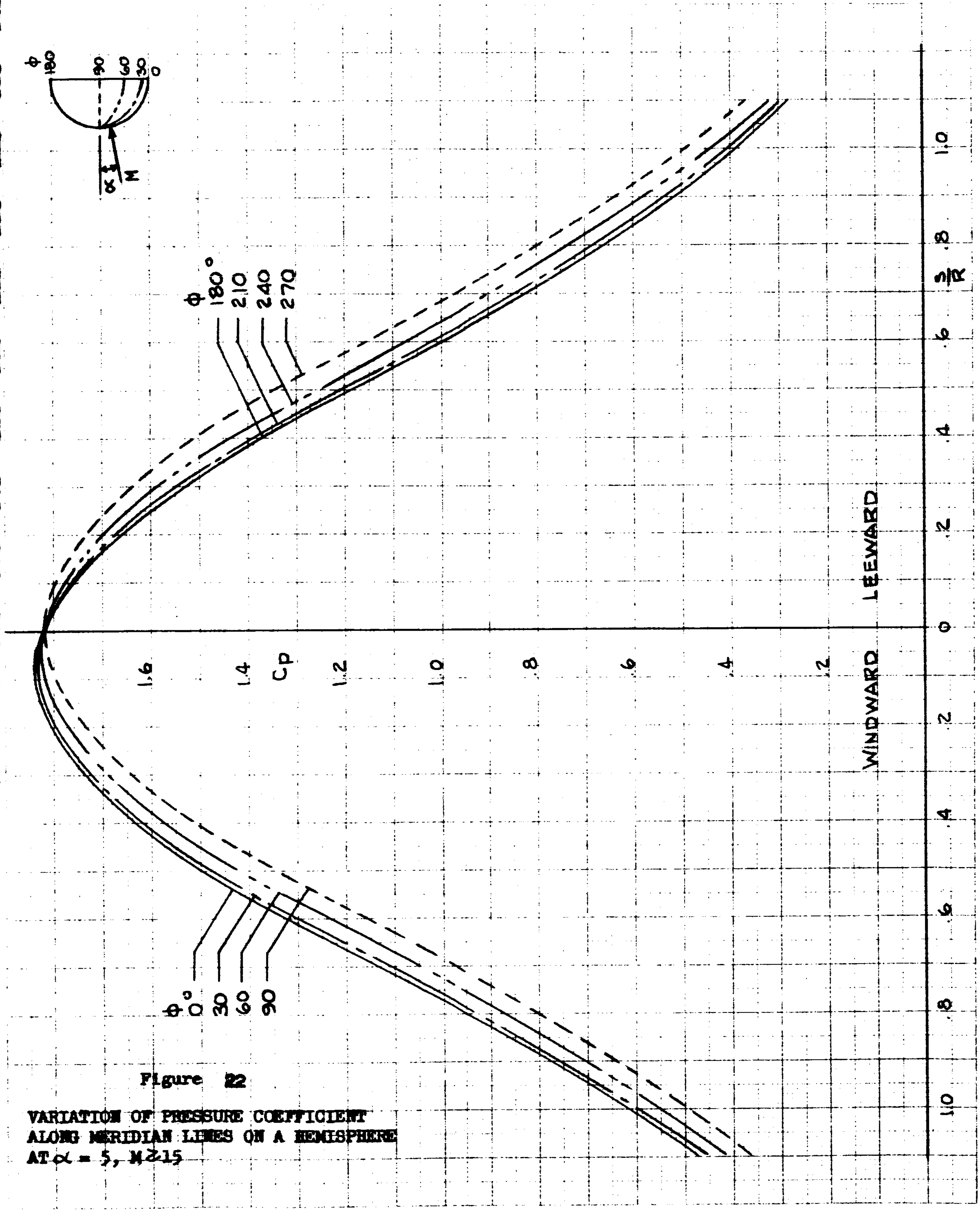

Figure 22

VARIATION OF PRESSURE COEFFICIENT
ALONG MERIDIAN LINES ON A HEMISPHERE
AT $\alpha = 5$, $M \geq 15$

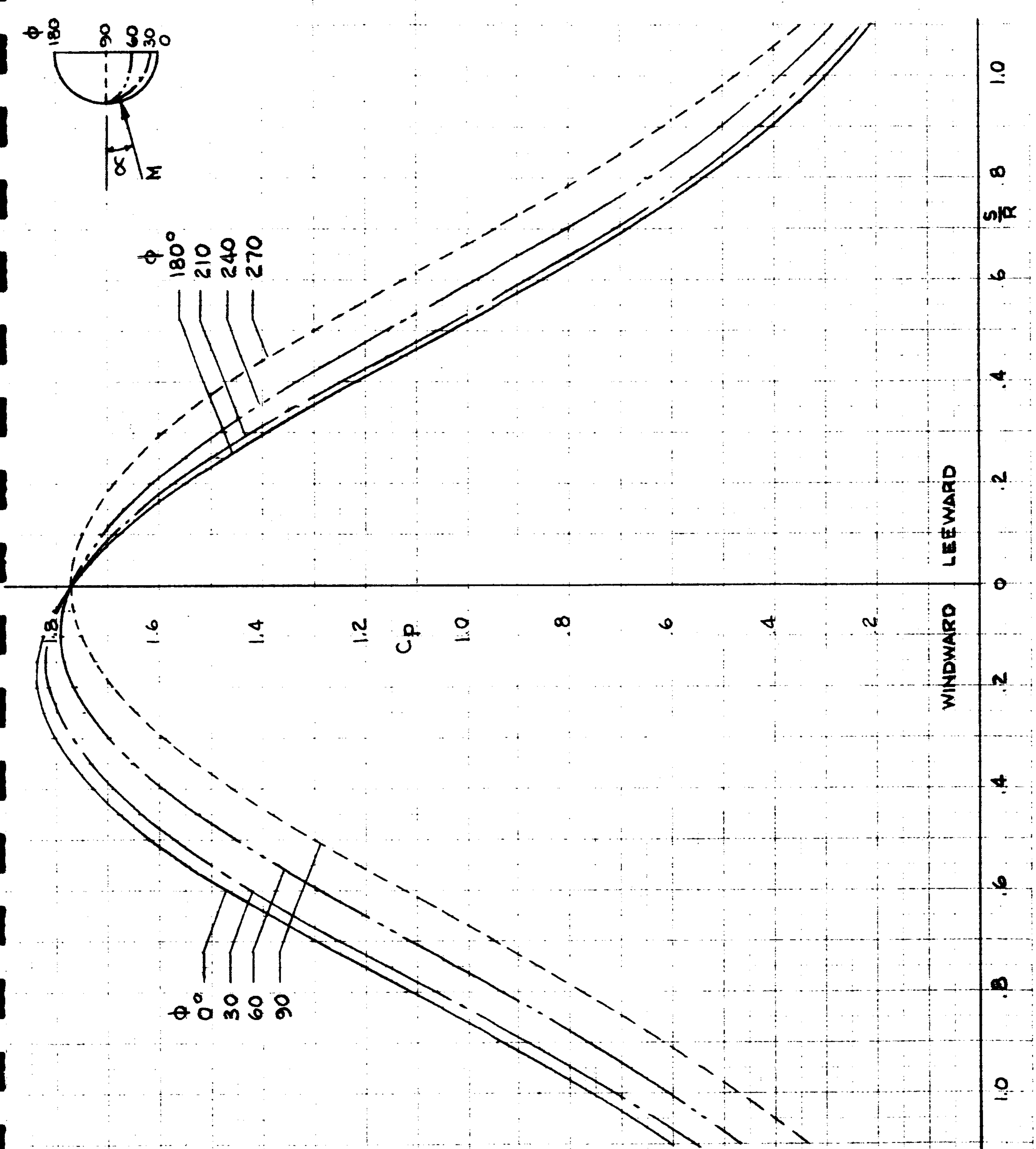

Figure 23

VARIATION OF PRESSURE COEFFICIENT ALONG MERIDIAN LINES ON A HEMISPHERE
AT $\alpha = 10°$, $M \geq 15$

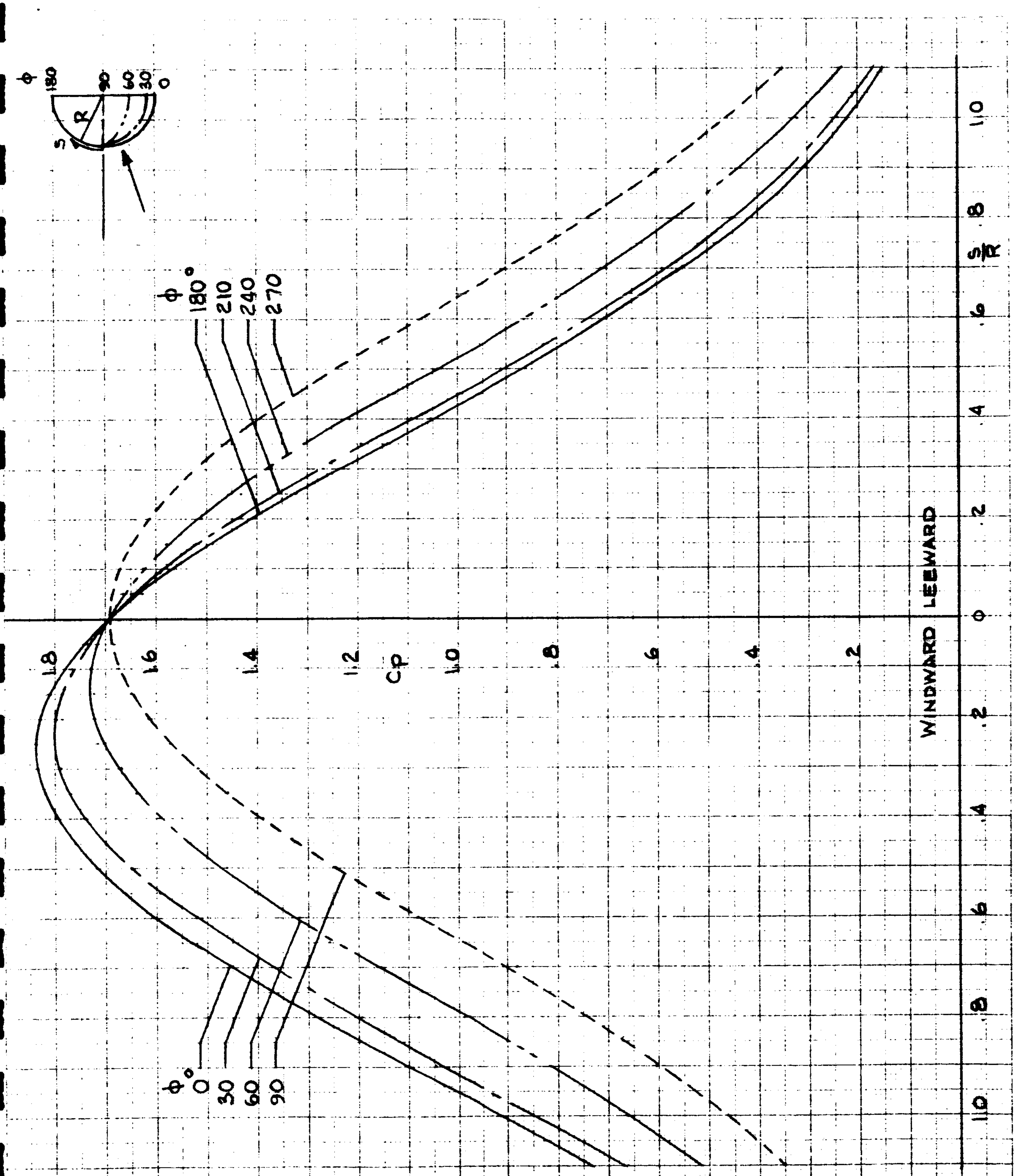

FIGURE [illegible]

VARIATION OF PRESSURE COEFFICIENT ALONG MERIDIAN LINES ON A HEMISPHERE AT $\alpha = 15$, $M \geq 15$

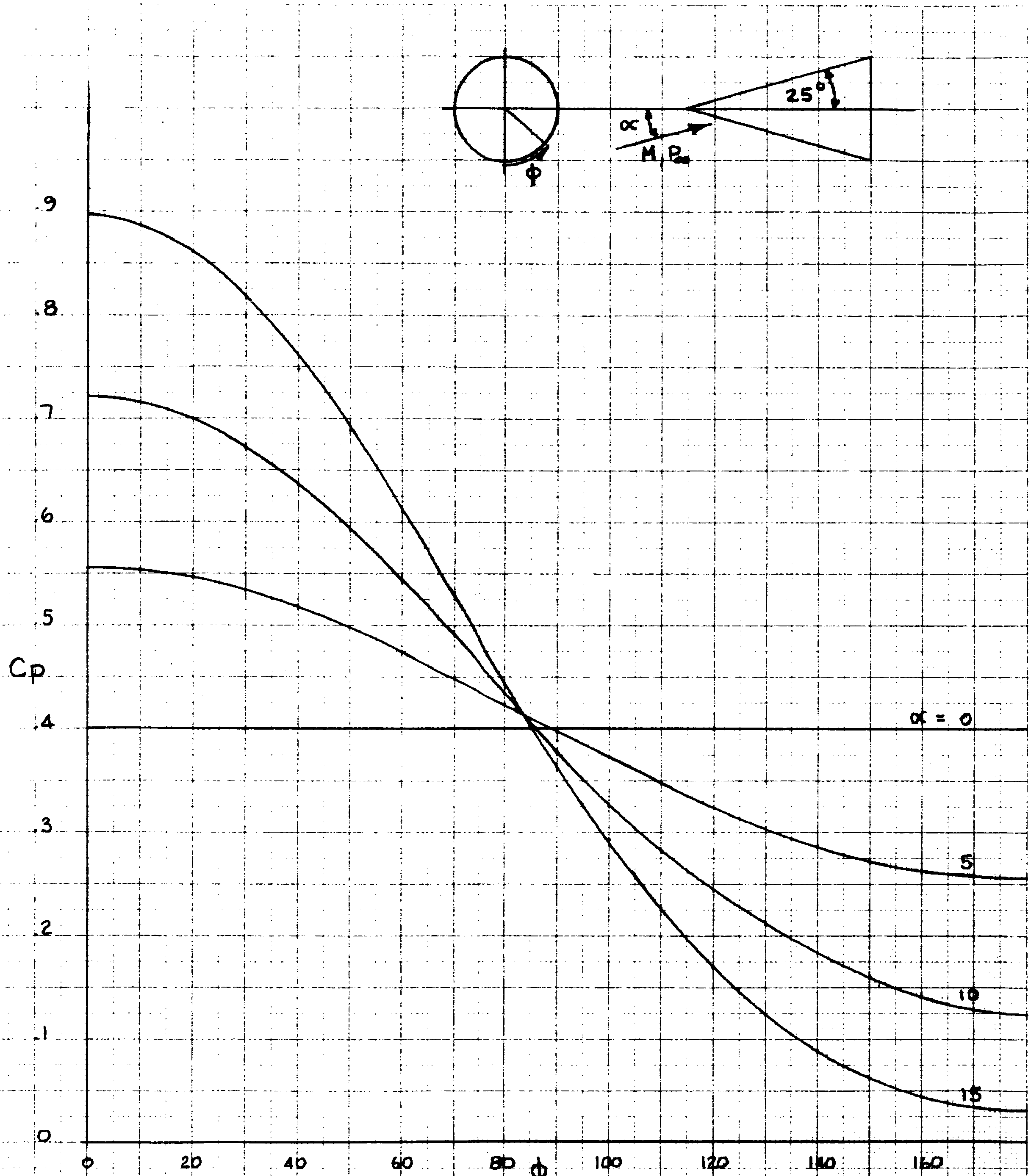

FIGURE 25

CIRCUMFERENTIAL PRESSURE DISTRIBUTION ON A 25° SHARP CONE AT M = 4

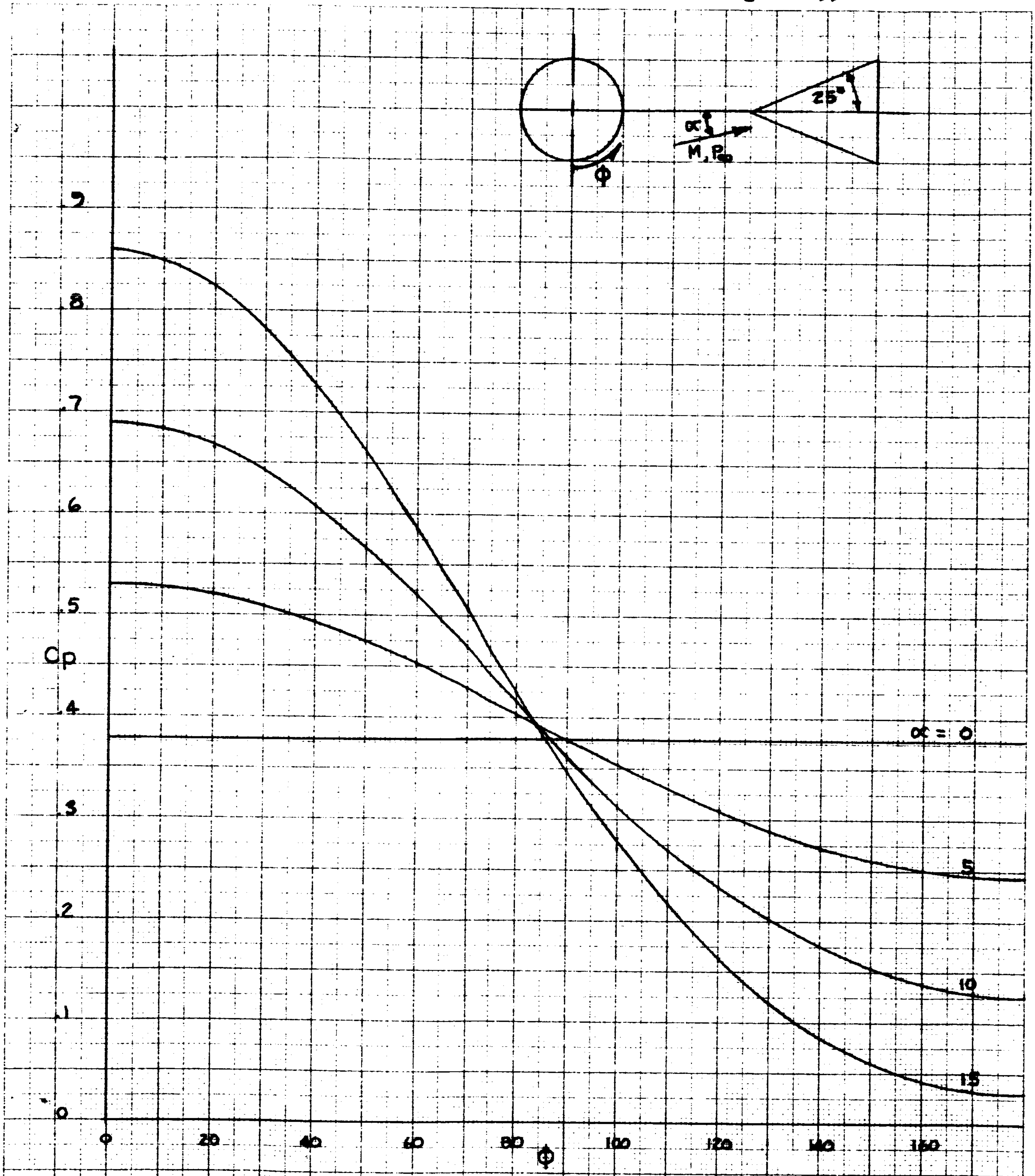

FIGURE [illegible]

CIRCUMFERENTIAL PRESSURE DISTRIBUTION ON A 25° SHARP CONE AT M = 10

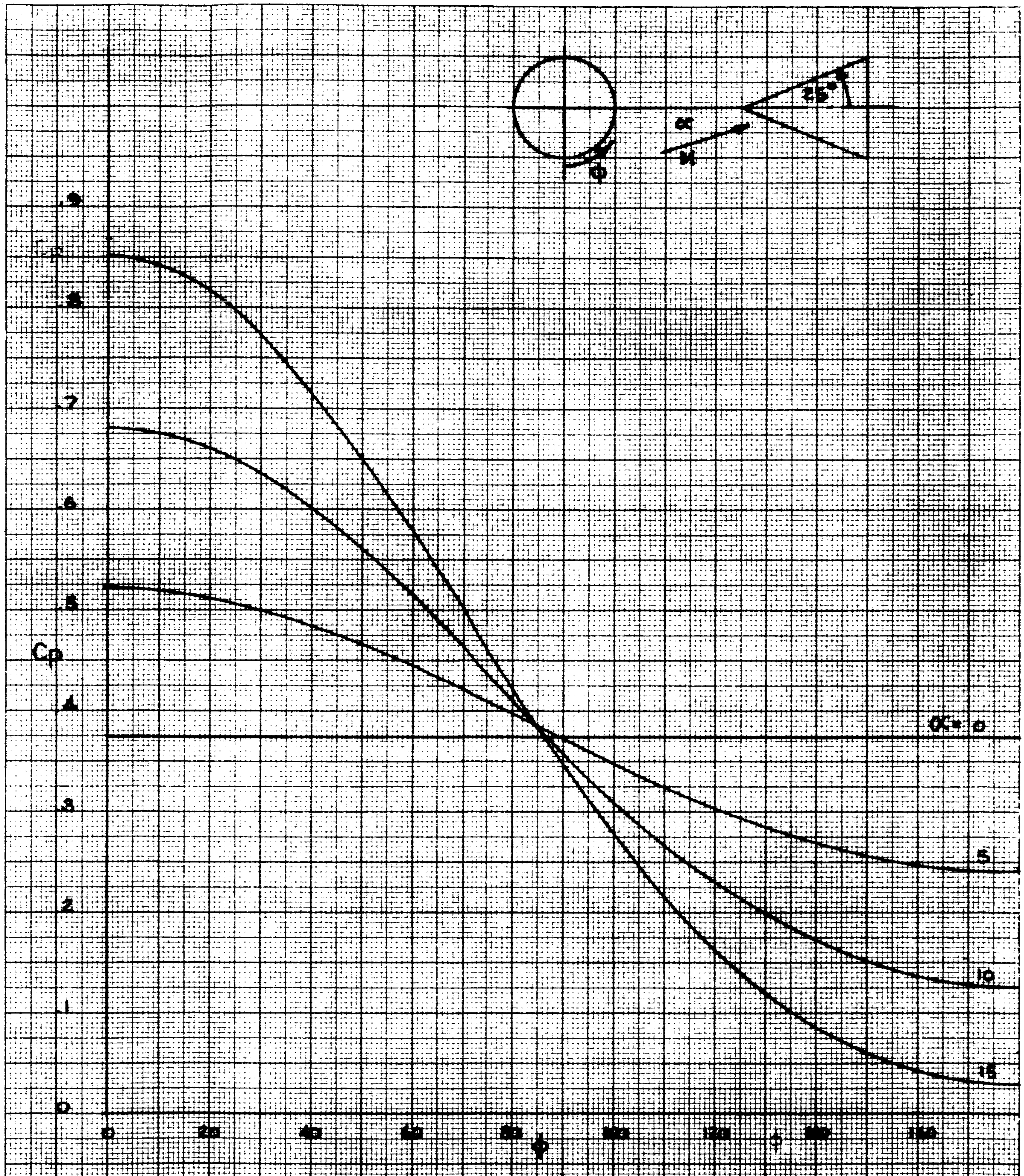
25°
α
M
Φ
Cp
.9
.8
.7
.6
.5
.4
.3
.2
.1
0
α = 0
5
10
15
0
20
40
60
80
100
120
140
160
Φ

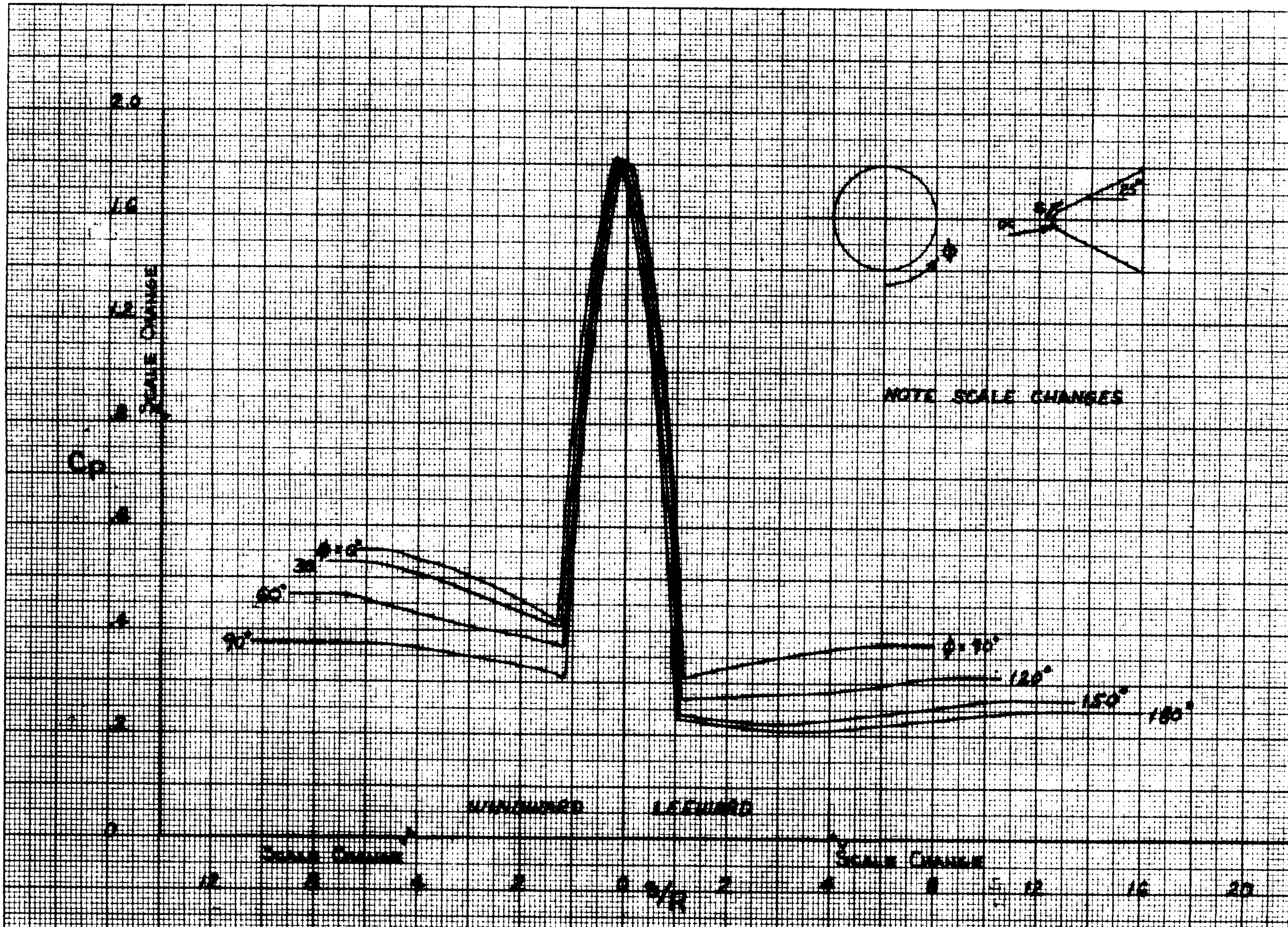

FIGURE [illegible]

VARIATION OF PRESSURE COEFFICIENT ALONG MERIDIAN LINES ON A 25° SPHERE-CONE AT M=[illegible], $\alpha = 5°$

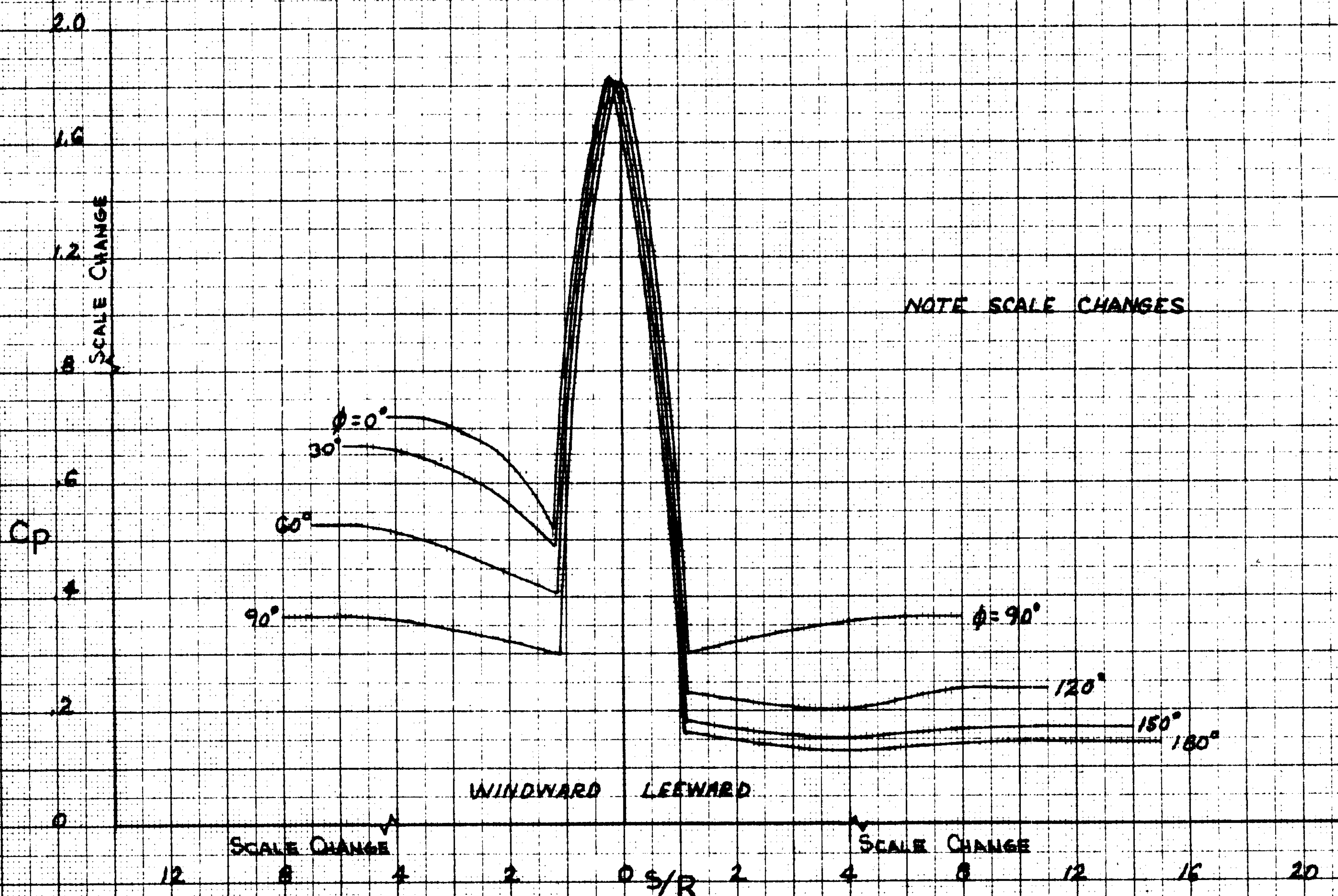

FIGURE [illegible]

VARIATION OF PRESSURE COEFFICIENT ALONG MERIDIAN LINES ON A 25° SPHERE-CONE AT $M=4.0$, $\alpha=10°$

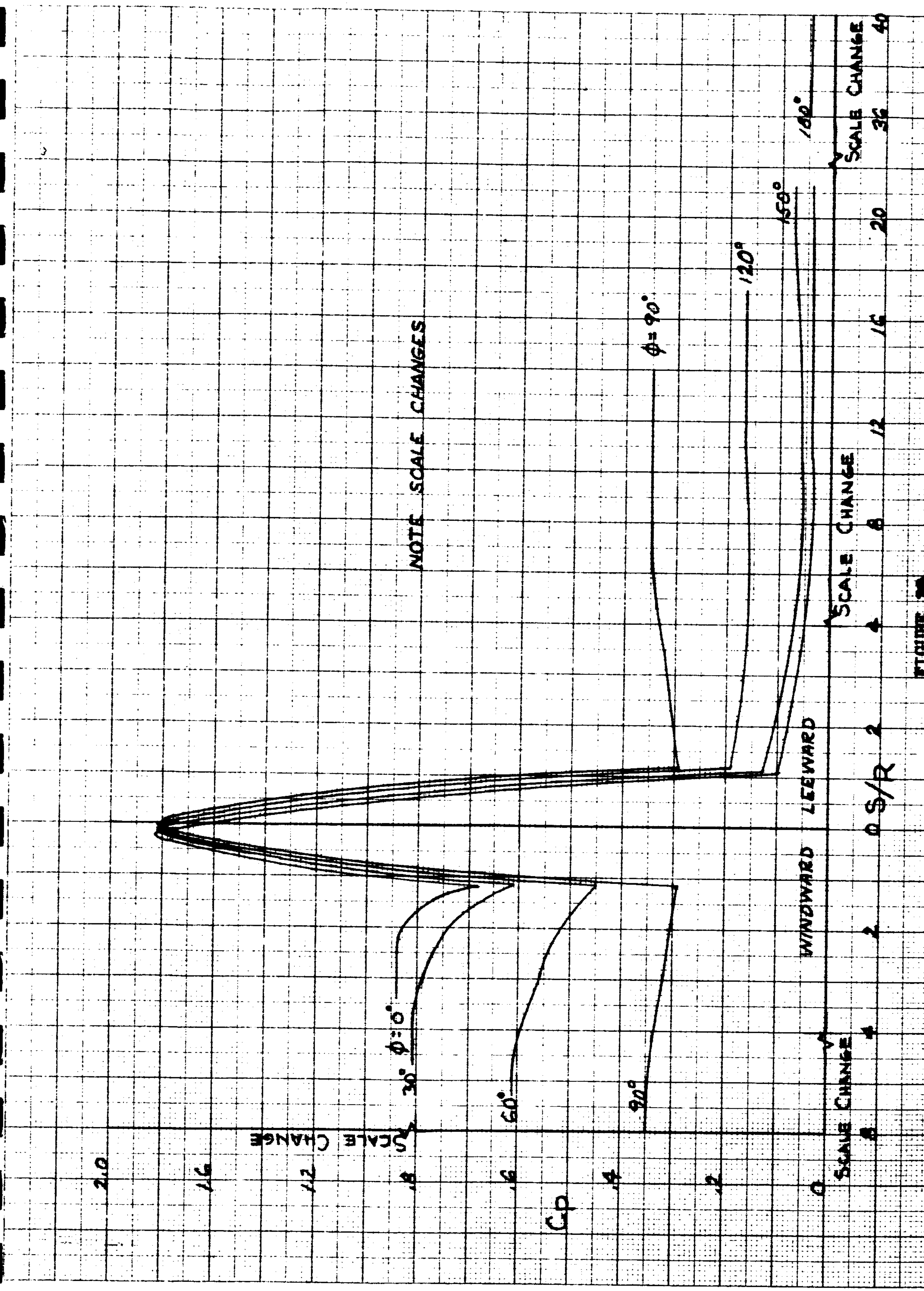

FIGURE [illegible]

VARIATION OF PRESSURE COEFFICIENT ALONG MERIDIAN LINES ON A 25° SPHERE-CONE AT $M = 4.0$, $\alpha = 15°$

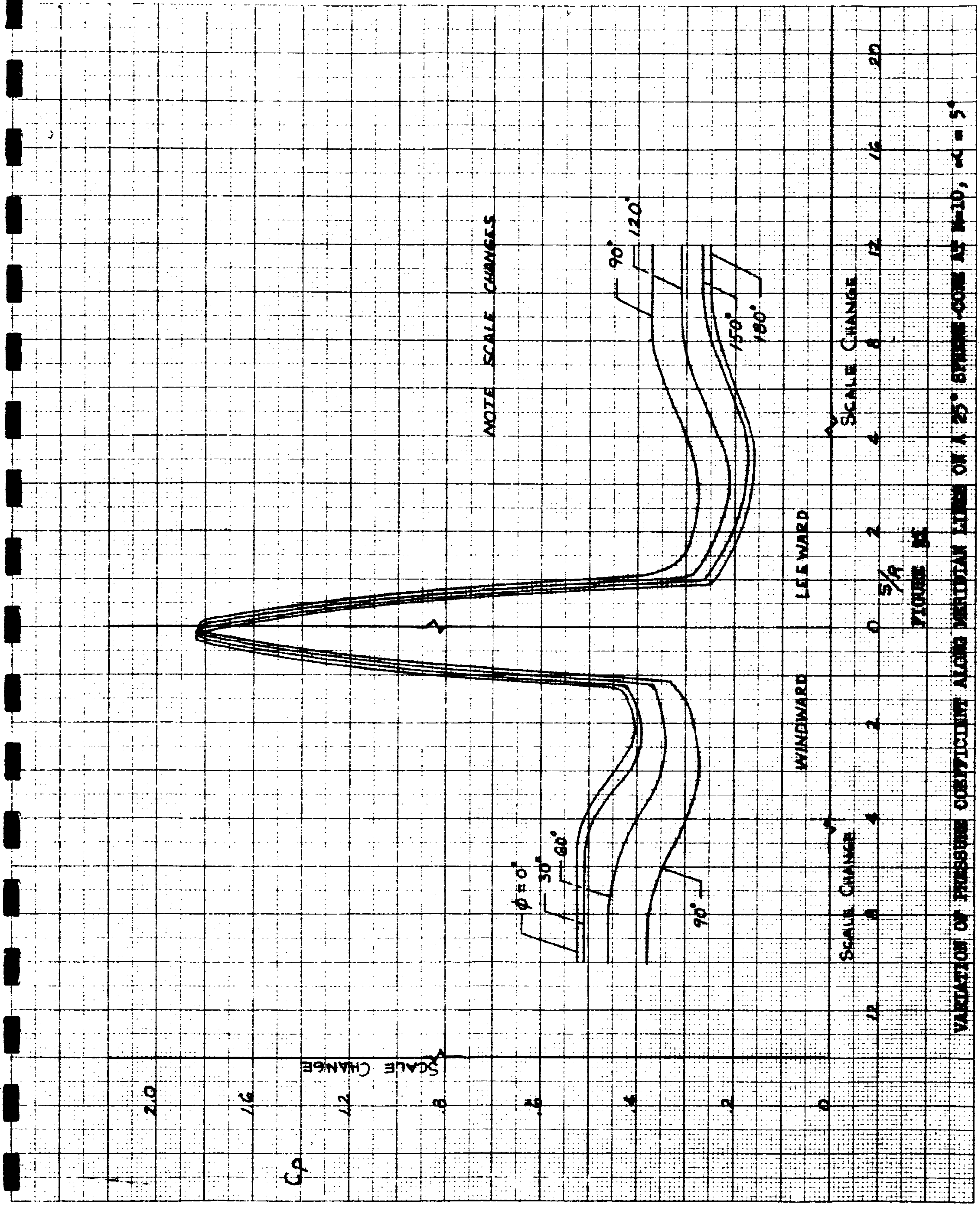

FIGURE [illegible]

VARIATION OF PRESSURE COEFFICIENT ALONG MERIDIAN LINES ON A 25° SPHERE-CONE AT M=10, $\alpha = 5°$

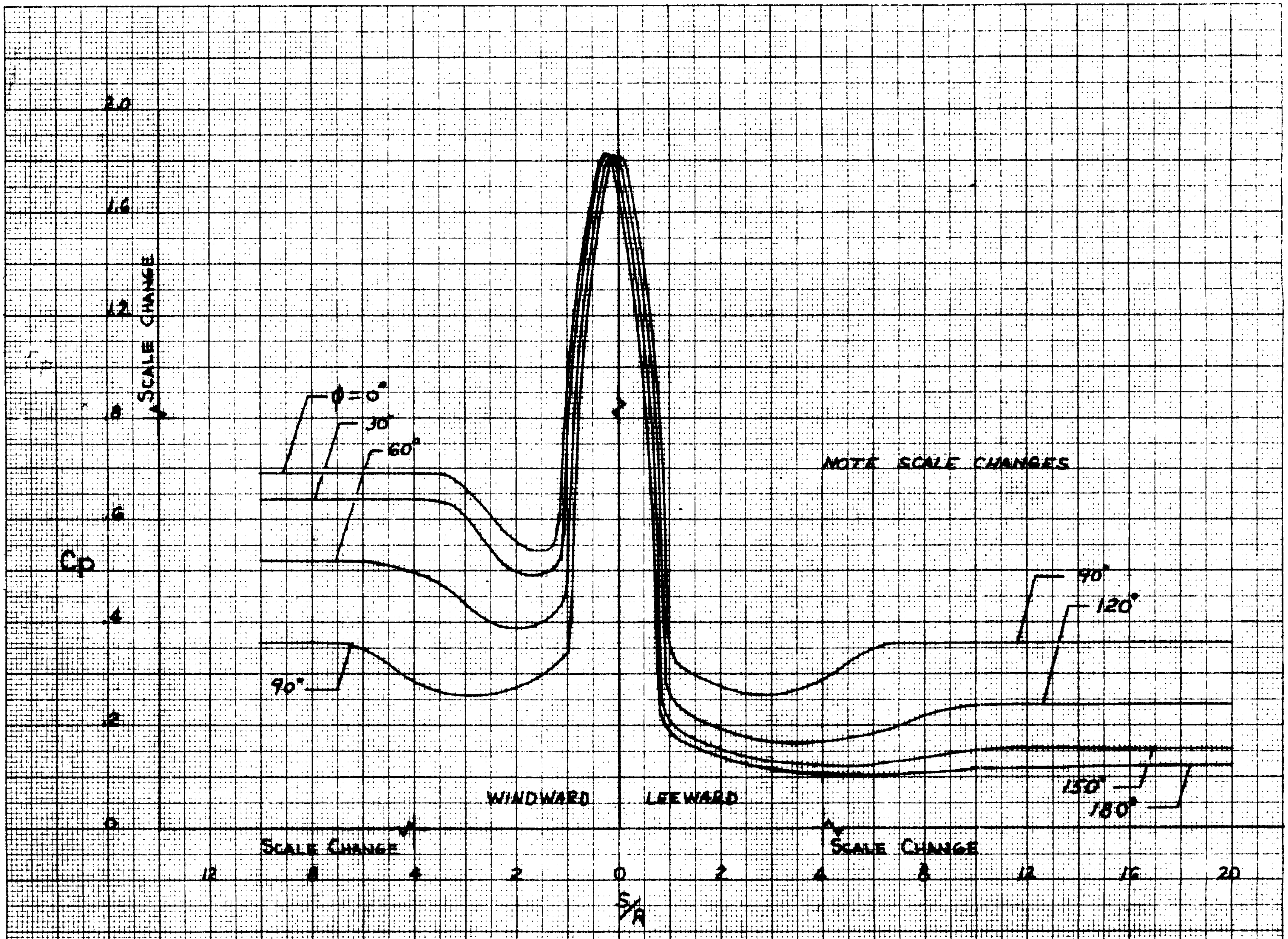

FIGURE [illegible]

VARIATION OF PRESSURE COEFFICIENT ALONG MERIDIAN LINES ON A 25° SPHERE-CONE AT M=19, α = 10°

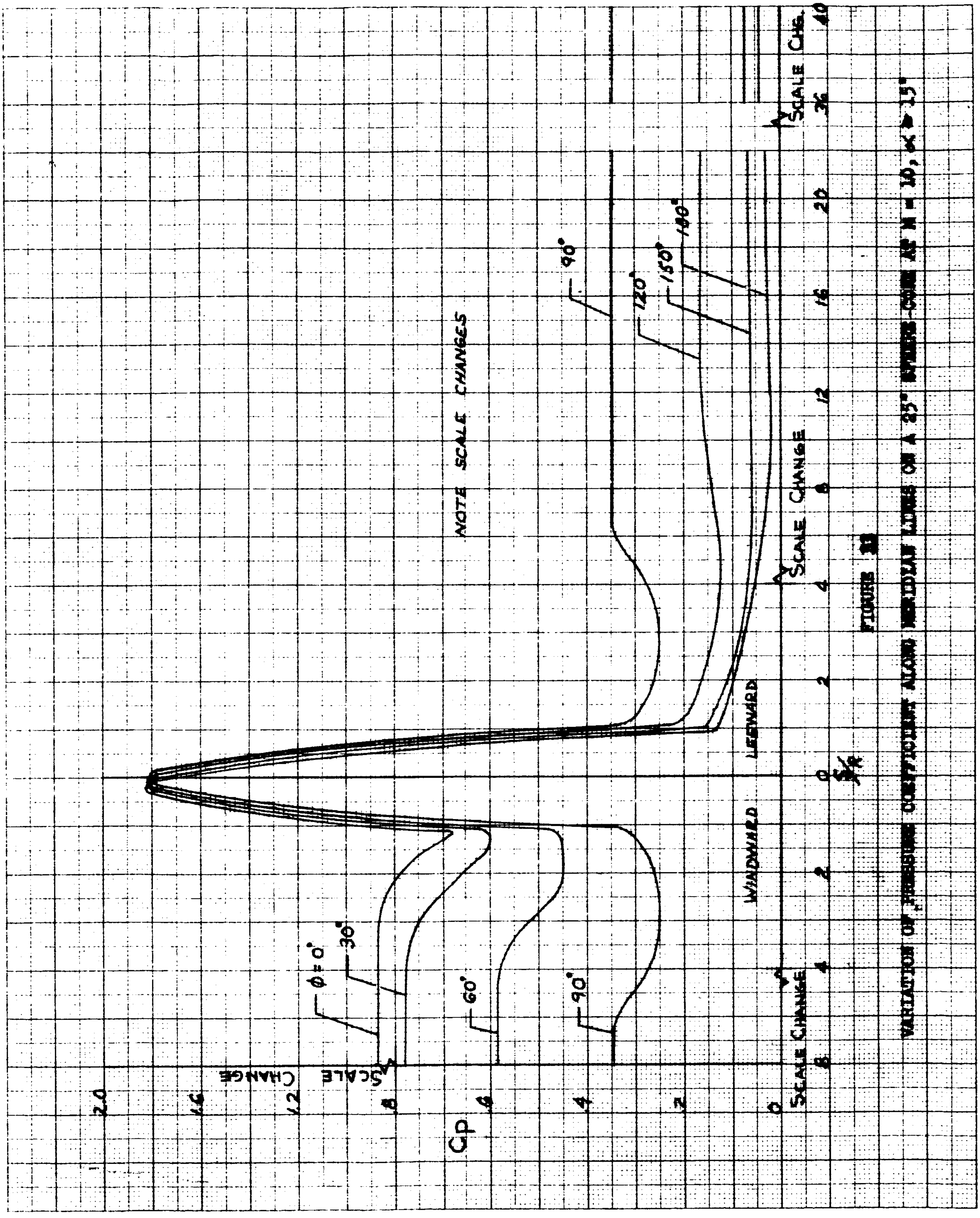

FIGURE 33

VARIATION OF PRESSURE COEFFICIENT ALONG MERIDIAN LINES ON A 25° SPHERE-CONE AT M = 10, α = 15°

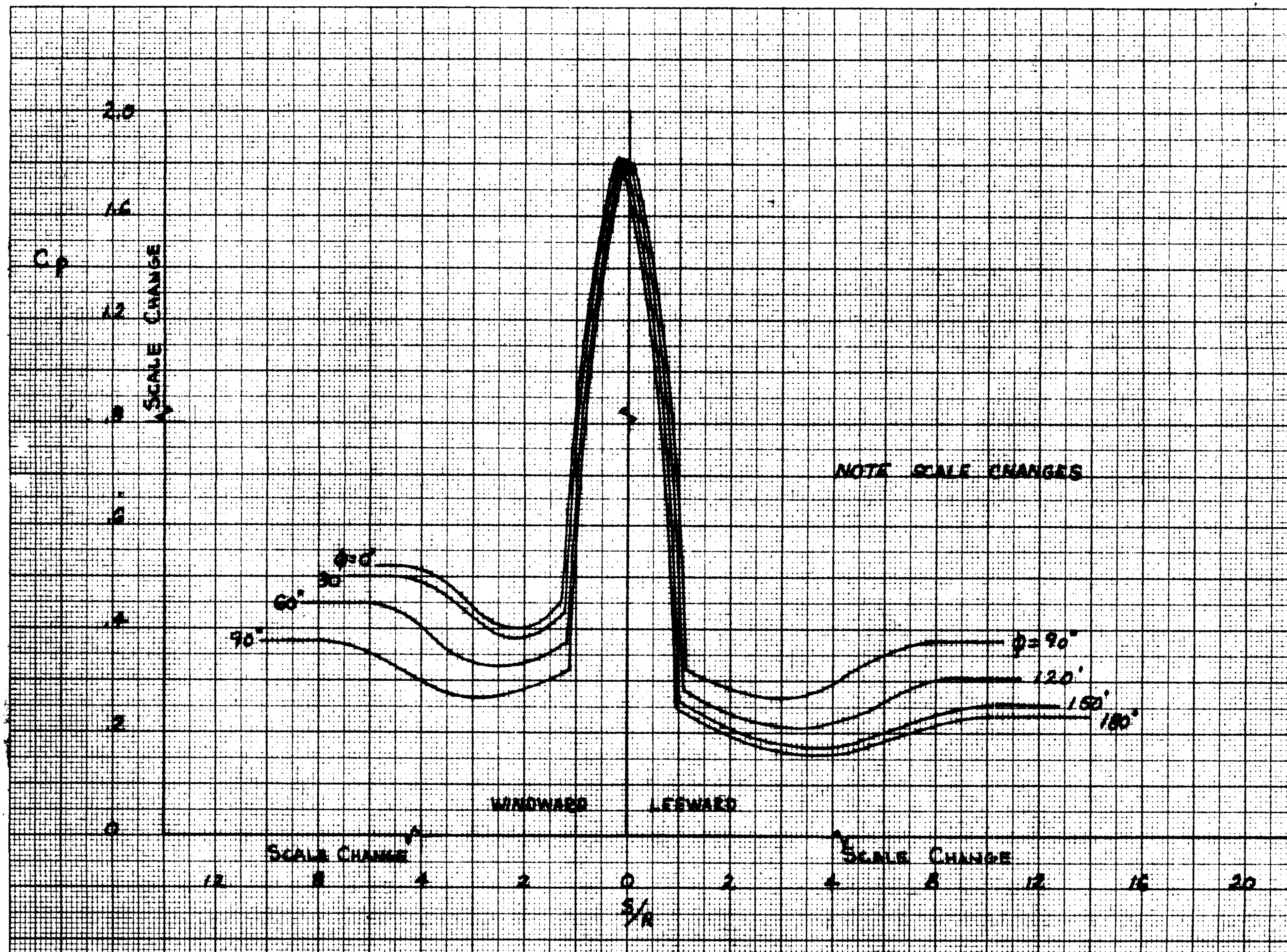

FIGURE [illegible]

VARIATION OF PRESSURE COEFFICIENT ALONG MERIDIAN LINES ON A 25° SPHERE-CONE AT $M \geq 15$, $\alpha = 5°$

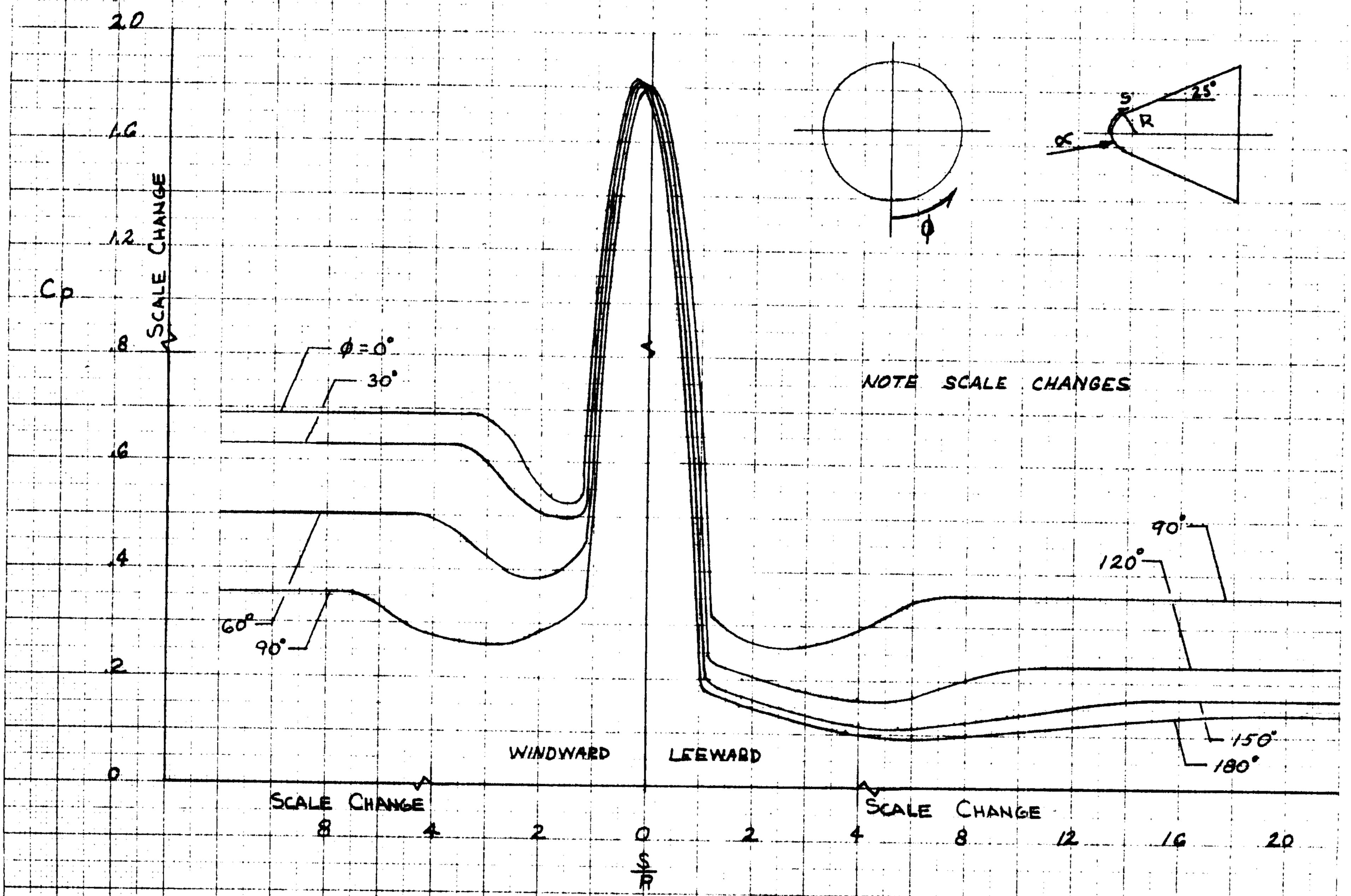

FIGURE 35

VARIATION OF PRESSURE COEFFICIENT ALONG MERIDIAN LINES ON A 25° SPHERE-CONE AT $M \geq 15$, $\alpha = 10°$

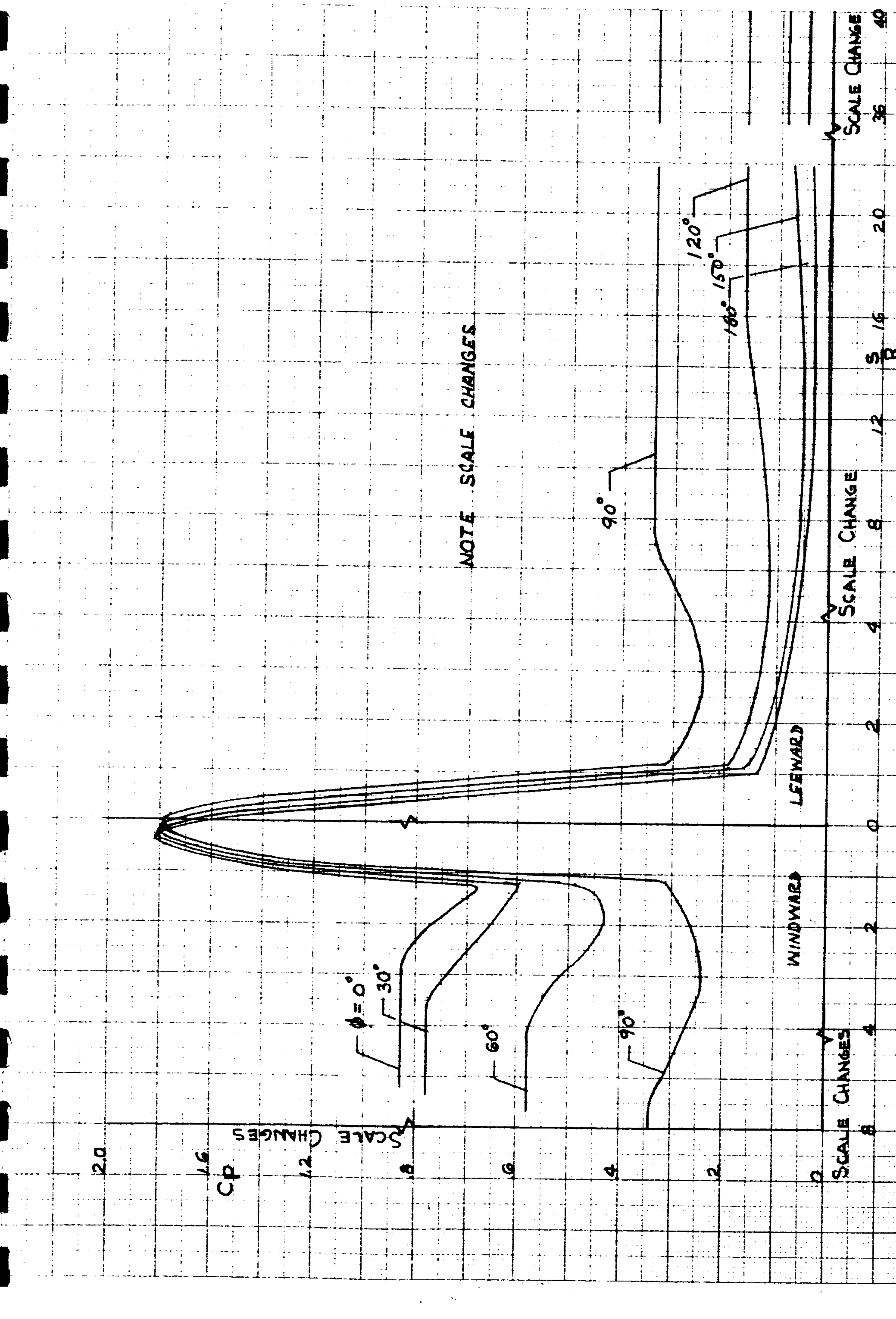

FIGURE [illegible]

VARIATION OF PRESSURE COEFFICIENT ALONG MERIDIAN LINES ON A 25° SPHERE-CONE AT M ≥15, α = 15°

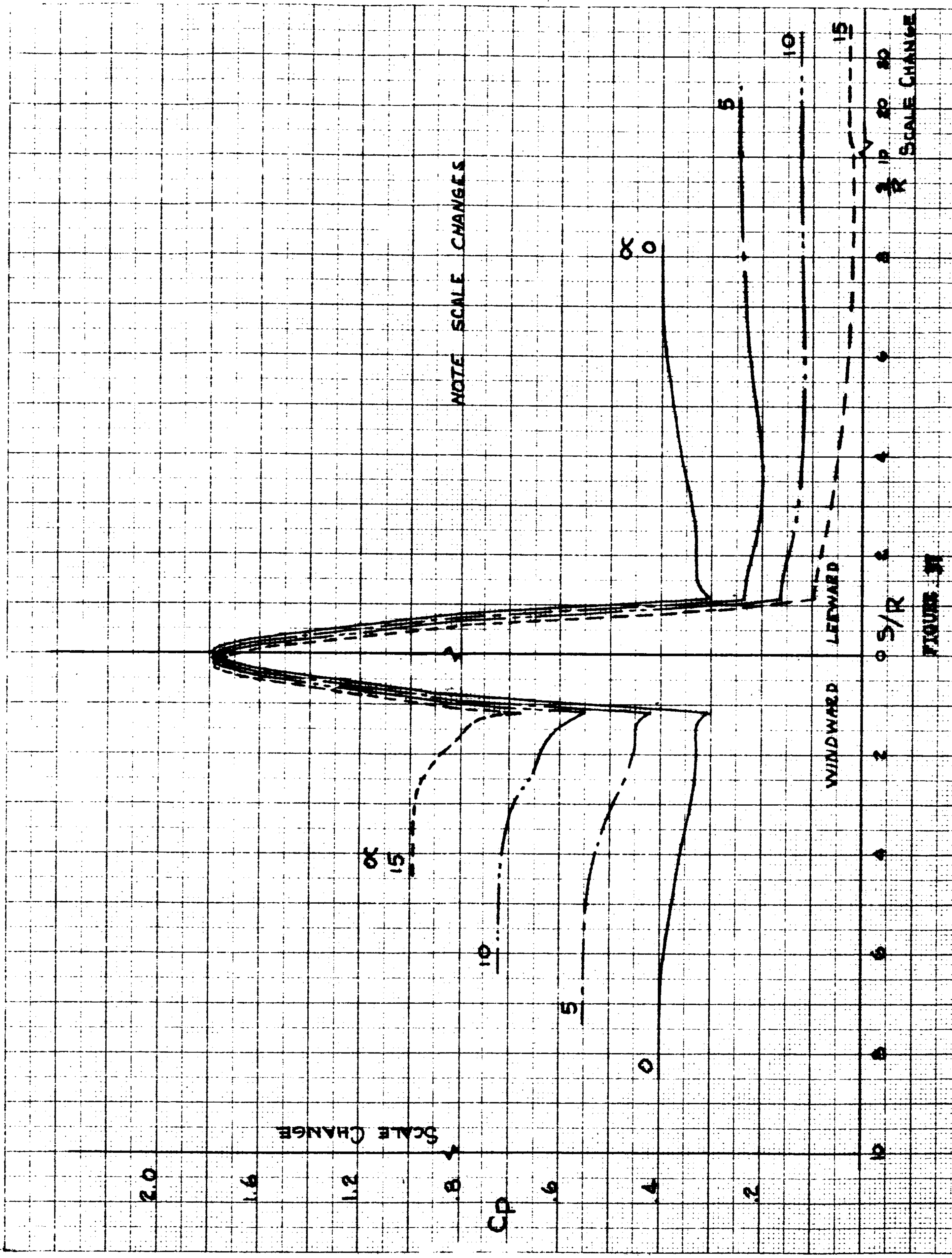

FIGURE [illegible]

VARIATION OF PRESSURE COEFFICIENT ALONG VERTICAL MERIDIAN LINE AT ANGLE OF ATTACK, M = 4.0

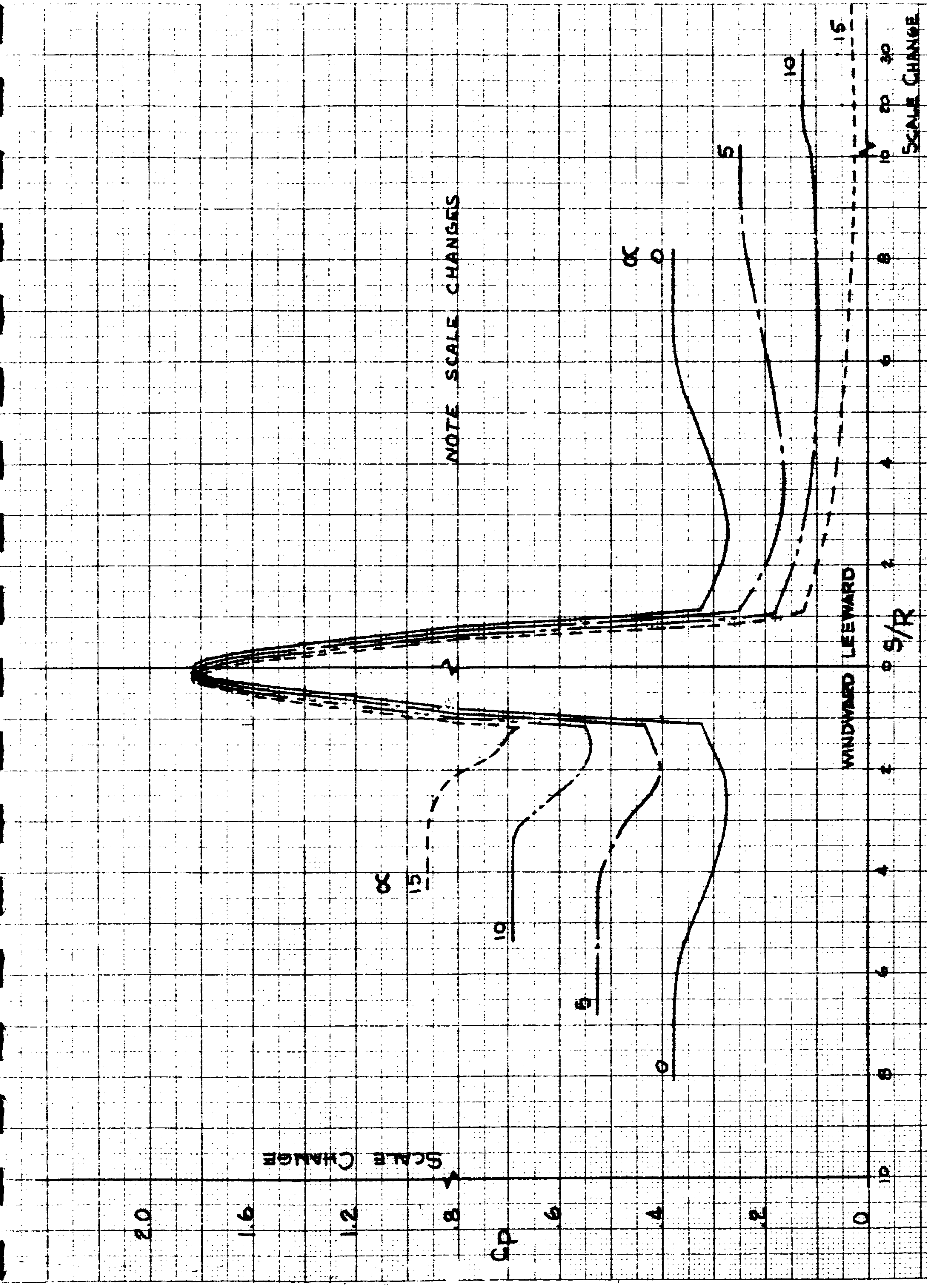

FIGURE

VARIATION OF PRESSURE COEFFICIENT ALONG VERTICAL MERIDIAN LINE AT ANGLES OF ATTACK, M = 10

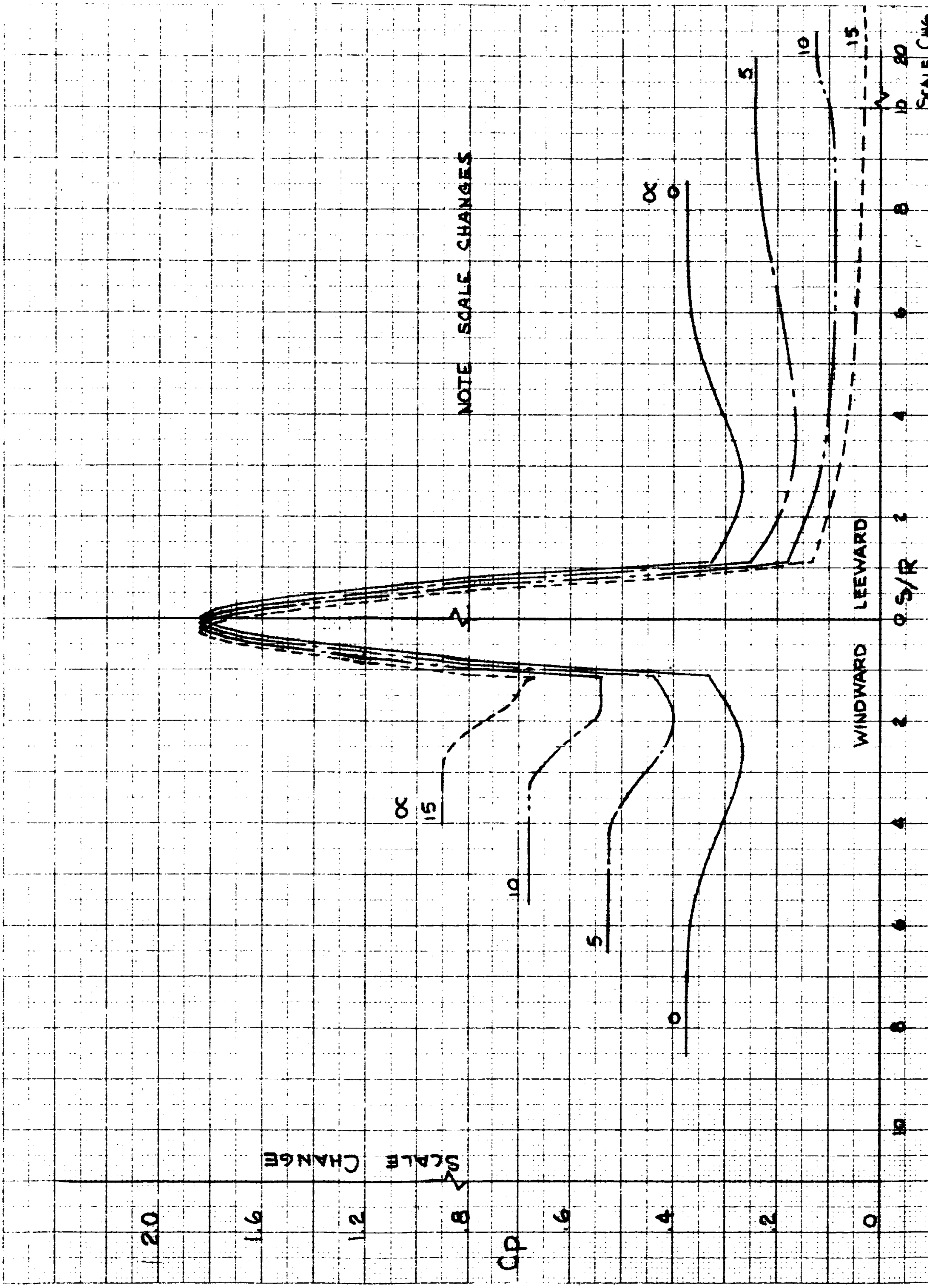

FIGURE 39

VARIATION OF PRESSURE COEFFICIENT ALONG VERTICAL MERIDIAN LINE AT ANGLES OF ATTACK, M ≥ 15

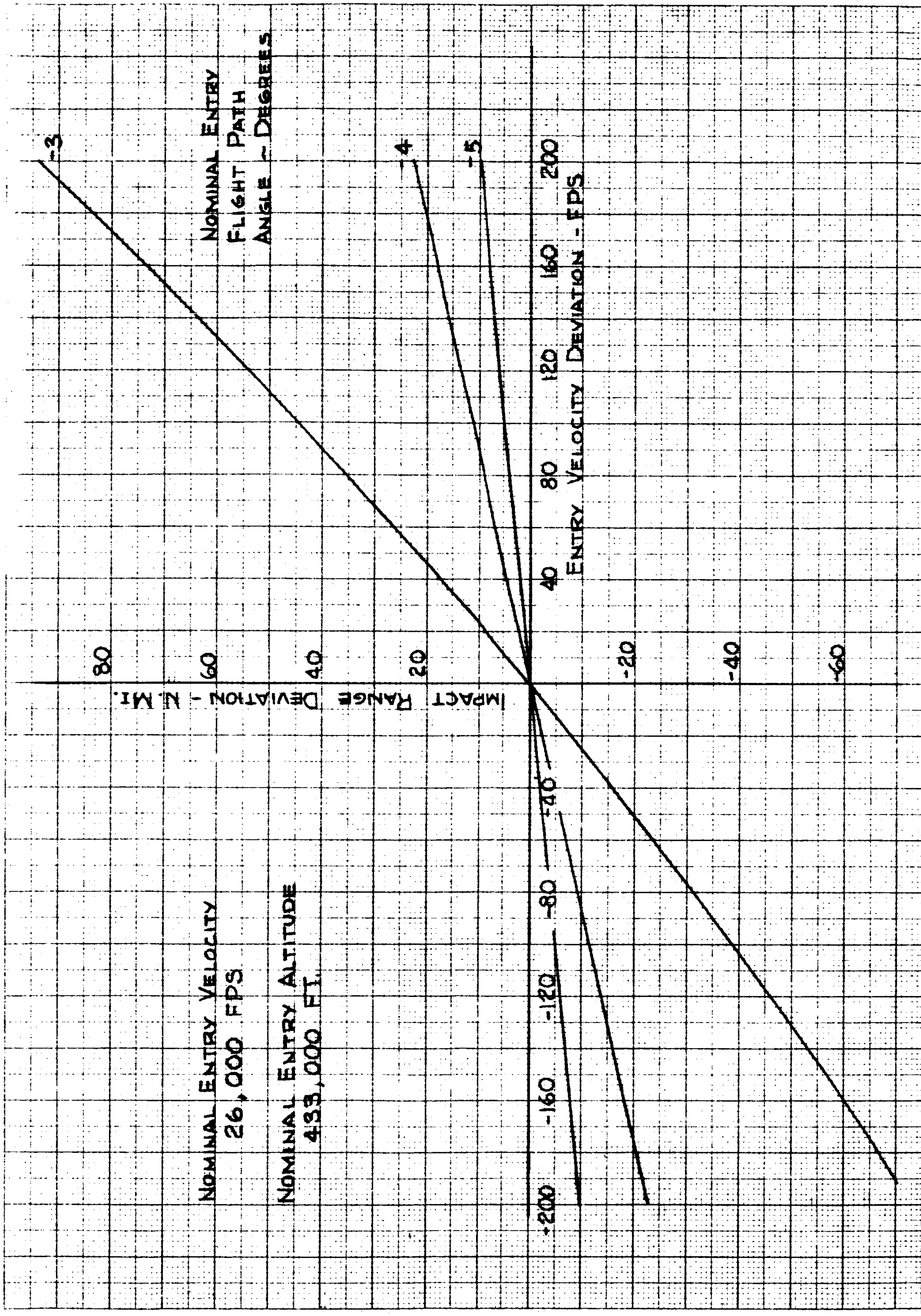

FIGURE 40

EFFECT OF ENTRY VELOCITY DEVIATIONS ON IMPACT RANGE FOR NOMINAL ENTRY FLIGHT PATH ANGLES OF -3, -4 AND -5 DEGREES

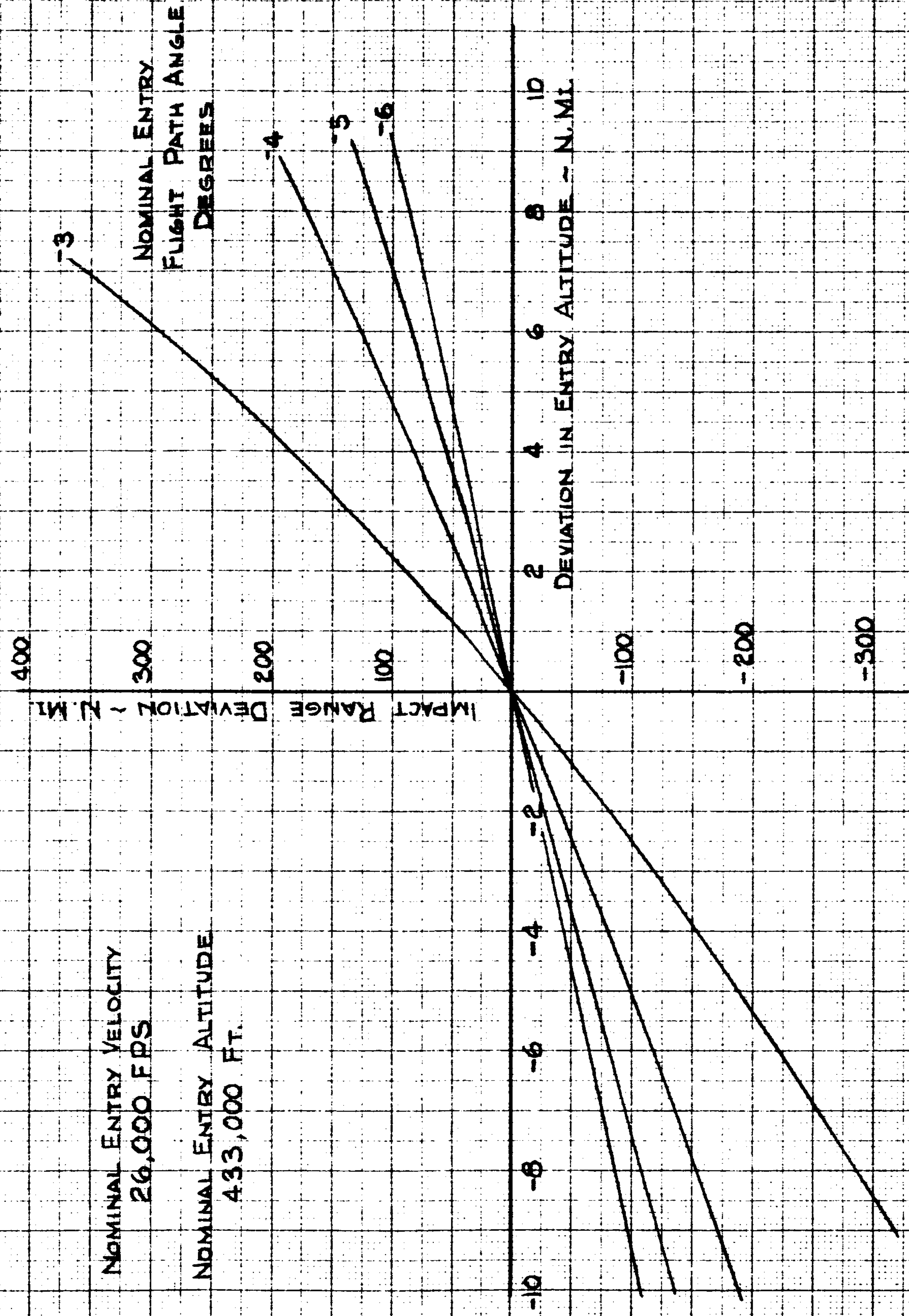

FIGURE 41

EFFECT OF VARIATIONS IN ENTRY ALTITUDE ON IMPACT RANGE FOR NOMINAL ENTRY FLIGHT PATH ANGLES OF -3, -4, -5 AND -6 DEGREES

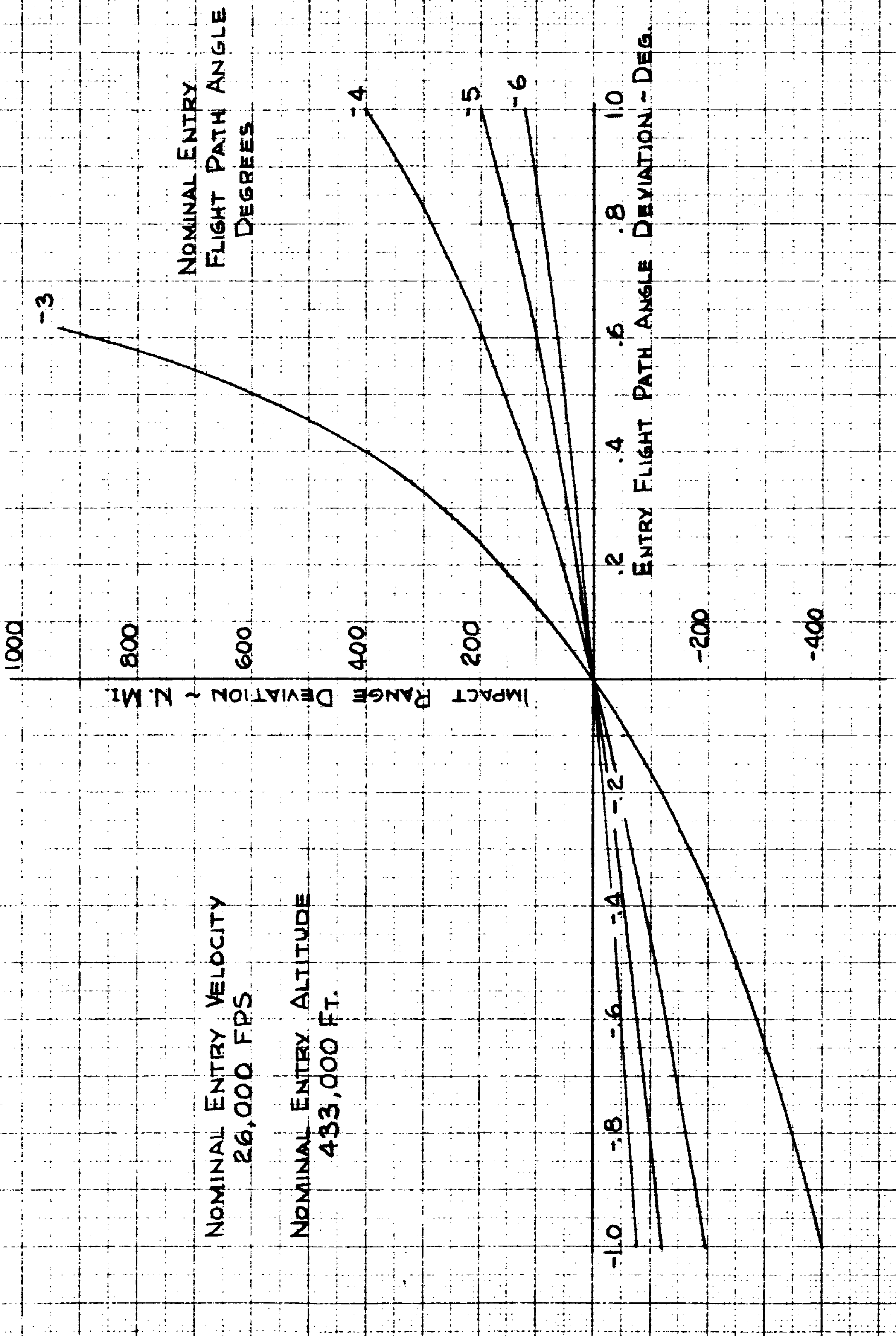

FIGURE 42

EFFECT OF VARIATIONS IN ENTRY FLIGHT PATH ANGLE ON IMPACT RANGE FOR NOMINAL ENTRY FLIGHT PATH ANGLES OF -3, -4, -5 AND -6 DEGREES

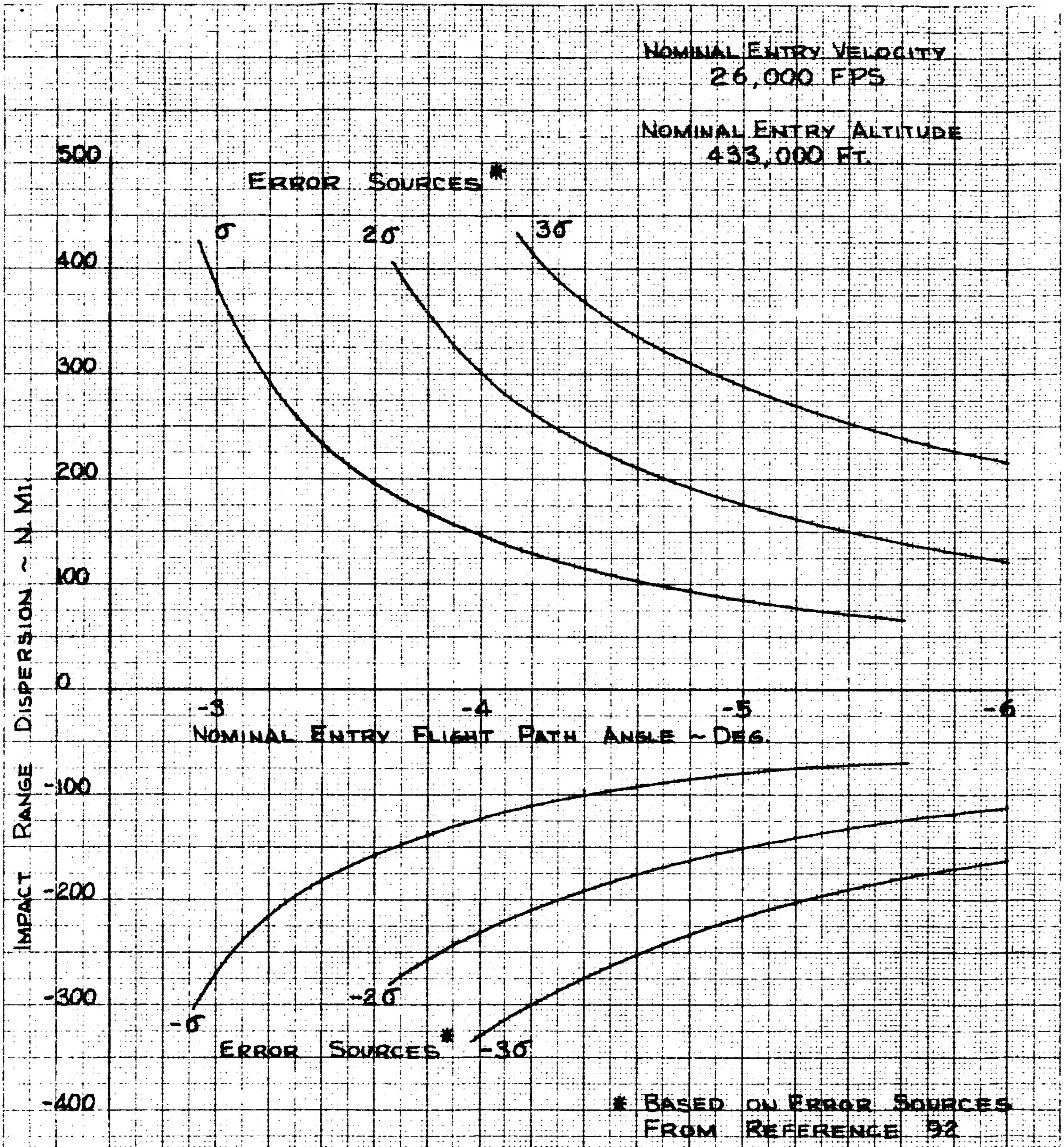

FIGURE 43

EFFECT OF ENTRY ANGLE ON POSITIVE AND NEGATIVE IMPACT RANGE DEVIATIONS

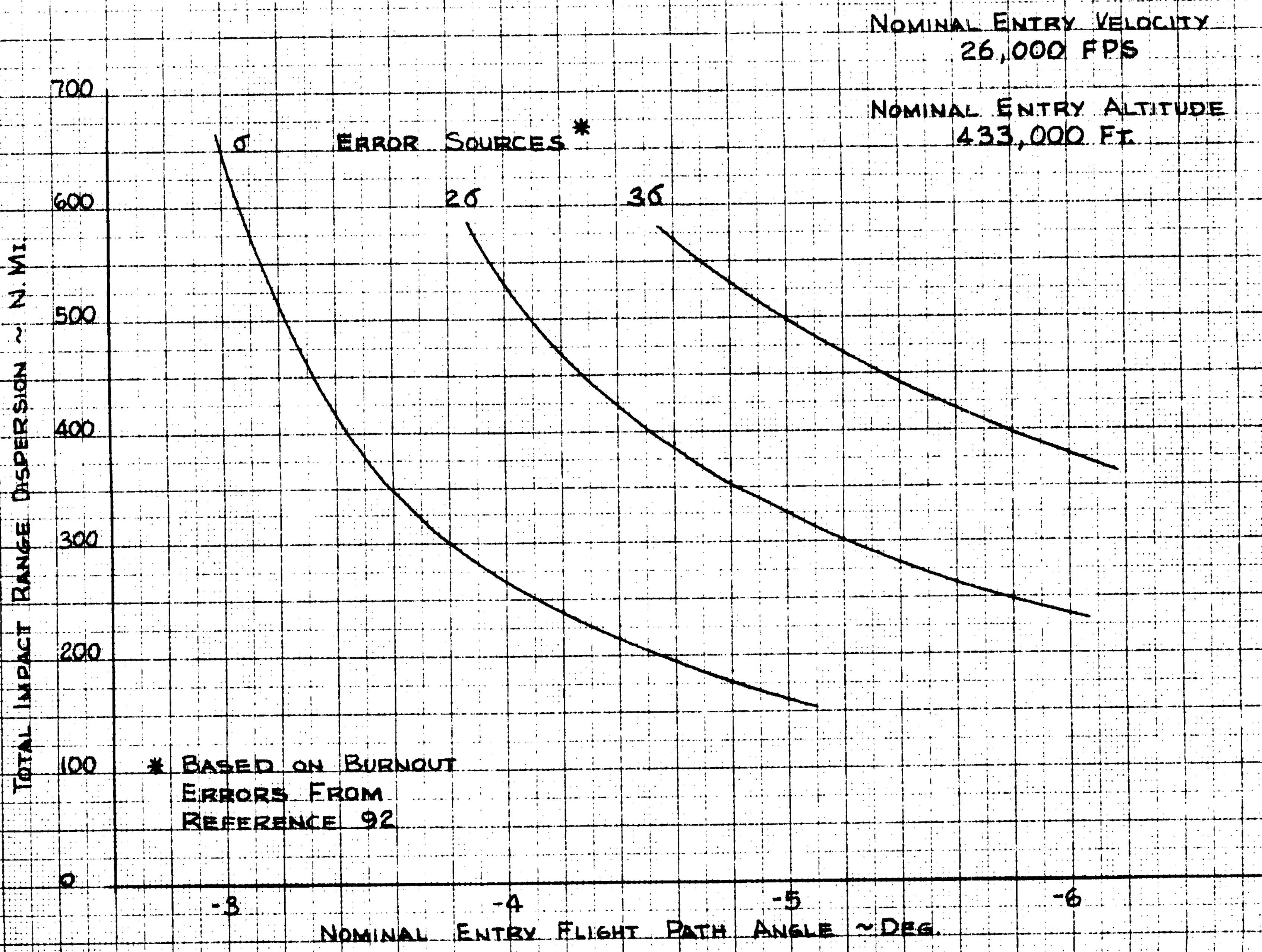

FIGURE 44

EFFECT OF NOMINAL ENTRY ANGLE ON TOTAL DISPERSION

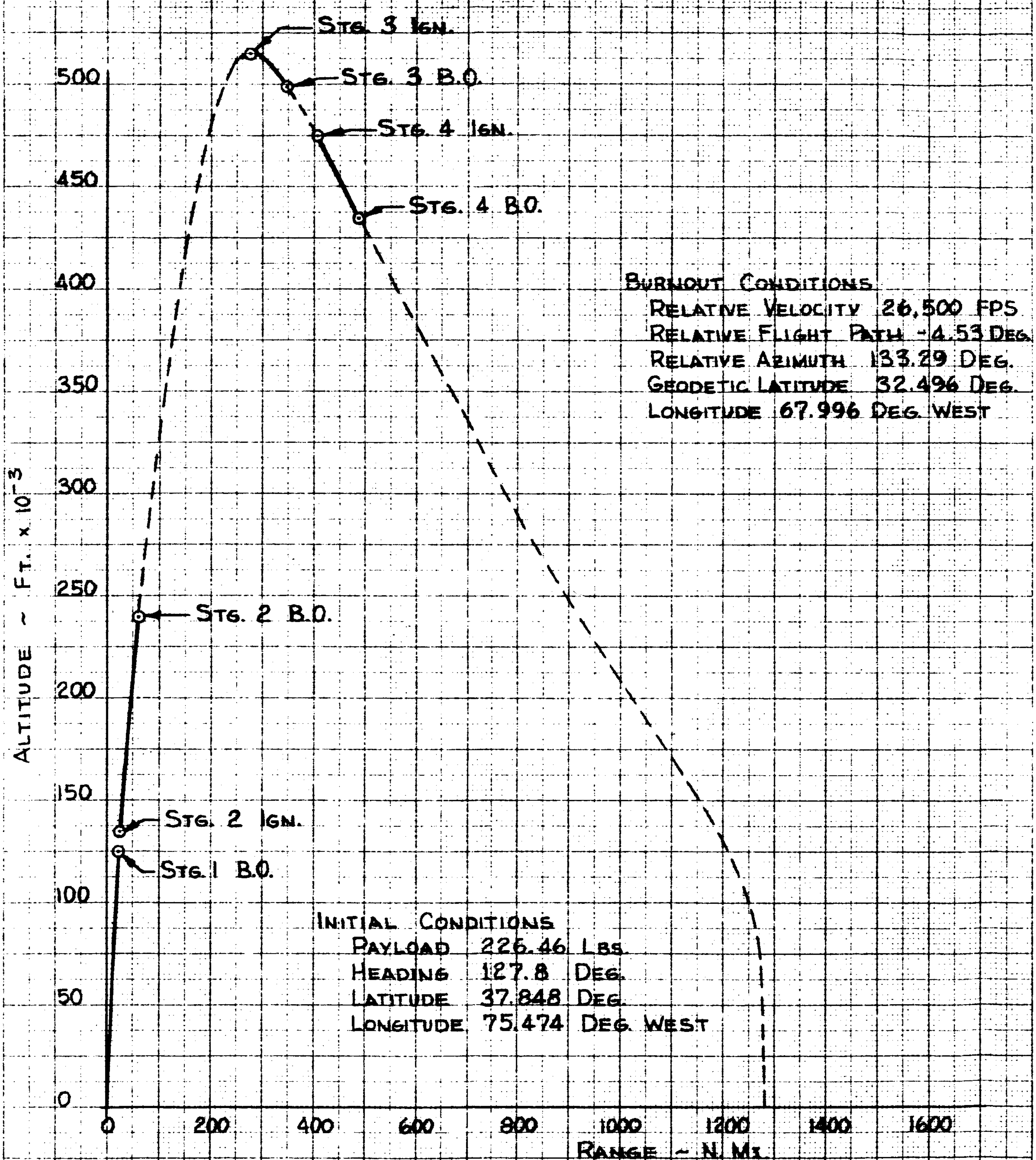

FIGURE 45

RANGE VS. ALTITUDE TRAJECTORY PROFILE FOR NOMINAL 4.53 DEG. ENTRY ANGLE

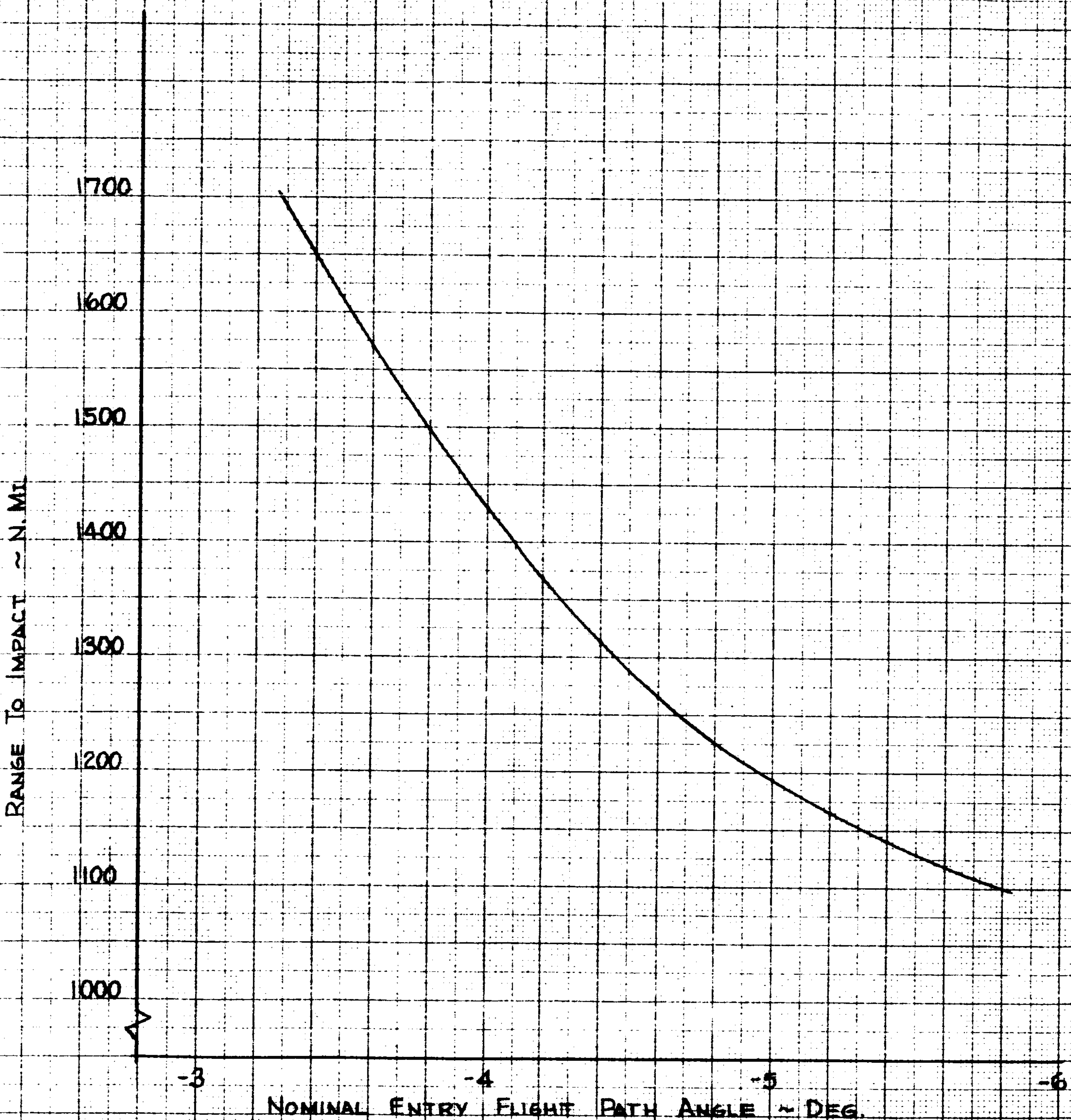

FIGURE 46

EFFECT OF ENTRY ANGLE ON LAUNCH - IMPACT RANGE

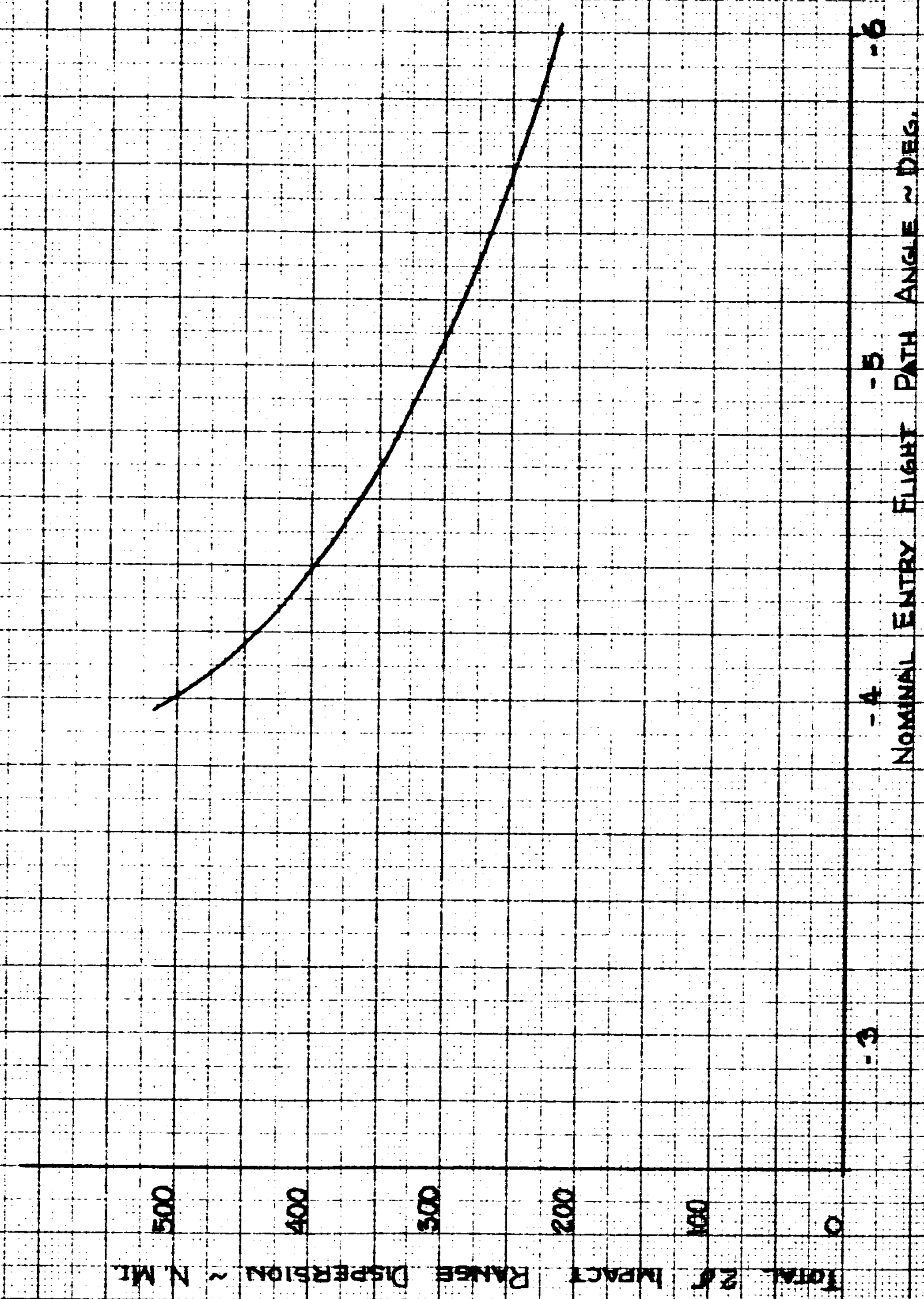

FIGURE 47

EFFECT OF NOMINAL ENTRY ANGLE ON 2σ IMPACT RANGE DISPERSION

FIGURE 48
EFFECT OF CENTER OF GRAVITY POSITION ON
LOW SPEED STABILITY

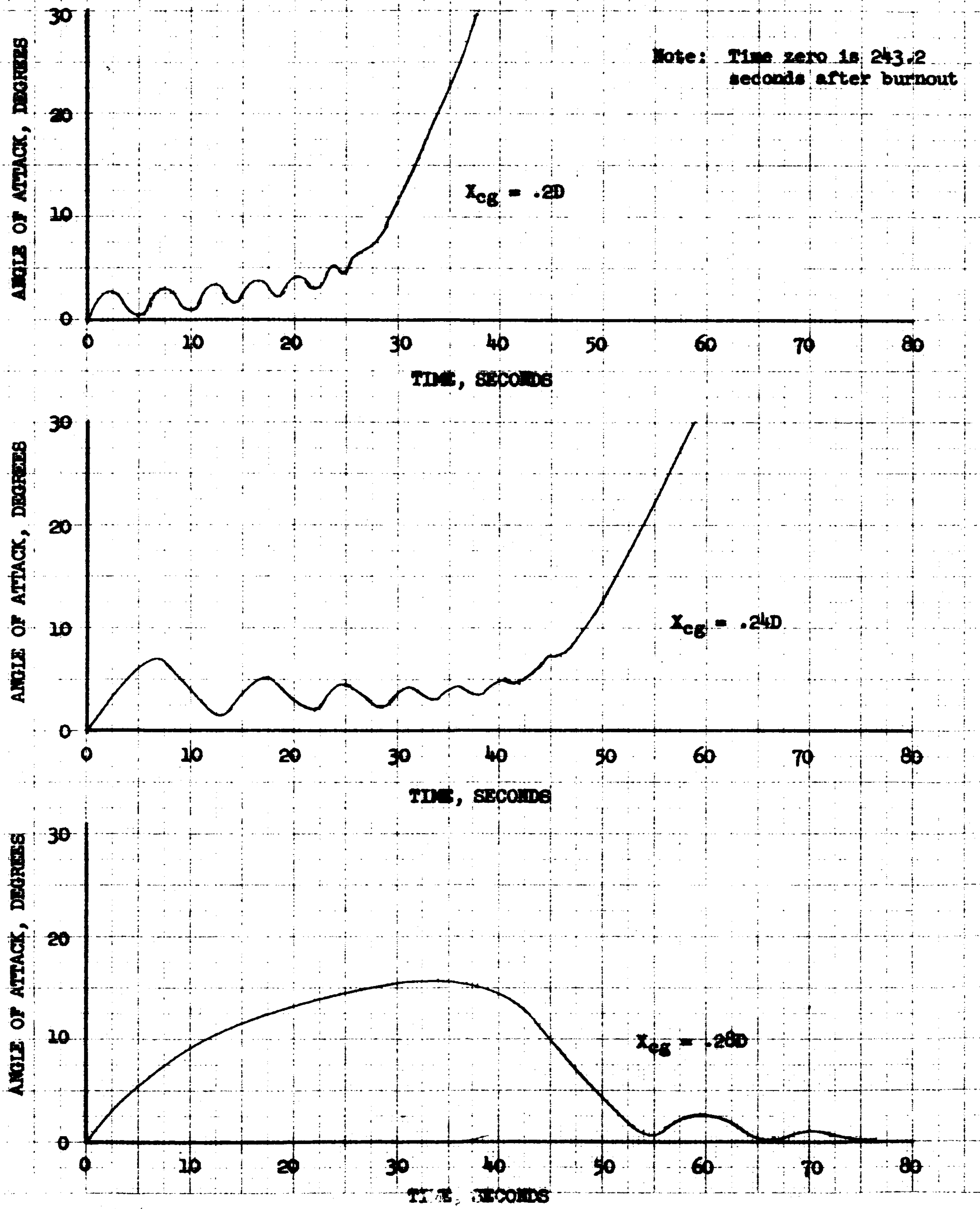

FIGURE 49

EFFECT OF CENTER OF GRAVITY LOCATION ON
ANGLE OF ATTACK ENVELOPE

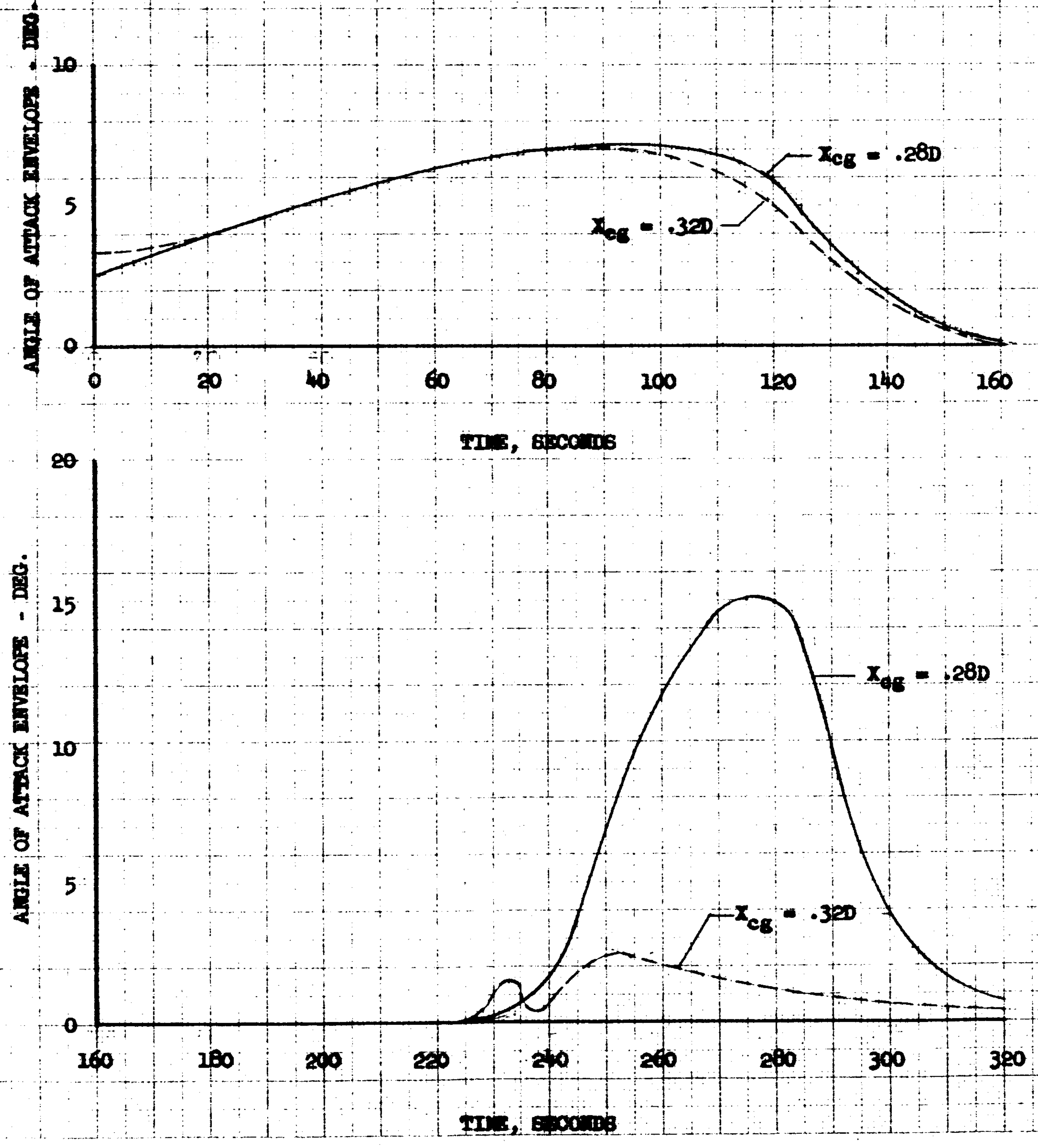

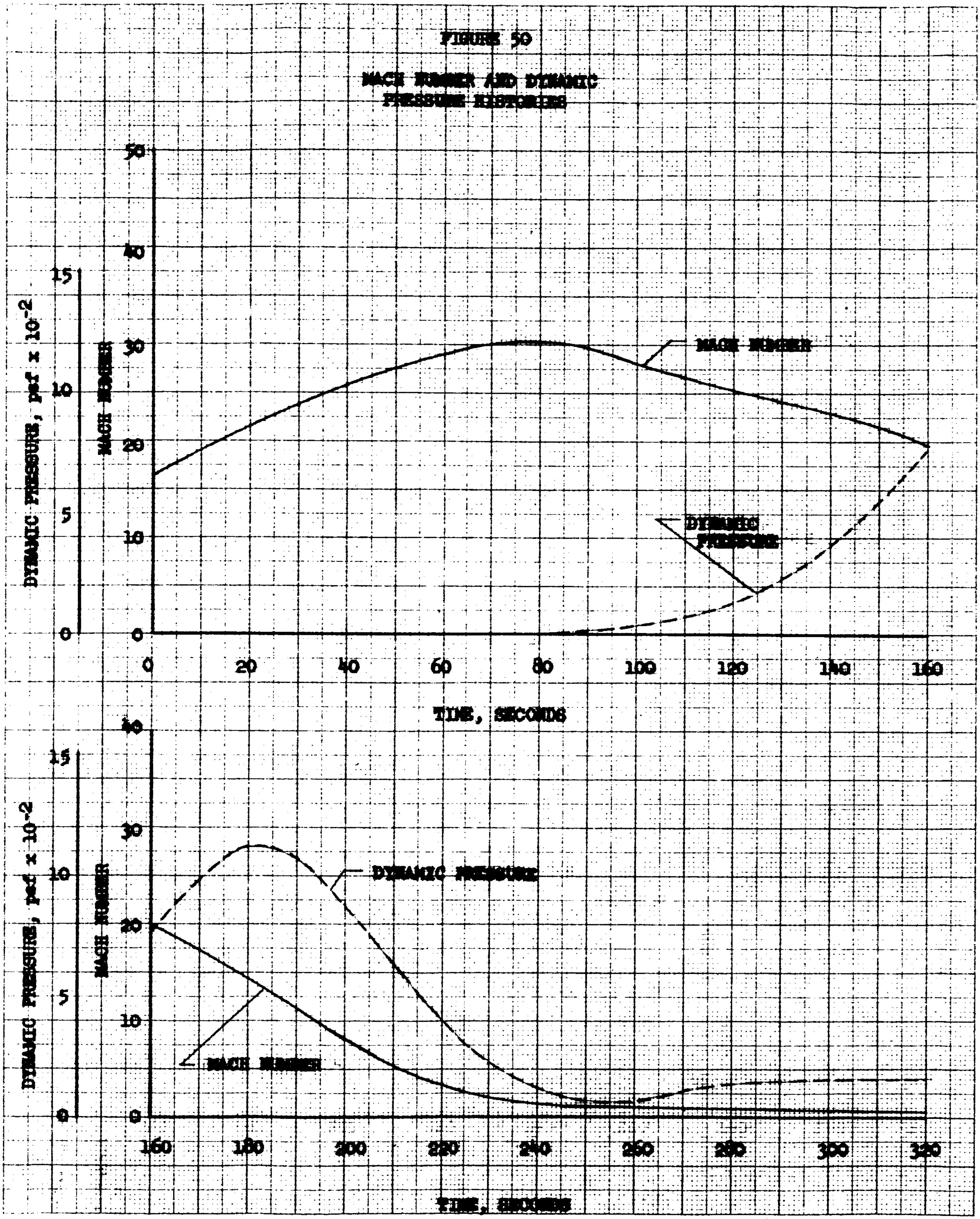
FIGURE 50
MACH NUMBER AND DYNAMIC PRESSURE HISTORIES
DYNAMIC PRESSURE, psf x 10^{-2}
MACH NUMBER
DYNAMIC PRESSURE
TIME, SECONDS
0
20
40
60
80
100
120
140
160
10
15
5
30
50
180
200
220
240
260
280
300
320

FIGURE 51

EFFECT OF AN INITIAL TIP-OFF ON THE ANGLE OF ATTACK ENVELOPE

$X_{cg} = 0.32\ D$

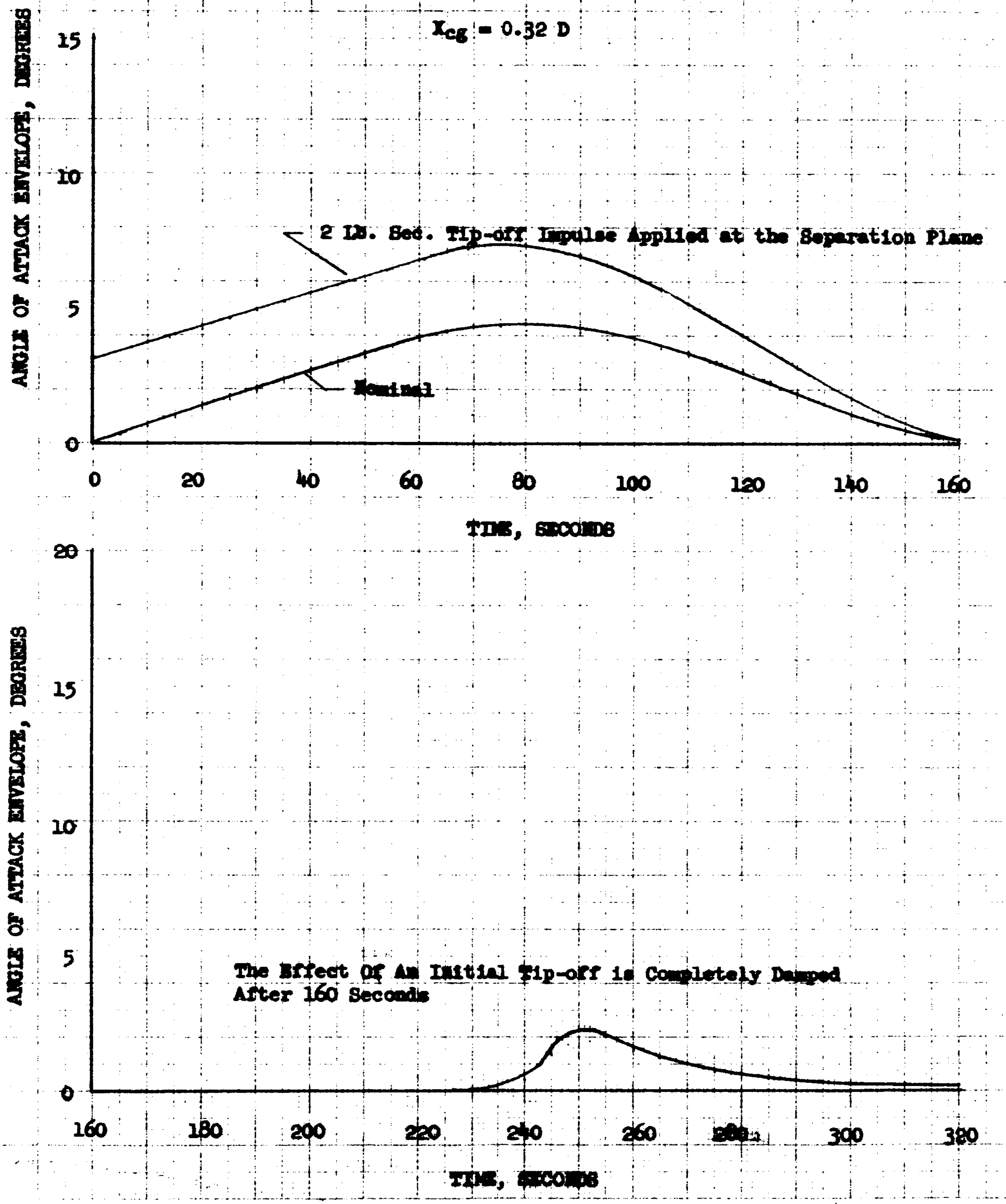

FIGURE 52

EFFECT OF MASS UNBALANCE ON THE ANGLE OF ATTACK ENVELOPE

$X_{cg} = 0.32$ D

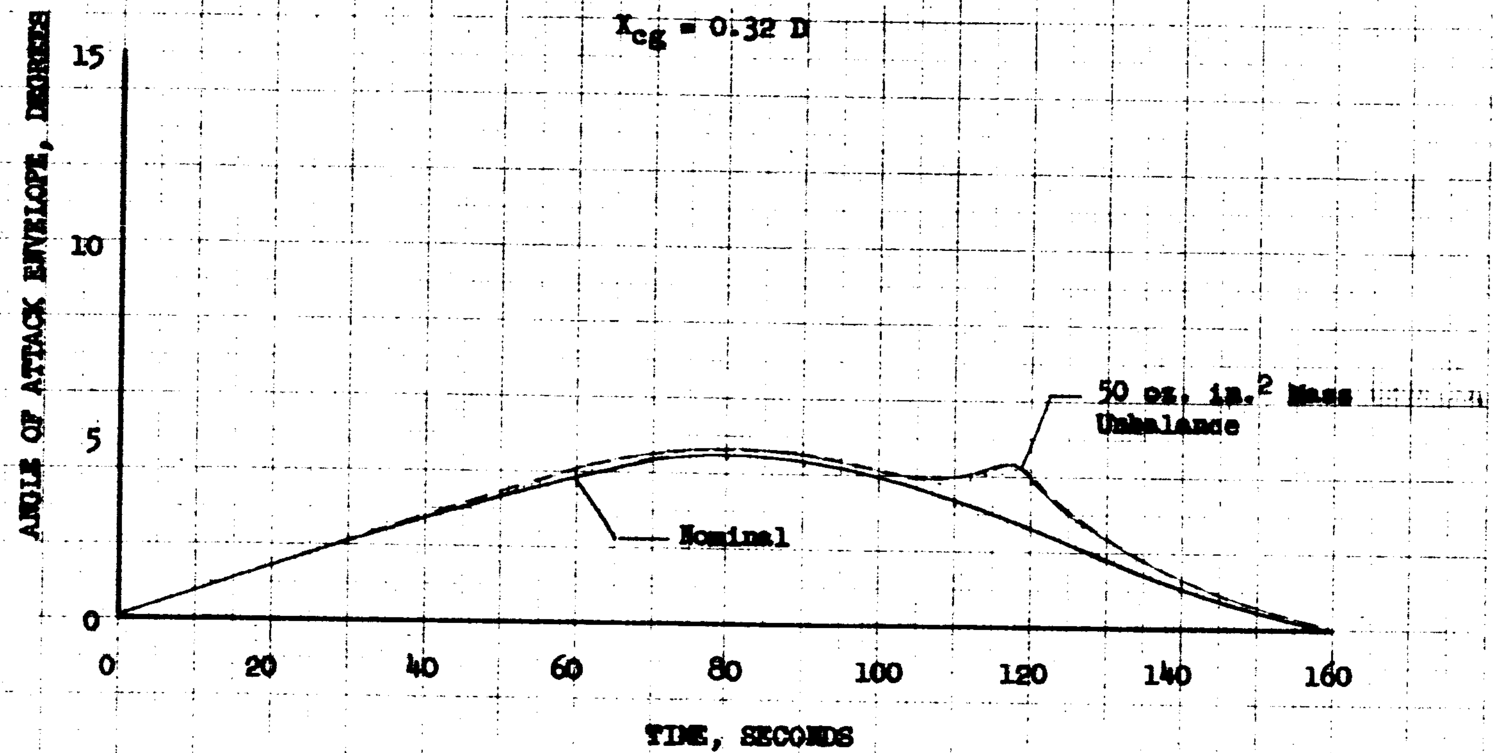

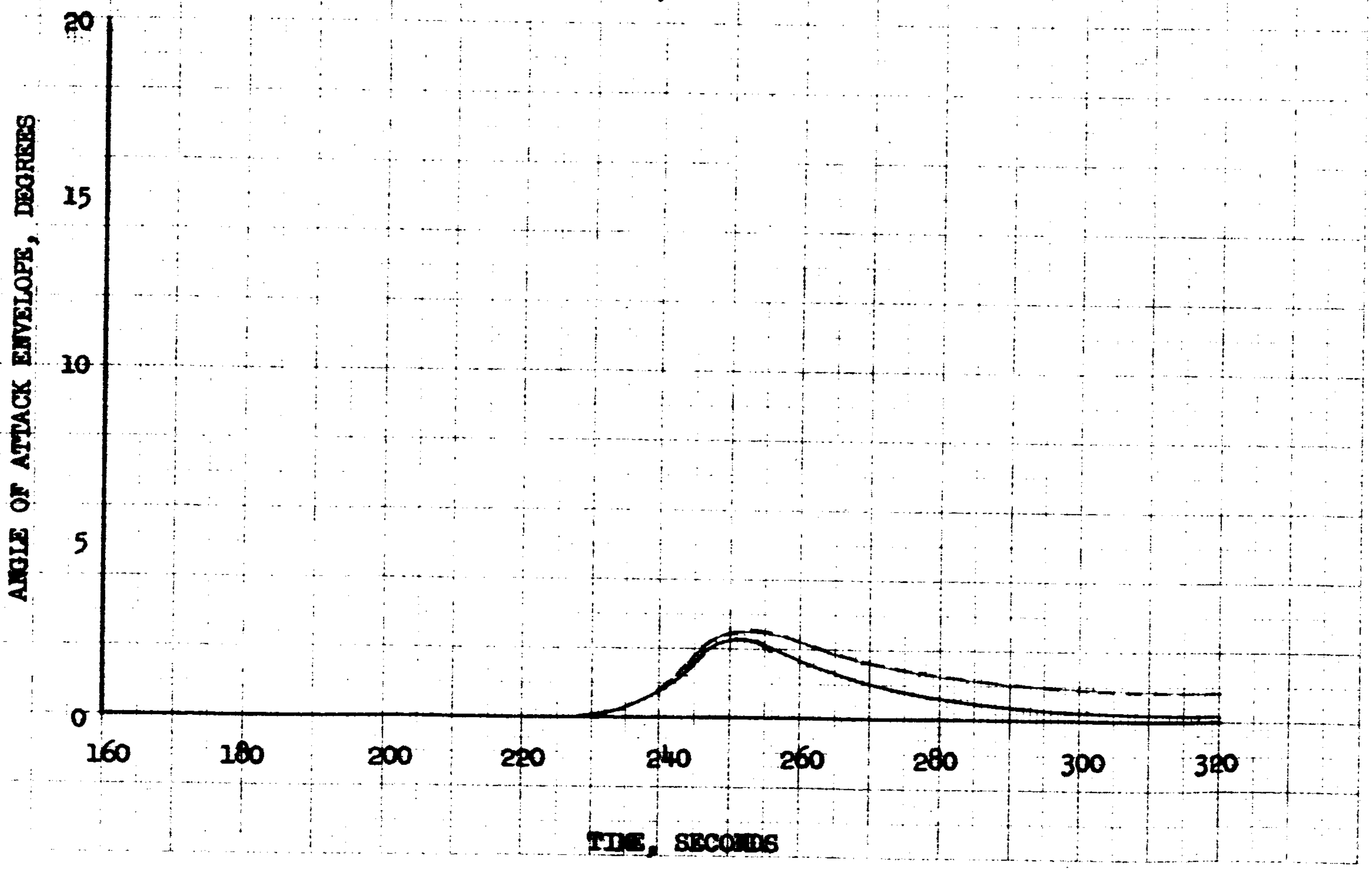

FIGURE 53

EFFECT OF CENTER OF GRAVITY
OFFSET ON THE ANGLE OF ATTACK ENVELOPE

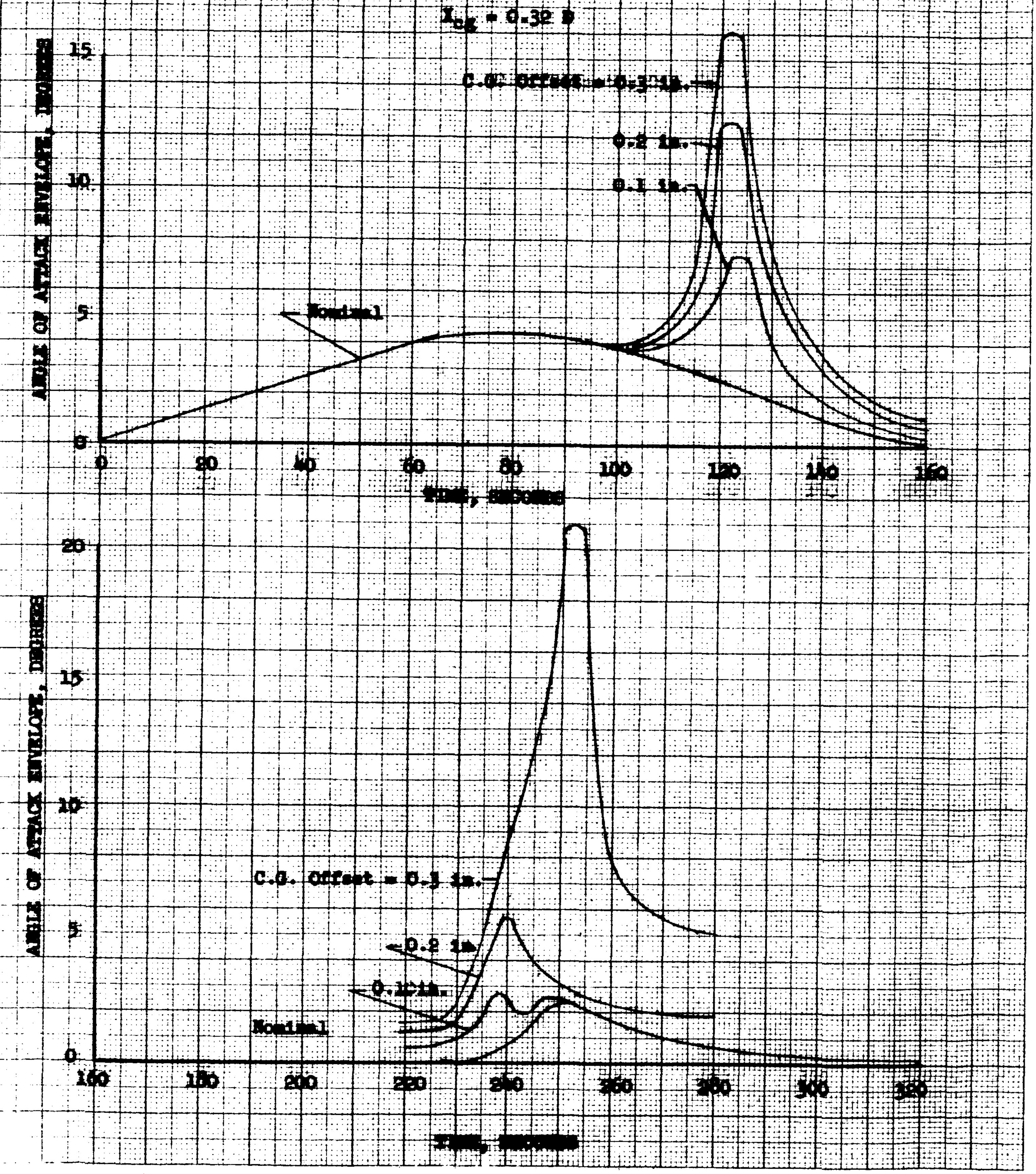

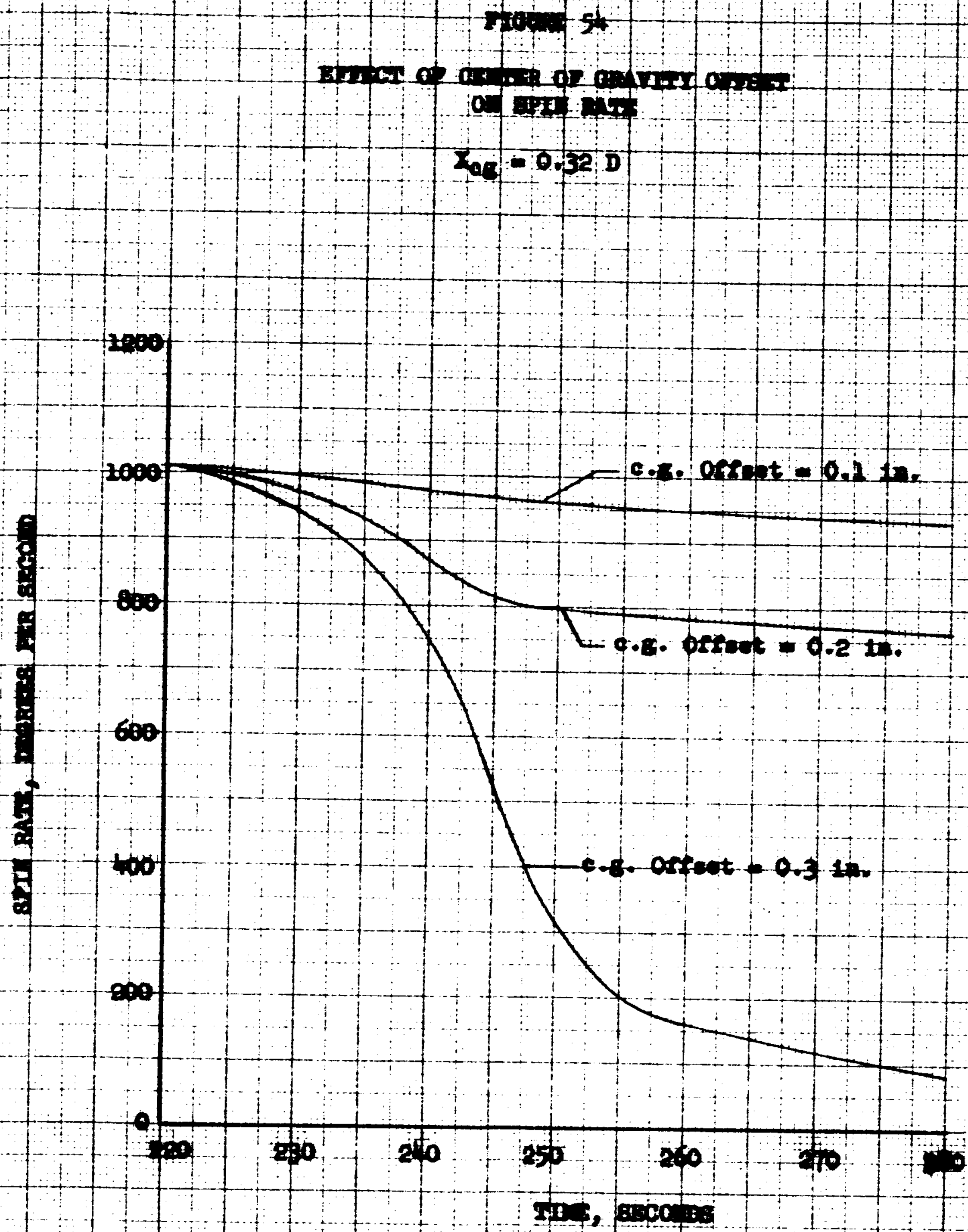
FIGURE 54
EFFECT OF CENTER OF GRAVITY OFFSET ON SPIN RATE
$X_{cg} = 0.32$ D
SPIN RATE, DEGREES PER SECOND
1200
1000
800
600
400
200
0
c.g. Offset = 0.1 in.
c.g. Offset = 0.2 in.
c.g. Offset = 0.3 in.
220
230
240
250
260
270
280
TIME, SECONDS

FIGURE 55

VARIATION OF SPINNING BODY

FREQUENCY WITH PITCH FREQUENCY

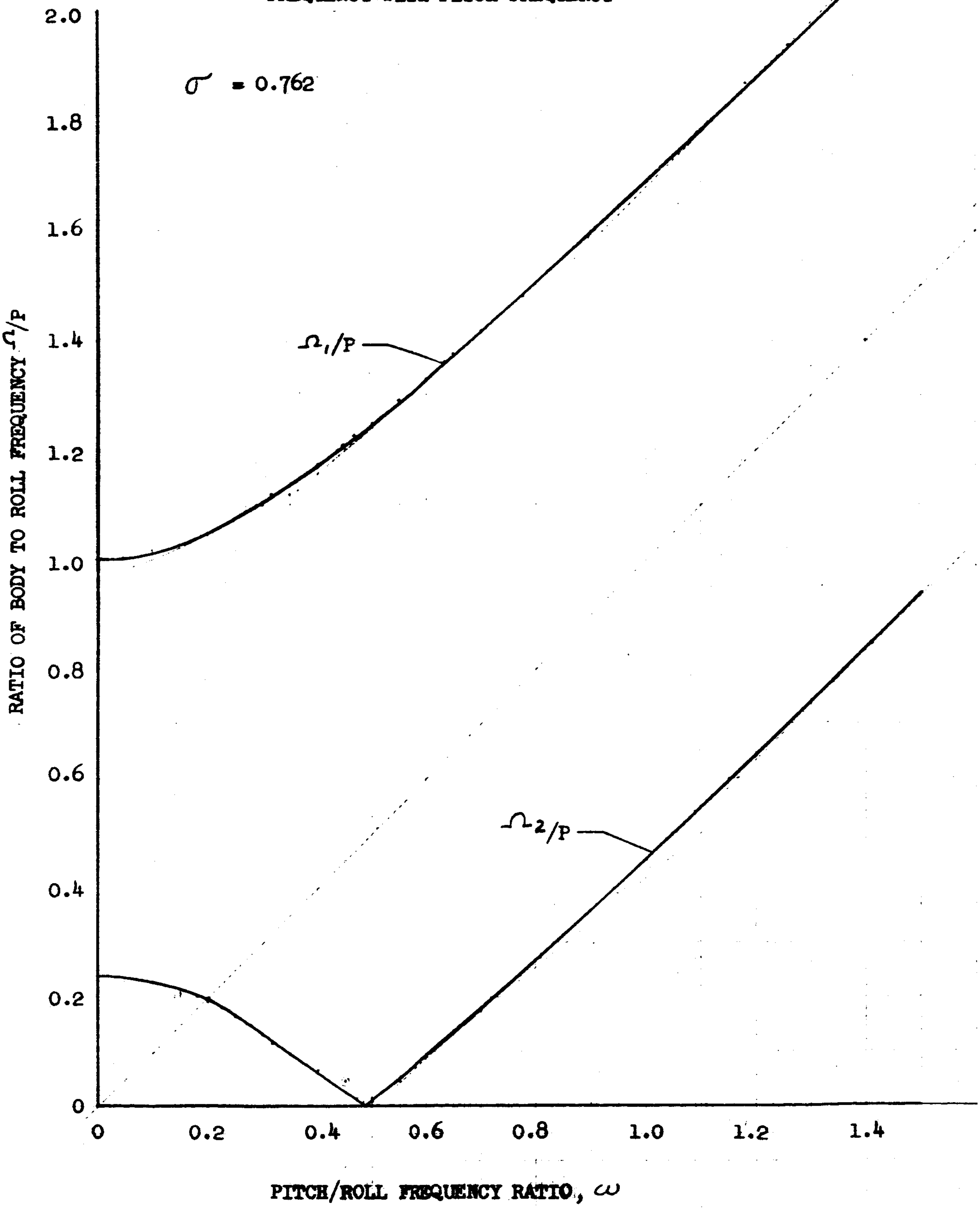

FIGURE 56

TIME HISTORY OF PITCH/ROLL FREQUENCY RATIO

$X_{cg} = 0.32$ D

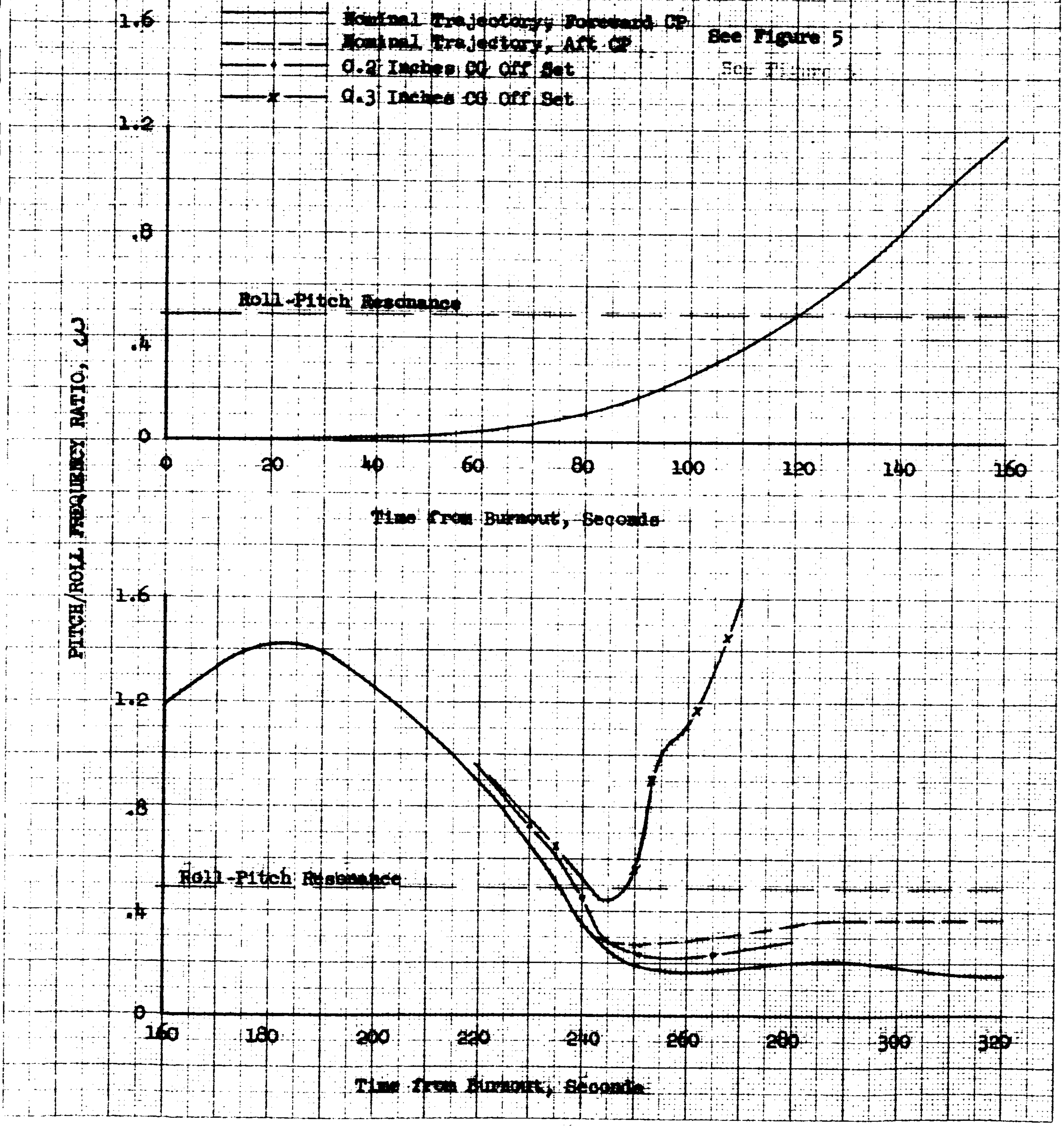

FIGURE 57

TIME HISTORY OF LOW FREQUENCY

NOMINAL TRAJECTORY

P = 3 cps

X_{cg} = 0.32 D

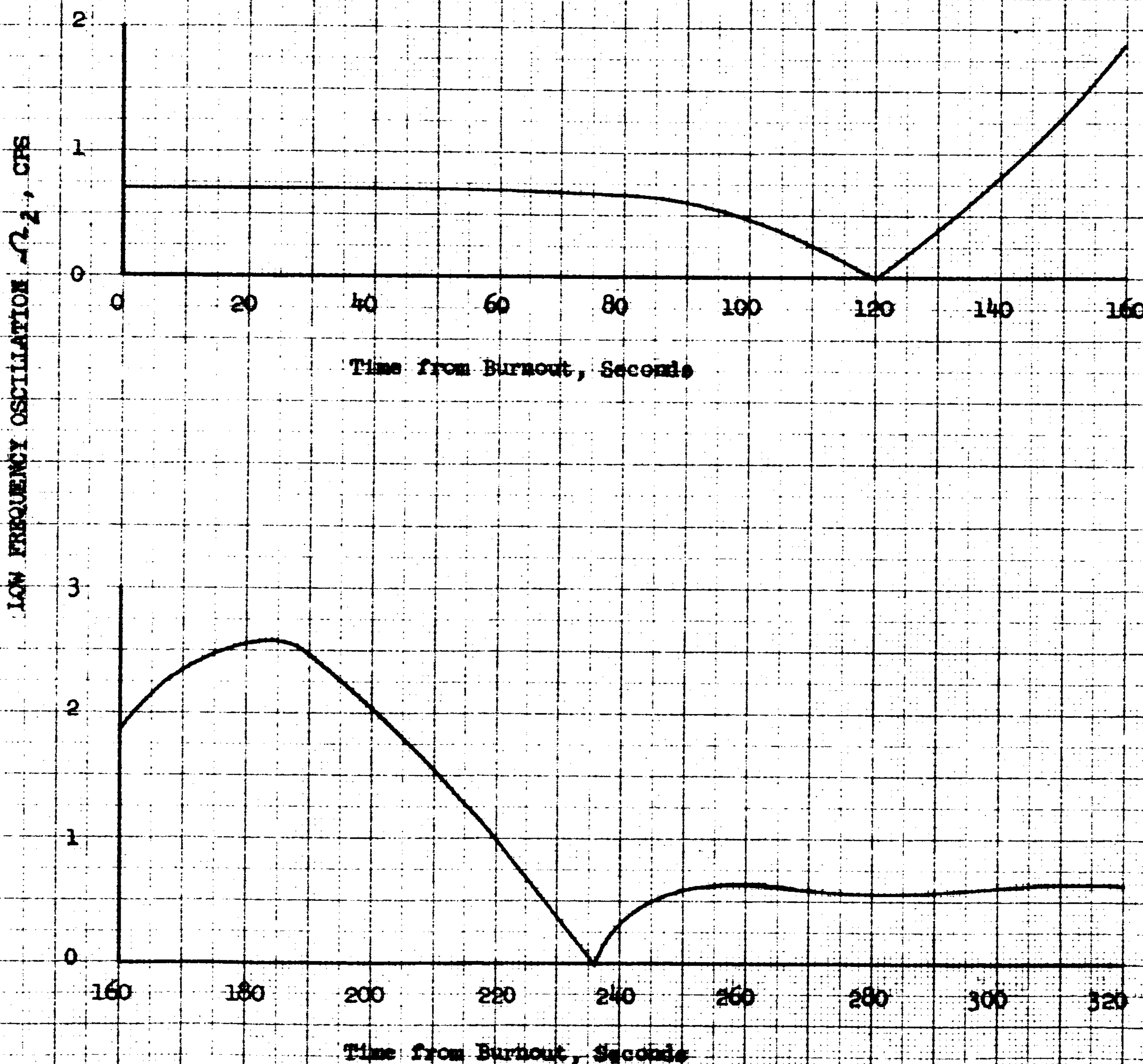

FIGURE 58

TIME HISTORY OF HIGH FREQUENCY

NOMINAL TRAJECTORY

P = 3 cps

X_{cg} = 0.32 D